Numerical Studies of Frustration and Entropic Ordering in Lattice Models

A Thesis

submitted to the

Tata Institute of Fundamental Research

for the degree of

Doctor of Philosophy in Physics

by

Geet Rakala

of the

Department of Theoretical Physics

Tata Institute of Fundamental Research

Mumbai

dated

December , 2018

DECLARATION

This thesis is a presentation of my original research work. Wherever contributions of others are involved, every effort is made to indicate this clearly, with due reference to the literature, and acknowledgement of collaborative research and discussions.

The work was done under the guidance of Professor [guide's name], at the Tata Institute of Fundamental Research, Mumbai.

GEET RAKALA

[candidate's name and signature]

In my capacity as supervisor of the candidate's thesis, I certify that the above statements are true to the best of my knowledge.

Kedar Damle.

[guide's name and signature]

Date: 21/12/2018

Publications relevant to this Thesis work

[1] Geet Rakala and Kedar Damle
Cluster algorithms for frustrated two-dimensional Ising antiferromagnets via dual worm constructions
Phys. Rev. E 96, 023304 (2017).

[2] Geet Rakala, Kedar Damle and Deepak Dhar
Statistics of worm algorithms.
In preparation

[3] Geet Rakala, Saumya Shivam, Nisheeta Desai and Kedar Damle
Z_6 parafermions in the triangular lattice antiferromagnet.
In preparation

[4] Geet Rakala, Dipanjan Mandal, R Rajesh, Kedar Damle, Deepak Dhar and Soham Biswas
Hard plates on a cubic lattice at full packing
In preparation

Other Publications by the author

[1] Sounak Biswas, Geet Rakala, and Kedar Damle
Quantum cluster algorithm for frustrated Ising models in a transverse field.
Phys. Rev. B 93, 235103 (2016).

Acknowledgments

I am grateful to my advisor Prof. Kedar Damle for introducing me to ideas that have become the bread and butter of my academic existence. I would like to thank Prof. Nic Shannon and Prof. Punyabrata Pradhan for a careful reading and useful comments that helped me improve this thesis. I would like to thank my collaborators, Prof. Deepak Dhar, Prof. R. Rajesh, Dipanjan Mandal, Sounak Biswas, Saumya Shivam and Nisheeta Desai for helpful discussions. I would like to thank my dear friends Rahul for making me a socialist, Nikhil for his shrewd advice whenever I needed it, Sambuddha for tolerating my long rants with brotherly patience, Nilay for making weekends sufferable and Maria for bringing purpose to my life. I am grateful to my mother for teaching me kindness, my father for always putting my needs first and my grandfather to whom I owe my faculties of reasoning. I would like to thank my high school physics teacher Dr. Sailesh Srivatsav for his inspired teaching. I would like to thank Kapil for his ever-timely help with the clusters and the DTP administrative unit for their ever-friendly support. I would like to thank my DTP colleagues for bringing our office to life. Finally, I will be eternally in debt to the humble Indian tax-payer who overcame innumerable hardships in this unfair world to fund a nobody's education.

> A loose, unbarbed arrow, lodged in a wound with a broad mouth and lying in an Anuloma direction, should be withdrawn by applying a magnet to its end. A shaft of grief, driven into the heart by any of the multifarious emotional causes, should be removed by exhilaration and merry-making.
>
> ——— *S*usruta-samhita 800±200 BCE

Contents

Chapter 1

Introduction

The second law of thermodynamics determines the equilibrium properties of a closed system. The entropy S of a closed system at equilibrium is always maximised. For a system that can exchange energy with the surroundings the second law implies that the Helmholtz free energy F, given by $F = E - TS$ is minimised, where E is the internal energy of the system and T is the temperature. At a constant temperature, the system can minimise its free energy by either maximising its entropy or minimising its internal energy. Entropy of a system can be thought of as a measure of the disorder of the system. Larger the disorder, larger the entropy. Thus, if at a finite T, the system orders, the loss in entropy is compensated by a decrease in the internal energy of the system. The simplest statistical physics example one can consider is the ferromagnetic Ising model in 2 dimensions, which was solved exactly by Onsager [1]. Below a critical temperature T_c the system orders because the decrease in the internal energy of the system outweighs the decrease in entropy. Such an ordering transition is 'energy driven'. There is another class of ordering transitions which are purely entropy driven. Consider a system for which the internal energy is a function of the temperature T, but not of the density. Classical systems with hard-core repulsion fall in this category. When these systems undergo an ordering transition as a function of density, they can do so only by increasing their entropy. The earliest such example was again given by Onsager [2] wherein he showed that a three dimensional fluid of thin hard rods must undergo a transition to a nematic ordered phase (where the orientations of the rods are aligned on an average) upon compression. This happens because the translational entropy of the rods increases in the nematic phase.

Generally speaking, it is very hard to write down an analytical expression for the free energy, F, of a system. Only a handful of simple systems exist for which exact solutions are known and even then only is some limiting cases. For example the exact solution of the 2-d Ising model is known only in the $\mathbf{B} = 0$ limit, where $\mathbf{B}$ is an external magnetic field. In case of the hard-rod system, the phase transition can be found exactly only in the $L/D \to \infty$ limit, where L is the length of the rod and D is

the diameter. Systems with many competing interactions have complicated phase diagrams. Although simple approaches such as mean field theory exist, it is not enough to provide a quantitative analysis of the complex features that exist near a phase transition. Numerical techniques like Monte-Carlo simulations[3] sample the configuration space of such systems and give us an insight into their equilibrium properties. They can be then used to determine the phase diagram as a function of various parameters like the temperature and interaction strength etc., which define the system. They can be also used to extensively characterise the phases and phase transitions, providing extensive support in understanding existing experimental data and also giving rise to new experimental directions. In this thesis, we numerically investigate using Monte-Carlo methods two systems: Ising antiferromagnet on the triangular lattice with next and next-next nearest neighbour interactions and hard squares at full packing on the cubic lattice. In the former the decrease in the internal energy determines the equilibrium properties of the system. In the latter, since there is no energy scale in the system, entropy determines the equilibrium properties. In both these cases we find that simple Metropolis Monte-Carlo algorithms that work by updating local configurations are not enough to equilibrate the system and we have to resort to non-local cluster algorithms. In the following sections, we present an overview of the both these types of systems, starting from their experimental origins to their theoretical modelling and various methods used to gain insights into their rich equilibrium properties. It must declared that the introductory scientific material presented in this Chapter is in essence a rewording of excerpts from many excellent books and review articles on these subjects and references are made wherever possible to the better source. This is in no way a complete introduction but merely an exercise in regurgitating what I remember from literature surveys while attempting to write this thesis with an obvious bias towards ideas used further in this thesis.

1.1 Magnetism

Magnetism is a uniquely interesting property exhibited by many naturally occurring and man-made materials. The first discovered and most abundant naturally occurring magnetic material was the mineral Magnetite with the chemical formula Fe_3O_4. Its use as a surgical tool by the ancient Indians, as a navigational tool by the ancient Chinese and as a philosophical object by the ancient Greeks has been recorded. Since then we have come a long way in finding practical uses for magnetic materials in every sphere of life from fridge magnets to the latest IBM quantum computer. Apart from this, the rich nature of magnetic materials gives perennial fodder to the hungry hordes of theoretical and experimental physicists with dozens of papers published each day contributing

to our ever increasing understanding and amazement about these materials and their properties. Chapter 3 of this thesis concerns itself with the study of a seemingly simple yet unsurprisingly complex theoretical magnetic model. Our main mode of enquiry into understanding this model is through numerical simulations. In Chapter 2 we develop and analyse the numerical simulation techniques needed to solve this model. In the subsequent subsections of this introduction, I provide the background needed to understand the model and numerical techniques of subsequent chapters. Further into this chapter, we will switch to entropic considerations as promised in the introduction and outline the background needed to understand the model thereof.

1.1.1 Magnetic materials

Magnetism can manifest in nature in many ways. Every material on earth is weakly diamagnetic, that is, it is repelled in the presence of an external magnetic field due to an induced magnetic field in the opposite direction. However this effect is generally very weak and hard to detect except in a class of materials known as superconductors. More commonly detected responses to an external magnetic field are paramagnetism and ferromagnetism, which easily outweigh the weak diamagnetism and become the defining properties of those materials. Paramagnetism is the more commonly observed effect, in which spins of the unpaired electrons in the material align with the external magnetic field causing a net attraction. However in the absence of an external magnetic field, the material doesn't have a net magnetic moment of its own. Ferromagnetic materials have a net magnetic moment in the absence of an external field. Below a critical temperature known as the Curie temperature, the spins in a paramagnet spontaneously align to produce a net magnetic moment. Other types of spontaneous alignment of spins exist including the antiferromagnet in which below a Neel temperature, the number of *up* aligned spins exactly cancel the number of *down* aligned spins creating a net-zero magnetic moment. Ferrimagnetism happens when this cancelling is not exact and a net magnetic moment survives. Some anti-ferromagnets can show ferrimagnetism in the presence of an external magnetic field. Materials in which there are no unpaired electrons are diamagnetic and are colloquially referred to as non-magnetic since diamagnetism is hard to detect. Hence all magnetic materials have unpaired electrons which respond to an external magnetic field. Although the spin of an electron and hence all magnetic interactions are quantum mechanical in nature, it is useful to work in a classical and semi-classical approximation to gain some physical insight into the problem. Here we start with the empirically observed Hund's rule and Pauli principle and work our way through justifications of the origins of a few types of magnetic interactions which form the basis of models further explored in this thesis.

Dipole moment of an electron

Electrons respond to magnetic field because they have a net dipole moment. This dipole moment has two contributions, one due to the intrinsic quantum-mechanical spin of the electron known as the spin magnetic dipole moment and the other due to the revolution of the electron around a nucleus known as the orbital magnetic dipole moment*. The total magnetic dipole moment of an electron is given as

$$\vec{\mu}_J = g_J \mu_B \frac{\vec{J}}{\hbar} \tag{1.1}$$

where μ_B and $\hbar$ are the Bohr magneton and Planck's constant respectively. $\vec{J}$ is the total angular momentum given as $\vec{J} = \vec{S} + \vec{L}$ where $\vec{S}$ and $\vec{L}$ are the spin angular momentum and the orbital angular momentum respectively. g_J is the lande g-factor which is related to the spin g-factor g_S and the orbital g-factor g_L by the expression

$$g_J = g_L \frac{J(J+1) - S(S+1) + L(L+1)}{2J(J+1)} + g_S \frac{J(J+1) + S(S+1) - L(L+1)}{2J(J+1)}. \tag{1.2}$$

Pauli's exclusion principle

Pauli's exclusion principle† states that two fermions cannot have the same quantum numbers. Electrons being fermions, follow this principle and hence if two electrons occupy the same orbital their spin quantum number has to be different.

Hund's rules

The first Hund's rule‡ can be explained in terms of Pauli's exclusion principle and the Coulomb interactions between electrons. Coulomb interactions between dipole moments of electrons energetically favours electrons of similar spin over electrons of opposite spins. This along with Pauli's exclusion principle ensures that electrons of similar spin occupy different orbitals before electrons of opposite spins occupy the same orbital. This leads to the first rule that the total spin S is always maximised. The second rule states that the total orbital angular momentum L consistent with S is maximised. The third rule states that the total angular momentum J is $|L-S|$ when the shell is less than half-full, S when the shell is half-full and $L+S$ when the shell is more than half-full.

*This picture assumes that the electron is localised around a nucleus. In metals, where the electron is delocalised, a quantum mechanical wave picture is more useful and can be found in [4].

†The quantum mechanical origins of this principle can be found in [5]

‡A more nuanced description of Hund's rules can be found in [6]

1.1.2 Magnetic ordering

The ideal paramagnet: Curie's law

Consider a system of N independent spins with no interaction between the spins in an external magnetic field B. The partition function of a single spin is given by the Brillouin function

$$Z = \frac{sinh(\Delta(J+1/2))}{sinh(\Delta/2)} \tag{1.3}$$

where $\Delta = \frac{\mu_B B}{k_B T}$. The net magnetisation per unit volume is then

$$M \sim -\frac{d\ln(Z)}{d\Delta} \tag{1.4}$$

which has the following limits:

$$\lim_{T\to 0} M(T) \sim J \tag{1.5}$$

$$\lim_{T\to \infty} M(T) \sim J(J+1)\frac{B}{T} \tag{1.6}$$

In the limit of a small magnetic field $B = \mu_0 H$, the susceptibility is given as :

$$\chi = \frac{M}{H} \sim J(J+1)\frac{\mu_0 \mu^2}{T} \tag{1.7}$$

This is known as the Curie's law and is used as an experimental signature to detect systems in which the interaction between the electron dipole moments are weak.

Exchange coupling

The paramagnet is an example of a non-cooperative magnet in which the individual electron dipole moments behave independently and are unaware of each others existence. This is often not the case and magnetic moments of electrons have an influence on neighbouring electrons. This leads to cooperative magnetism. Two types of exchange interactions are possible following from Pauli's exclusion principle. Direct exchange occurs when the electrons are close enough such that the wavefunctions overlap. Indirect exchange happens when the electrons are so far apart that the exchange is mediated by an intermediary. In metals, the intermediaries are delocalized electrons giving rise to RKKY(Ruderman and Kittel, Kasuya and Yosida) interactions. In insulators, the intermediaries are non-magnetic ions in the lattice giving rise to superexchange. Both RKKY and superexchange interactions in the presence of strong spin-orbit coupling give rise to DM(Dzyaloshinsky-Moriya) interactions. The direct exchange cou-

pling can be represented as a spin-dependent coupling term in the Hamiltonian as:

$$H_E = -\sum_{ij} J(r_{ij})\vec{S}_i.\vec{S}_j \tag{1.8}$$

where r_{ij} is the distance between two ions at i and j with spins $\vec{S}_i$ and $\vec{S}_j$ respectively. J_{ij} is the exchange parameter. In the case of intra-atomic direct exchange, the exchange parameter J is positive following Hund's rules. For inter-atomic direct exchange the sign of J is determined by the inter-play between Coulomb and kinetic energies of the pair of magnetic ions. Coulomb interaction forces the ions apart. However, increase in localisation increases the kinetic energy. In the case of indirect exchange, J can be positive or negative for superexchange and oscillates between positive and negative for RKKY exchange depending on the separation between the ions.

Ferromagnetism

A ferromagnet is a cooperative magnet. In an ideal ferromagnet, each site of a crystal is occupied by an identical magnetic ion with a spontaneous dipole moment with positive (J>0) inter-atomic direct exchange between the ions. The magnetic ions then form domains which spontaneously magnetise along an easy axis determined by the crystal field D. An external field doesn't change the magnitude of the intrinsic magnetisation of these domains, but helps them in aligning along the direction of the field. As temperature increases, the thermal energies of the magnetic moments eventually overcome the exchange energies and the system transitions into a paramagnet above the critical Curie temperature T_c. The magnetic susceptibility χ above T_c is given by the Curie-Weiss law as:

$$\chi \sim \frac{1}{T - T_c} \tag{1.9}$$

Examples of crystalline ferromagnets include Fe, Co and Ni. Various alloys of Fe, Ni and Co are also examples of amorphous ferromagnets.

Antiferromagnetism

An ideal antiferromagnet is similar to the ideal ferromagnet but with a negative exchange parameter (J<0). Thus magnetic moments on neighbouring sites of a crystalline lattice are oppositely aligned giving rise to a net zero magnetic moment. The lattice of an ideal antiferromagnet can be divided into two sublattices, each with a ferromagnet. The direction of the spontaneous magnetisation in these two ferromagnets is exactly opposite and cancel out each other. Hence there is no overall spontaneous magnetisation. As temperature increases, the thermal energies of the magnetic moments eventually overcome the antiferromagnetic exchange energies and the system

transitions into a paramagnet above the critical Neel temperature T_N. Below T_N, the magnetic susceptibility increases with increasing temperature. Above T_N, the magnetic susceptibility is given by a Curie-Weiss law. Examples of antiferromagnets include ionic compounds such as FeO, CoO, MnS etc. and ordered alloys such as Fe_3Mn, Pt_3Fe and CrPt.

Ferrimagnetism

In a simple crystalline ferrimagnet, different kinds of magnetic ions occupy different sublattices of the system. The magnetic moments in a sublattice have ferromagnetic exchange. But the exchange between different sublattices is antiferromagnet. A net spontaneous magnetisation arises when the net moments of the different sublattices don't cancel each other exactly due to generally different number of sublattice sites per unit cell and different moments of the ionic magnets on each of those sublattices giving rise to a ferrimagnet. Examples of crystalline ferrimagnets include $FeO.Fe_2O_3$(magnetite), $NiO.Fe_2O_3$, $MnO.Fe_2O_3$ etc. Amorphous ferrimagnetism exists in direct analogy to the crystalline case except that the magnetic ions in the sublattices have random positions. Examples include alloys like $TbFe_2$ and $GdFe_2$ where Tb-Tb, Gd-Gd and Fe-Fe interactions are ferromagnetic but Tb-Fe and Gd-Fe are antiferromagnetic. Temperature dependence of a ferrimagnet is similar to that of a ferromagnet with a transition to a paramagnet above the Curie temperature T_c. However, the magnetic susceptibility shows significant deviation from the Curie-Weiss law near T_c.

Other types of magnetic ordering

Many other types of magnetic ordering exists and below we list a few well known types to give a flavour of the variety:

- **Metamagnetism** where a magnetic field induced transition happens from a state of low magnetisation to a state of high magnetisation through a phenomenon known as *spin flop*. Examples include 3d transition metal compounds like YCo_2, $TiBe_2$, and $FePt_3$.

- **Incipient ferromagnetism** happens when the exchange coupling is not strong enough to form a long-range ferromagnet. However, at very low temperatures small domains of similarly aligned magnetic moments emerge and are stabilised over experimentally measurable timescales. Such domains are called *paramagnons*. Palladium and platinum are examples which display incipient ferromagnetism.

- **Superparamagnetism** occurs when small single domain particles of ferromagnetic nature below a critical volume can be made to thermally fluctuate fast

enough along the easy axis of the crystal such that net measured magnetisation is zero. This is different from the paramagnetic transition of a ferromagnet because it happens below the Curie temperature. Examples include Co particles in mercury and Fe particles in amorphous gels.

- **Speromagnetism** is the phenomenon by which below an ordering temperature T_{ORD}, the magnetic moments are frozen in random directions such that there is no net magnetisation. This effect is mainly observed in systems with RKKY and superexchange interactions. Example of a superexchange enabled speromagnetism is FeF_3 and RKKY enabled speromagnetism is CuMn.

- **Asperomagnetism** Asperomagnetism is similar to ferromagnetism but with some orientations of magnetic moments more probable than others giving rise to a net spontaneous magnetisation. YFe_3 and $DyNi_3$ are examples.

- **Helimagnetism** is asperomagnetism on a crystalline lattice where magnetic moments on the sites of a crystalline lattice are frozen in different orientations below the ordering temperature T_{ORD}, but with some orientations more probable than others giving rise to a net spontaneous magnetic moment. $MnAu_2$ is an example.

- **Weak ferromagnetism** also known as canted antiferromagnetism or parasitic ferromagnetism occurs when two or more antiferromagnetic sublattices are canted at an angle and do not cancel each other out exactly resulting in a net magnetic moment. This can be caused by a difference in single-ion anisotropy in the sublattices (NiF_2) and DM interactions (β-MnS).

Detailed explanations of the various magnetic orderings and the various magnetic excitations associated with them can be found in [[7]]

1.2 Theoretical modelling

1.2.1 Spin models

Heisenberg model

Working in the approximation where a quantum spin is represented by a vector $\vec{S}_i$ in a three dimensional space at site i the exchange coupling hamiltonian of Eq. [1.8] can

be written more generally as[§]:

$$\mathcal{H} = -\sum_{ij} \left(J_{ij}^x S_i^x S_j^x + J_{ij}^y S_i^y S_j^y + J_{ij}^z S_i^z S_j^z \right) \tag{1.10}$$

where $\vec{J}_{ij} = (J_{ij}^x, J_{ij}^y, J_{ij}^z)$ is the anisotropic exchange parameter. In the isotropic limit, the Heisenberg model is

$$\mathcal{H} = -J \sum_{ij} \left(S_i^x S_j^x + S_i^y S_j^y + S_i^z S_j^z \right) \tag{1.11}$$

In terms of the spin raising and lowering operators $S_i^{\pm} = S_i^x \pm i S_i^y$ this can be written as:

$$\mathcal{H} = -J \sum_{ij} \left[\frac{1}{2} \left(S_i^x S_j^x + S_i^y S_j^y \right) + S_i^z S_j^z \right] \tag{1.12}$$

When $J < 0$, it can be seen that the ground state is realised when all spins point in the same direction. Thus $J < 0$ is the ferromagnetic exchange parameter. For antiferromagnetic $J > 0$, the ground state has oppositely aligned neighbouring spins. In the presence of a magnetic field B along the $\hat{z}$ axis and a crystal field D along the easy axis of the crystal, the hamiltonian can be written as:

$$\mathcal{H} = -J \sum_{ij} \left(\vec{S}_i . \vec{S}_j \right) - \sum_i \sum_{\alpha=x,y,z} D_\alpha \left(\vec{S}_i . \hat{e}_\alpha \right)^2 - B \sum_i S_i^z \tag{1.13}$$

Ising model

The Ising model can be seen as a limiting case of the Heisenberg model when the easy axis of the crystal is anisotropic along the z direction with $D_z >> D_x, D_y$. The lowest energy state corresponds to spin doublet, $S^z = \pm s$ and the effective Hamiltonian can be written as:

$$\mathcal{H} = -Js^2 \sum_{ij} \sigma_i \sigma_j - Bs \sum_i \sigma_i \tag{1.14}$$

where $\sigma_i = \pm 1$. Examples of compounds favouring such anisotropy include K_2CoF_4 and Rb_2CoF_4[8]. The nearest neighbour Ising model has been solved analytically in one dimension by Ising[9] and in two dimensions by Onsager[1] on the square lattice. It can also be solved using transfer matrix methods on the square lattice. In subsequent sections, we will study this model in more detail using mean-field and Landau theory.

[§]The Hubbard model is a more general effective Hamiltonian which reflects the quantum mechanical nature of the spin of an electron, but is generally very difficult to solve and only solved exactly in one dimension. The generalised anisotropic Heisenberg model can be derived as a limit of this model at half filling.

XY model

When $D_z << D_x, D_y$, the spin is free to rotate in the XY-plane giving rise to the XY model represented as

$$\mathcal{H} = -J \sum_{ij} S_i^+ S_j^- + S_i^- S_j^+ \tag{1.15}$$

Rb_2CrCl_4 is an example of a compound which shows XY behaviour due to easy-axis anisotropy[10]. The XY model has been solved analytically by performing a Jordan-Wigner transformation of the spin raising and lowering operators into fermionic operators. Further exploration of the interesting physics that takes place in this model will be done in subsequent sections.

1.2.2 Mean field approximations

Mean field approximations are an important first tool in exploring the solutions of a many-body Hamiltonian. In the case of spin models, the effect of exchange interactions from neighbouring spins is approximated by a mean value of the spin and fluctuations around this mean value are ignored. As we shall see below mean field theory gets better with increasing dimension and above an upper critical dimension the fluctuations are much smaller than the mean value and can be ignored. This effect can be attributed to the fact that as the dimensionality of the system increases, the coordination number of the spin increases and there is a higher probability for the fluctuations from the neighbouring spins to cancel each other. In infinite dimensions, mean field theory becomes exact.

Weiss mean field theory

We will first study the Ising model using a mean field approximation on a d-dimensional hypercube with coordination number $z = 2d$. The mean value of spin s_i is approximated by the local magnetisation $m = \langle s_j \rangle$ as $s_i = m + \delta$ where $\delta = s_i - m$ and the limit $\delta \to 0$ is taken. Under this approximation Eq.[1.14] will read

$$\mathcal{H}^0 = \sum_i \mathcal{H}^0_{s_i} = -\sum_i s_i(zJm + B) \tag{1.16}$$

The expectation value of s_i under this Hamiltonian is given as:

$$\langle s_i \rangle = \frac{\text{tr } s_i e^{\beta \mathcal{H}^0_{s_i}}}{\text{tr } e^{\beta \mathcal{H}^0_{s_i}}} = \tanh[\beta(zJm + B)] \tag{1.17}$$

Using the self consistency condition $m = \langle s_i \rangle$, we get the magnetisation as:

$$m = \tanh[\beta(zJm + B)] \tag{1.18}$$

In the absence of a magnetic field B, when $\beta zJ < 1$, the only solution is $m = 0$, corresponding to a paramagnet. When $\beta zJ > 1$, three solutions exist: $m = 0$ and $\pm m_0$ corresponding to the Z_2 symmetry breaking of a ferromagnet. Thus the critical temperature is given by $\beta zJ = 1$ or $k_B T = zJ$. In 1-d, this simple mean-field approximation predicts a phase transition at $k_B T_c = 2J$. But we know using the Peierls argument[11] that there is no phase transition in 1-d. In 2-d the mean-field approximation does better by predicting a phase transition at $k_B T_c = 4J$. However, the exact transition temperature calculated by Onsager is $k_B T_c = \frac{2J}{\ln\left(1+\sqrt{2}\right)} \sim 2.269J$. In 3-d, the predicted value is $k_B T_c = 6J$ as compared to the numerically calculated value of $k_B T_c = 4.511J$[12].

Bethe mean field theory

Bethe a gave a more nuanced version of the Weiss mean field approximation which greatly improves the predictions of mean field theory. We start by considering a cluster of $z + 1$ spins: the spin s_i and its z nearest neighbours. We improve the mean field approximation by saying that each of the neighbours interact with s_i directly, but the interaction between the neighbours is only through an effective Weiss mean field. With this approach if we follow a procedure similar to the one shown above for Weiss mean field theory and solve a self consistency equation, we end up with the following form for the critical temperature:

$$k_b T_c = \frac{2J}{ln(\frac{z}{z-2})} \tag{1.19}$$

In 1-d since $T_c = 0$, this correctly predicts that there is no phase transition. In 2-d, the prediction is $T_c = \frac{2J}{\ln 2} = 2.885J$ which is much closer to the exact value than the Weiss mean field prediction. Taking bigger and bigger clusters for the mean field approximation will increase the accuracy of the predicted exponent at the cost of increasing difficulty. However at the critical point when the correlations are long range, any finite cluster approximation will fail at correctly predicting the critical exponents for dimensions less than the upper critical dimension.

1.2.3 Order parameter

Order parameter is a model dependent quantity that can be used to distinguish between the ordered and disordered phases of the system. The order parameter for a system is not unique. Any quantity which is zero is the disordered phase and non-zero in the ordered phase is a viable order parameter.

Heisenberg model: The ferromagnetic Heisenberg model orders below T_c for dimensions greater than 2. The ground state corresponding to an energy minimum is realised when all the spins point in some arbitrary direction $\hat{n}$ and there is a net magnetisation. Above T_c, the system is disordered and there is no not magnetisation. Thus a natural order parameter for this model would be the total magnetisation vector $\vec{m} = \frac{1}{N}\sum_i \vec{S}_i$. For $T < T_c$, in the ordered state it takes the value $\vec{M} = M\hat{n}$. In the disordered state for $T > T_c$, $\vec{M} = 0$. In the absence of an external field, the Hamiltonian has $O(3)$ symmetry and the symmetry is spontaneously broken in the ordering direction $\hat{n}$.
Ising model: For the 2-d ferromagnetic square lattice Ising model a viable order parameter is the scalar total magnetisation $M = Nm$, where m is the intensive magnetisation. The ferromagnetically ordered ground state of this model for $T < T_c$ has Z_2 symmetry in the absence of an external field. $M = \pm N$ in the two ground states and is 0 in the disordered state for $T > T_c$.
XY model: In the 2-d XY model, the spins are free to rotate in the XY plane. The ordered ground state can be described by the two component vector $\vec{M} = (M_x, M_y)$. However the situation is more complex with the ordered state undergoing a KT transition which cannot be described by a local order parameter. We will return to this topic in subsequent sections.
Other more complicated ground state ordering of spins require complex order parameters as we shall see in the subsequent sections.

1.2.4 Landau theory

Landau developed a phenomenological theory for predicting the type of phase transitions a system can undergo. The basis of writing down a Landau theory is to identify an order parameter and expand the Gibb's free energy around it, such that the symmetries of the system are respected. If we were to consider an Ising ferromagnet, the local magnetisation m is a good order parameter, since it is 0 in the paramagnetic phase and ± 1 in the ferromagnetic phase. The Z_2 symmetry of the system at $B = 0$ implies that the Gibb's free energy should be same for $\pm m$. Hence in the expansion, only terms which are even powers of m appear. The Gibb's free energy can be written as:

$$G(m,T) = a(T) + \frac{1}{2}b(T)m^2 + \frac{1}{4}c(T)m^4 + \frac{1}{6}d(T)m^6 + ... \tag{1.20}$$

By expanding around the mean value m, we have neglected the fluctuations around this mean value. A variation of the Landau theory called the Landau-Ginzburg theory takes into account these fluctuations. Landau theory successfully explains the continuous/2$^{\text{nd}}$ order transitions, 1$^{\text{st}}$ order transitions and the interplay between them.

2nd order transitions

Let $c(T), d(T), .. > 0$. We then Taylor expand $b(T)$ around T_c upto linear order as $b(T) = b_0(T - T_c)$. The ground state solution at a given T should minimise the free energy. Hence we get

$$\frac{\partial G}{\partial m}\Big|_T = bm + cm^3 + dm^5 + ... = 0 \tag{1.21}$$

The solutions to first order are, $m = 0$ for $T > T_c$ and $m_0 = \pm\sqrt{\frac{-b}{c}}$ for $T < T_c$. At $T = T_c$, $b = 0$. In the limit $T \to T_c^-$, $m_0 = \pm\sqrt{\frac{b_0}{c}(T_c - T)}$. The value of the order parameter, m changes continuously at all times as T is varied, hence the transition is continuous/2nd order in nature.

1.2.5 Critical exponents

In the previous subsection we saw that the in the case of a 2nd order phase transition in the 2-d Ising model, the temperature dependence of magnetisation near the critical point T_c is given as $m \sim (T_c - T)^{1/2}$. Here $1/2$ is a critical exponent which turns out to be independent of the microscopic details of the model and belongs to a universality class. In this case it is the mean-field/Landau universality class in which fluctuations can be ignored. Above the model dependent upper critical dimensions all models fall in this class. The universality class of a model can be determined in the frame work of a renormalisation group theory¶. These critical exponents can serve as effective experimental and numerical markers to understand the underlying effective theory which governs the phase transitions observed in the system. We first define $t = \frac{T - T_c}{T_c}$. The critical point is then marked by $t = 0$ and critical exponents predict the behaviour of various measurable quantities in the vicinity of criticality. Below we list a few critical exponents and their definitions in terms of measurable quantities.

Specific heat:

$$C(B = 0, t) \sim \frac{1}{t^\alpha} \tag{1.22}$$

Magnetization:

$$M(B = 0, t) \sim |t|^\beta \tag{1.23}$$

$$M(B, t = 0) \sim |B|^{\frac{1}{\delta}} \tag{1.24}$$

Magnetic susceptibility:

$$\chi(B = 0, t) \sim \frac{1}{|t|^\gamma} \tag{1.25}$$

¶For a review of the renormalization group framework refer to[13]

Correlation length:

$$\xi(B=0,t) \sim \frac{1}{|t|^{\nu}} \tag{1.26}$$

In the above discussion we have assumed that the critical exponents above and below T_c are the same. This assumption is not always valid and breaks down for example in the presence of anisotropies. The critical exponents obey various scaling relations. For example $\alpha + 2\beta + \gamma = 2$ and $\delta = 1 + \frac{\gamma}{\beta}$.

1.2.6 XY model

The spins in the XY model are unit vectors free to rotate in the XY plane and can be represented as $\vec{S}_i = (\cos\theta_i, \sin\theta_i)$ where θ_i is the angle of the spin with respect to a fixed direction in the XY plane. Eq.[1.15] then can be rewritten as:

$$\mathcal{H} = -J\sum_{ij} \vec{S}_i.\vec{S}_j = -J\sum_{ij} \cos(\theta_i - \theta_j) \tag{1.27}$$

This Hamiltonian as mention before can only be exactly solved in 1d. Mermin-Wagner theorem[14] tells us that there can be no long range order for $d \leq 2$ in case of continuous spins. In 2d mean field calculations do not work because the upper critical dimension is 4 and fluctuations are too important an effect to be ignored in this model. However, we can still do a high temperature series expansion of the partition function. The partition function is given as:

$$Z = \int_0^{2\pi} \prod_i \frac{d\theta_i}{2\pi} e^{-\beta\mathcal{H}} \tag{1.28}$$

To leading order this becomes:

$$Z \sim \int_0^{2\pi} \prod_i \frac{d\theta_i}{2\pi} \prod_{ij} (1 + K\cos(\theta_i - \theta_j)) \tag{1.29}$$

where $K = \beta J$. Now, the spin correlation function g(r) can be calculated as:

$$\langle S(r).S(0)\rangle = \left[\int_0^{2\pi} \prod_i \frac{d\theta_i}{2\pi} \cos(\theta_r - \theta_0) \prod_{ij} [1 + K\cos(\theta_i - \theta_j)]\right] /Z \tag{1.30}$$

Taking appropriate approximations to leading order, we find

$$\langle S(r).S(0)\rangle \sim e^{\frac{-|r|}{\xi}} \tag{1.31}$$

where ξ is the correlation length given by $\xi = 1/\ln(a/K)$ where a is the nearest neigh-

bour distance. Thus, at high temperatures, the correlation function decays exponentially and the system is disordered.

At low temperatures, the spins can be thought of as pointing in the same general direction, but with fluctuations coming from spin waves of long wavelength. This picture can be treated by taking the continuous approximation $\theta_i \rightarrow \theta(\vec{r})$. The Hamiltonian then becomes:

$$\mathcal{H} = \frac{1}{2} J \int d\vec{r}\, (\nabla\theta)^2 \tag{1.32}$$

Spin correlations can be easily obtained by then solving a Gaussian integral and take the form

$$\langle S(\vec{r}).S(0)\rangle \sim \begin{cases} e^{-aT} & \text{for} \quad d > 2 \quad \text{(1.33a)} \\ \left(\frac{r}{L}\right)^{-\eta} & \text{for} \quad d = 2 \quad \text{(1.33b)} \\ e^{\frac{-|r|}{\xi}} & \text{for} \quad d = 1 \quad \text{(1.33c)} \end{cases}$$

At $d = 1$ there is no phase transition as the model is always disordered. For $d > 2$, the model orders at low temperatures and undergoes a continuous phase transition into the high temperature disordered phase. The most interesting physics happens at $d = 2$. There is no long range order at low temperatures. But the spins are algebraically correlated. This means thats the system is at criticality with a temperature dependent critical exponent. As we keep increasing the temperature, this line of critical points needs to end somewhere for the system to transition into a disordered phase. This transition cannot be understood in the Landau free energy frame work since there is no local order parameter that disorders. A complete picture of this transition can be explained using renormalization group theory as done by Kosterlitz and Thouless[15]. The transition at $d = 2$ is hence dubbed a KT transition. We can however gain a qualitative understanding of this transition and an estimate of the transition temperature by considering excitations called *vortices* in the spin wave picture developed above.

1.2.7 The frustrated antiferromagnet

Antiferromagnetic order describes the the lack of any type of net magnetism in a magnetic system. First formulated by Neel[16], antiferromagnetic ordering exists below a Neel temperature T_N. The most basic realisation of this Neel order exists in a bipartite lattice of spins $\mathbf{S}$ with nearest neighbour antiferromagnetic exchange interactions $J > 0$. If the exchange interactions are isotropic, the Hamiltonian, H of the system can be written as:

$$H = J \sum_{\langle ij \rangle} \mathbf{S}_i.\mathbf{S}_j \tag{1.34}$$

Here, the sum is over nearest-neighbour links $\langle ij \rangle$ of the bipartite lattice. The spins then, below a Neel temperature, spontaneously pick an axis, $\mathbf{n}$ such that $\langle \mathbf{S}_{\vec{r}} \rangle = (-1)^{\vec{r}}\mathbf{n}$, that is the spin directions alternate. This classical antiferromagnet can be easily mapped to a classical ferromagnet, by the transformation $\mathbf{S}'_i = \eta \mathbf{S}_i$, where $\eta_i = (-1)^i$ Because of this duality, the mean-field theory which describes ferromagnets can be used as is to describe the antiferromagnets with the above substitution to take into account the 'sign' of the spin.

The antiferromagnetic order parameter can be then defined as

$$\mathbf{m} = e^{i\mathbf{Q}.r_i}\mathbf{S}_i \tag{1.35}$$

where $\mathbf{Q}$ is the ordering wavevector such that $e^{i\mathbf{Q}.\vec{r}_i} = \pm 1$

The difference between ferromagnets and antiferromagnets arises because the antiferromagnetic order-parameter does not commute with the Hamiltonian, unlike in the ferromagnetic case where the order parameter is the total spin and commutes with the Hamiltonian. This changes the dispersion-law of the spin-wave spectrum. Also, quantum-spin fluctuation become important. In this thesis we work in the classical limit and ignore quantum fluctuations. A way of destroying this duality with the ferromagnets in the classical limit is to move away from bipartiteness which introduces geometric frustration in the antiferromagnetic models and a simple transformation as shown above becomes impossible. Not surprisingly, many antiferromagnetic materials in nature do not crystallise in a simple bipartite manner. In fact, they crystallise in geometrically or topologically 'frustrated' lattices, of which the simplest two-dimensional analogue is the triangular lattice. The basic difference between a triangular lattice and a bipartite lattice motif is that in the triangular lattice case, the Neel order is frustrated. The geometry of the triangular lattice leads to competing exchange interactions resulting in 'geometric frustration' described in detail below in the subsequent sub-sections. This 'geometric frustration' on the triangular lattice causes it to not order at all temperatures. Only an incipient spin liquid behaviour with a huge ground state degeneracy is observed at $T \to 0$[17]. Many other types of geometrically frustrated models with spin-liquid behaviour have been analytically and numerically studied. Few examples include spin-ice[18, 19], pyrochlores[20], Kagome lattice models[21, 22] and Kagome ice[23]. Experimental interest in geometric frustration has been long standing. Many transition-metal oxides crystallise in geometrically frustrated lattices based on triangles or tetrahedrons that share corners, edges or faces [24]. Examples include anhydrous alums[25, 26], jarosites[27, 28], Herbertsmithite[29], Kapellasite[30], pyrochlores[31, 32], spinels[33, 34], magnetoplumbites[35, 36], garnets[36], ordered NaCl[37, 38], and many other structure types[24]. A new kind of system based on non-colloidal monolayers has also been shown to approximate the triangular lattice Ising antiferro-

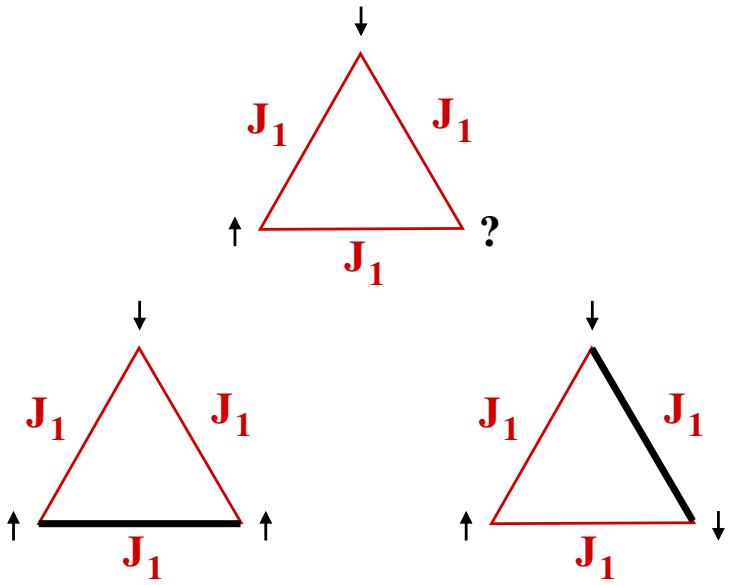

Figure 1.1: Triangular motifs showing Ising spins with antiferromagnetic nearest neighbour couplings. Due to geometric frustration on the triangular lattice, all the three spins cannot simultaneously satisfy the antiferromagnetic couplings. Shown in black is the one frustrated bond always present.

magnet in many ways[39]. Recently, a new class of rare-earth-based frustrated antiferromagnets have been discovered with effective Ising spins arranged on a perfect triangular lattice[40, 41].

Ground-state spin configurations of the triangular Ising model with nearest, next-nearest and next-next nearest neighbour interactions in the absence of an external magnetic field show a surprising variety. In fact it has been analytically shown that seven types of distinct ground states exist [42]. In this thesis, we concern ourselves with antiferromagnetic nearest neighbour interactions and ferromagnetic next-nearest and next-next nearest neighbour interactions as detailed below.

1.2.8 Antiferromagnetic nearest neighbour interactions on the triangular lattice Ising model

This triangular Ising spin net was studied by Wannier[17]. On the triangular lattice, the Ising antiferromagnet with nearest neighbour antiferromagnetic exchange interactions is defined by the Hamiltonian,

$$H = J_1 \sum_{\langle ij \rangle} S_i^z . S_j^z \tag{1.36}$$

where $\langle ij \rangle$ now represent nearest neighbour links on the triangle. In this case J_1 cannot pick a ground state even at $T \to 0$ as shown in the Fig[1.1] due to geometric frustration. In fact, the minimum energy configuration of this model at $T \to 0$ is defined as containing one frustrated bond per triangle as shown in Fig[1.2]. Frustrated

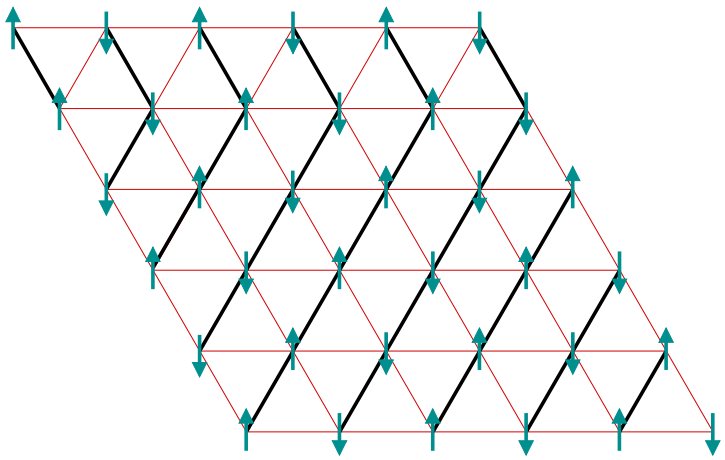

Figure 1.2: One of the many degenerate minimum energy ground states of the nearest neighbour Ising model on the triangular lattice. Up arrows represent up spins and down arrows represent down spins. The frustrated bonds, one per triangle, are shown in black.

bond here refers to the bond which doesn't satisfy the antiferromagnetic nature of the nearest neighbour coupling and is shown in 'black' in Fig[1.2]. This frustrated ground state can be thought of a spin-liquid which was shown to have an incipient order at the three-sublattice wavevector $\mathbf{Q} = (\frac{2\pi}{3}, \frac{2\pi}{3})$[43]. At $T \to 0$, the spins are correlated in a power-law fashion as:

$$\langle S^z(\mathbf{r}) S^z(0) \rangle \sim \frac{A_3 \cos\left(2\pi(\hat{x}+\hat{y})\right)}{\sqrt{r}} + \frac{A_0}{r^{9/2}} \tag{1.37}$$

Ferromagnetic next-nearest neighbour interactions on the triangular lattice Ising model

Further neighbour interactions, stabilise this spin-liquid ground state below a critical temperature [44]. A model with nearest neighbour and next-nearest neighbor interactions can be written as:

$$H = J_1 \sum_{\langle ij \rangle} S_i^z . S_j^z + J_2 \sum_{\langle\langle ij \rangle\rangle} S_i^z . S_j^z \tag{1.38}$$

where $\langle ij \rangle$ represent the nearest neighbour links of the triangular lattice and $\langle\langle ij \rangle\rangle$ represent the next-nearest neighbour links of the triangular lattice. For antiferromagnetic J_1 ($J_1 > 0$) and ferromagnetic J_2 ($J_2 < 0$), a ferrimagnetic three sublattice order as shown in Fig[1.3] is established. Ferrimagnetic refers to the fact that the three-sublattice order has a net magnetic moment. The three sublattice order breaks the symmetry between the three sublattices of the triangular lattice such that spins of one of the three sublattices of the triangular lattice point upward(downward) and the spins

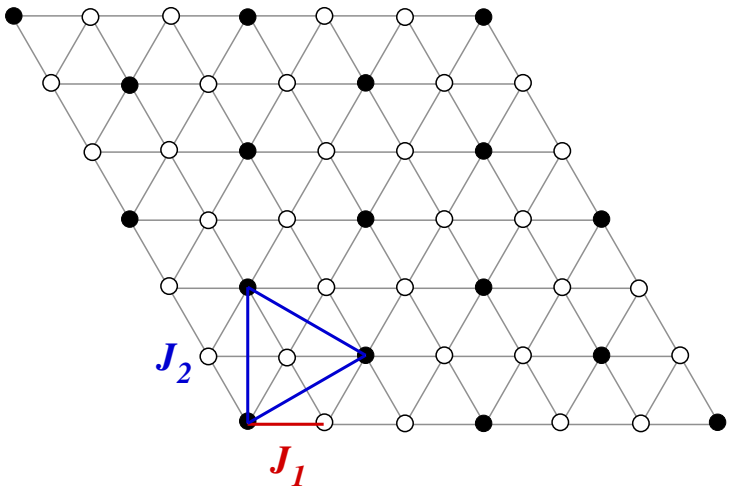

Figure 1.3: Ferromagnetic J_2 stabilises a ferrimagnetic three-sublattice ordered state with a net magnetic moment in which spins of one of the three sublattices of the triangular lattice point upward(downward) and the spins on the other two sublattices point downward(upward). Shown here is one such realisation of this six-fold symmetric three-sublattice order. The black dots represent 'up' spins and the white dots represent 'down' spins.

on the other two sublattices point downward(upward) giving rise to a six-fold symmetric ground state.

The three-sublattice order parameter can be defined as:

$$\psi \equiv |\psi| e^{i\theta} = -\sum_{\vec{R}} e^{i\frac{2\pi}{3}(m+n)} S^z_{\vec{R}} \tag{1.39}$$

where $\vec{R} = m\hat{e}_x + n\hat{e}_y$ as shown in Fig[1.4].

On the triangular lattice, the melting of this three-sublattice order has been studied extensively as a model for the melting of three-sublattice order in monolayer films of adsorbed noble gases on graphite substrates [45, 46]. The potential on the graphite surface has hexagonal symmetry and the adsorbed gas molecules tend to sit on the hexagonal centres forming a triangular net. Owing to the large effective size of the gas molecules, the nearest site occupation is unfavourable. By assigning an 'up' spin to the occupied sites and a 'down' spin to vacant sites, this model can be mapped to a triangular lattice Ising antiferromagnet. On the triangular lattice antiferromagnet, at $B = 0$, the ferromagnetic next-nearest neighbour couplings (J_2) stabilise a three-sublattice ordered phase of the ferrimagnetic kind (having a net magnetic moment) below a critical temperature. The three-sublattice ordered state is known to melt in a two-step manner, with an intermediate-temperature phase characterised by power-law three-sublattice order of the Ising spins σ: $\langle\sigma(\vec{R})\sigma(0)\rangle \sim cos(\mathrm{Q}.\vec{R})/|\vec{R}|^{\eta(T)}$ with the temperature dependent power-law exponent $\eta(T) \in (1/9, 1/4)$ [47].

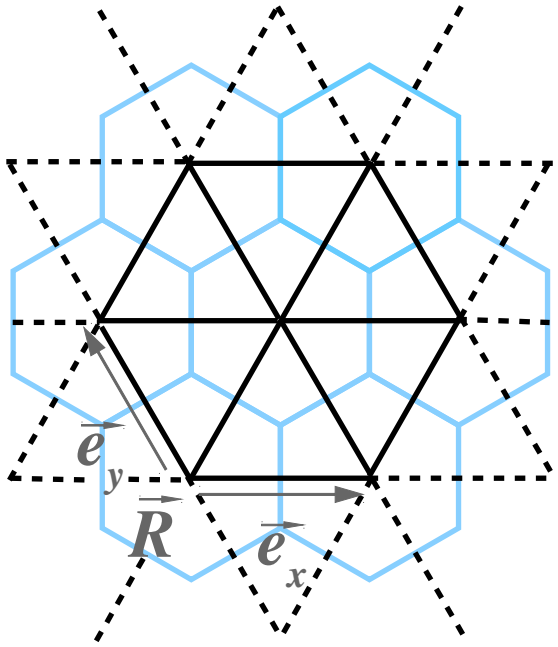

Figure 1.4: The triangular lattice shown in black with its dual honeycomb lattice shown in blue

Ferromagnetic next-next nearest neighbour interactions on the triangular lattice Ising model

Next-next-nearest ferromagnetic interactions (J_3) stabilize a striped order which consists of alternating rows of 'up' and 'down' spins as shown in Fig[1.5]. It was shown that ferromagnetic J_3 is equivalent to a antiferromagnetic J_2 in that they stabilise the same stripe ordered ground state[44]. The Hamiltonian for this model can be written as:

$$H = J_1 \sum_{\langle ij \rangle} \mathbf{S}_i.\mathbf{S}_j + J_3 \sum_{\langle\langle\langle ij \rangle\rangle\rangle} \mathbf{S}_i.\mathbf{S}_j \tag{1.40}$$

where $\langle ij \rangle$ represent the nearest neighbour links of the triangular lattice and $\langle\langle\langle ij \rangle\rangle\rangle$ represent the next-nearest neighbour links of the triangular lattice and $J_1 > 0$ is the antiferromagnetic nearest neighbour coupling and $J_3 < 0$ is the ferromagnetic next-next-nearest neighbour coupling.

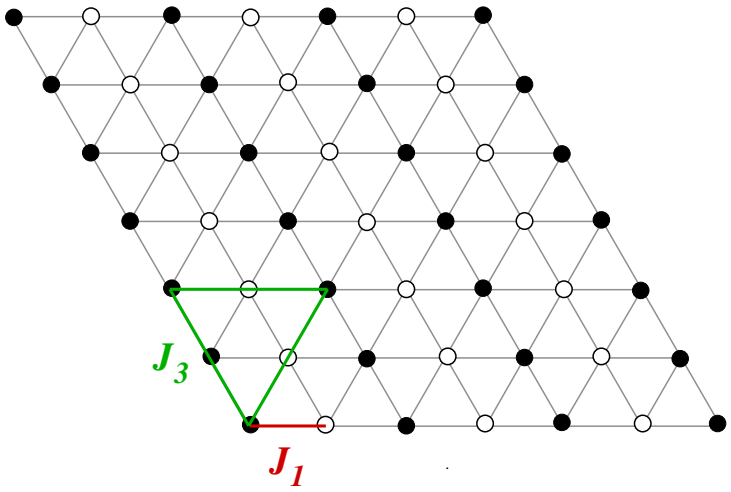

Figure 1.5: Ferromagnetic J_3 stabilises a striped ordered state in which 'up' and 'down' spins form alternating rows. The net magnetic moment of this state is zero. Shown here is one such realisation.

The striped order parameter can be defined as ϕ_μ: $(\mu = 1, 2, 3)$ with,

$$\begin{aligned}
\phi_1 &= \sum_{\vec{R}=m\hat{e}_x+n\hat{e_y}} (-1)^m S^z_{\vec{R}} \\
\phi_2 &= \sum_{\vec{R}=m\hat{e}_x+n\hat{e_y}} (-1)^n S^z_{\vec{R}} \\
\phi_3 &= \sum_{\vec{R}=m\hat{e}_x+n\hat{e_y}} (-1)^{m-n} S^z_{\vec{R}}
\end{aligned}$$

where $\vec{R} = m\hat{e}_x + n\hat{e}_y$ as shown in Fig[1.4]. The striped order phase has been shown to melt first order transition at a finite temperature[48, 49].

Recently discovered $TmMgGaO_4$ can be modelled using the effective Hamiltonian:

$$H = J_1 \sum_{\langle ij \rangle} S^z_i S^z_j + J_2 \sum_{\langle\langle ij \rangle\rangle} S^z_i S^z_j - \mu \sum_i S^z_i \tag{1.41}$$

where $i \in$ sites of a triangular lattice with $J_1, J_2 > 0$ and $J_2 \sim 0.09 J_1$ [41]. $TmMgGaO_4$ shows stripe order at zero field below $T \sim 0.27K$.

In a system with competing ferromagnetic next-nearest and ferromagnetic next-next-nearest neighbour interactions, the three-sublattice ordered phase is known to undergo a first order transition into the striped phase when the next-next-nearest neighbour interactions dominate[49] as described in Chapter 3. However, it is also interesting to understand how the three-sublattice melting transition is effected by a ferromagnetic J_3 and we also explore this in detail in Chapter 3.

1.2.9 Hard object lattice gas

Lattice gases with hard-core repulsion have been of interest as a simple lattice approximation of a fluid consisting of hard molecules as they are easy to study and yet retain excluded-volume effects. Hard objects are objects which occupy one or more lattice sites with the property that no two objects share one or more lattice sites. At full packing each lattice site uniquely belongs to a hard object. Many systems with different shapes of hard objects on different lattices have been studied using a host of analytically approximate, and numerical exact methods.. Since temperature plays no role in these systems, the ordering in such systems is entropy driven. Decreasing the density of the hard-objects usually drives the system into a disordered fluid phase. Some examples of the models studied include dimers[50, 51, 52, 53], trimers[54, 55], squares[56, 57, 58, 59, 60, 61, 62], hexagons[63], long rods[64], rectangles[65] and a mixture of squares and dimers[66]. Despite this, only few examples of an analytically exact solution exist: for a problem of hard hexagons due to Baxter[63] and some recent solutions on random lattices.[67]. Integrability of the hard hexagon problem has been compared with the non-integrability of hard squares by means of partition function roots and transfer matrix eigenvalues[68]. Recently, a model of hard squares on a square lattice (which can be thought of particles with nearest and next-nearest neighbour exclusion) was studied numerically[66]. At full packing of hard squares, the system is in a columnar ordered state (where one of the odd or even columns is preferentially occupied) with a transition of the Ashkin-Teller type to a disordered fluid as the fugacity of the hard squares is decreased. Further in this thesis, we study the problem of hard squares on a cubic lattice.

1.3 Monte-Carlo simulations

Monte-Carlo simulations of spin models involve generating an ensemble of spin configurations $\mathcal{C}$ such that the probability of the a spin configuration is proportional to the equilibrium Boltzmann weight of the spin configuration at a given temperature T. Once we have such an ensemble of configurations which occur with the right probability, we can perform measurements of various averages of various order parameters and susceptibilities on this ensemble and call it the equilibrium average. Monte-Carlo helps us do this without actually calculating the partition function of the system, since we just need to normalise the computed averages using the reduced partition function of the ensemble of configurations generated. Monte-Carlo becomes exact at infinite time, but even at finite time, good Monte-Carlo algorithms can equilibrate the systems very well and this can be checked using known methods as will be shown further in this thesis. Monte-Carlo is also limiting in the sense that the configurations that can be pro-

duced are finite, belonging to finite system sizes. Careful finite size scaling corrections to measured quantities can be used effectively to mitigate this effect. Overall Monte-Carlo algorithms are a very effective tool for gaining insights into strongly correlated many-body problems whose exact solutions are inaccessible. In the following section we start with the most basic form of Monte-Carlo called the Metropolis algorithm which produces spin configurations by flipping one spin the previous configurations. After this we go onto more complicated non-local forms of Monte-Carlo, which involve flipping a non-local amount of spins in one Monte-Carlo step.

1.3.1 Detailed balance

An important principle that the Monte-Carlo algorithms use to generate configurations that approach the probability distribution at equilibrium is called *detailed balance*. A Markov chain is a stochastic process in a configuration space consisting of spin configurations. We want the weight of each configuration $\pi_{\mathcal{C}}$ to approach the equilibrium weight. This can be achieved by the following condition:

$$\frac{P(A \to B)}{P(B \to A)} = \frac{\pi_A}{\pi_B} \tag{1.42}$$

for all pairs of configurations A and B belonging to the Markov chain. Here $P(A \to B)$ is the transition probability from A to B. Additionally ergodicity should be maintained, in the sense that every configuration in the ensemble should be a part of the Markov chain.

1.3.2 Metropolis

The Metropolis algorithm[69] as alluded to above involves generating a random spin configuration A as the starting point of the Markov chain. The next spin configuration B is produced by selecting and flipping a random spin in A. This move is accepted using the following probability:

$$P(A \to B) = \min\left[1, \frac{\pi(B)}{\pi(A)}\right] \tag{1.43}$$

It can be easily seen that this condition satisfies detailed balance. We define a few terms which will be used in the context of Monte-Carlo further on in this thesis.

Monte Carlo Step (MCS) One MCS involves flipping N spins randomly using the Metropolis algorithm before a new spin configuration is recorded in the ensemble on which the equilibrium measurements are carried out.

Warm-up time refers to the initial run of the Monte-Carlo algorithm ensuring that the

system is well equilibrated and correlations with initially chosen random spin configuration have died out. After the initial warm-up, spin configurations are recorded at every Monte-Carlo step and are stored as part of an ensemble on which the equilibrium measurements are carried out. Sometimes, the spin configurations are recorded every two MCS for better sampling and will be specified when used.
Using the above Metropolis algorithm, one can generate spin configurations on which equilibrium measurements can be made. However, in the most interesting case of critical phenomena, this algorithm is very inefficient. This can be justified by noting that the Metropolis involves local moves and at criticality the correlation length in the system diverges. In other words, every spin talks to every other spin. Hence, a Markov process which depends only on local changes will have very large autocorrelation times. In other words the time taken for a spin flip to happen will be very high thus rendering a finite time simulation highly inefficient. This is also referred to as critical slowing down. More sophisticated algorithms involving non-local spin flips are used to address this problem.

1.3.3 Cluster updates

Improvements from the Metropolis algorithm involve flipping clusters of spins. The Wolff cluster algorithm uses this method. The Wolff cluster[70] is an improvement over the Swensden-Wang algorithm[71].

Wolff cluster

We take the example of a 2d Ising spin model to illustrate this algorithm. Clusters of connected spins are constructed starting from a single spin. A connected spin is a spin pointing in the same direction as that of the cluster. So we choose a random initial spin and start building a cluster using spins that are in similarly oriented. A spin which points in the same direction as the cluster is added to the cluster with a probability $p = 1 - \exp\{-2\beta\}$. Once such a cluster is built, it is flipped with probability 1. Note that doing so satisfies the detailed balance condition. The steps in the Markov chain here are connected by cluster flips rather than spin flips. This overcomes the local constraints of flipping each spin individually and thus can speed up the process. In the case of highly frustrated systems or highly constrained models even the Wolff cluster performs unsatisfactorily and we have to resort to more sophisticated algorithms as we will see futher in this thesis.

1.3.4 Dual worm algorithms for the 2d frustrated Ising antiferromagnets

Worm algorithms are very useful as a means of generating non-local updates in Monte Carlo simulations of various lattice models (for a brief review, see Section 5.1 of Ref. [72]). The 'worm' construction typically involves creating a defect and an antidefect next to each other in the initial configuration. The location of the defect defines the fixed *tail* of the worm, while the *head* of the worm corresponds to the antidefect, which is moved through the lattice in a way which satisfies detailed balance conditions in a larger configuration space that allows for one defect-antidefect pair. The construction ends when the *head* reaches the *tail* again and annihilates it. All variables encountered during the motion of the worm are updated as a result of this construction. An early implementation of a worm algorithm in the context of classical lattice model Monte Carlo simulations was done in the high-temperature expansion representation, by updating closed path configurations through the motion of end points of a disconnected path [73]. A similar idea was also used to develop a worm algorithm for the quantum rotor model in $d = 2$ spatial dimensions using the link-current representation (divergence-free configurations of current variables on links of the equivalent classical $d + 1 = 3$ dimensional space-time lattice) [74, 75]. The construction creates a charged defect (with non-zero divergence of the link current) at the tail, and a corresponding antidefect at the head. In this case, the worm maintains detailed balance in the configuration space relevant to the sampling of the Green function of the system [76]. In quantum Monte Carlo simulations of other bosonic systems, a similar worm algorithm has been used both in the framework of imaginary time worldline formulations [77, 78], and the stochastic series expansion (SSE) approach [79] to perform non-local changes in the configuration. In this case too, the defects at the head and the tail of the worm correspond to creation and annihilation of a particle [80], allowing access to configurations relevant to the sampling of the single particle Green function. 'Dual' worm algorithms have also been used to construct cluster updates for two-dimensional classical Ising models [81]. These algorithms work by updating dimer configurations (which encode bond energies of the original model) on the corresponding dual lattice. The updated bond energies are used to obtain a new spin configuration in which an entire cluster of spins has been flipped in one update step. Recently, this approach has been used [49] to obtain efficient cluster updates for frustrated Ising models for which the usual cluster updates [71, 70] are known to perform poorly [82]. For instance, for the antiferromagnetic Ising model on the triangular lattice, bond-energy configurations correspond to dimer configuratons on the dual honeycomb lattice, with dimers intersecting frustrated bonds on the direct lattice. At $T = 0$, the dimer configuration is a perfect matching (each dual lattice site is touched by exactly one dimer). The

worm algorithm then works by creating a defect-antidefect pair in the dimer configuration. The defect corresponds to a monomer, *i.e.* a site on the dual lattice with no dimers touching it. The antidefect corresponds to an antimonomer, *i.e.* a site with two dimers touching it. The initial defect-antidefect pair is created by simply picking a site at random and pivoting the dimer touching it to another unoccupied link. The antidefect is then propagated by pivoting successive dimers along a closed path, with probabilities preserving detailed balance. The updated dimer configuration of the dual lattice is then mapped back to a new spin configuration. This ends up flipping an entire cluster of spins. At nonzero temperature, the dimer configuration is not a perfect matching since dual lattice sites with three dimers touching them are allowed, and the worm construction is suitably generalized to work with more general defect antidefect pairs.[49] The fact that all these worm constructions preserve detailed balance in a larger configuration space with one defect-antidefect pair allows for an interesting and simple method to calculate the corresponding correlation functions: The equilibrium defect-antidefect correlation function is simply proportional to the histogram of the head-to-tail separations measured during the worm propagation [83, 84, 80]. In the quantum rotor case, and in the context of worldline and SSE methods, this corresponds to the imaginary time single-particle Green function [83, 84, 80, 75]. As we detail in Chapter 2, in the example studied in the thesis here, this corresponds to the correlation function between a half-vortex and the corresponding antidefect in the argument θ of the complex three-sublattice order parameter [49]. Apart from measuring the defect-antidefect correlator during worm construction, one can also measure various statistical properties of the worms themselves; the simplest of these is the distribution of worm lengths. This is of interest because the Monte-Carlo autocorrelation properties of the worm algorithm depends on the number of variables updated in a single worm construction, which in turn depends on the distribution of worm lengths. For instance, the fractal structure and scaling properties of worms defined by the high temperature expansion have been studied previously [85]. Properties of spin clusters defined by other cluster algorithms [71, 70], have been numerically studied in the case of the critical $2d$ Ising model [86], and found to be in agreement with theoretical predictions [87, 88, 89, 90, 91]. Following the generalization of cluster algorithms to the fully frustrated square lattice [92], the properties of such clusters have also been studied extensively in that setting [93]. Since closed worms on the dual lattice define a cluster on the original lattice, properties of these clusters are also interesting from this point of view. Statistics of worms constructed by a direct worm algorithm for a three dimensional spin ice model have also been studied, but less information seems to be available on worms in the corresponding two dimensional model [94]. Part of the motivation for our work is an earlier observation that the autocorrelation properties of two rather different dual worm algorithms (DEP and myopic) [49], when used to

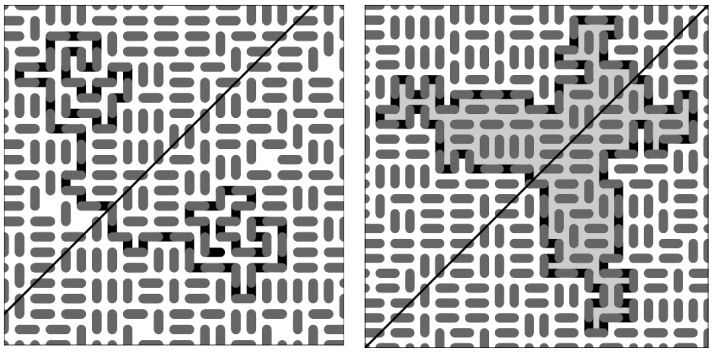

Figure 1.6: Transition graphs of initial (black) and final (gray) configurations of the pocket algorithm. Left: In the presence of monomers the graph can be open; right: transition loop touching the symmetry axis. The cluster move consists in flipping the cluster. Figure and caption taken from Ref.[95]

simulate frustrated Ising models on two different $2d$ lattices (triangular and Kagome) over a range of temperatures and further neighbor interactions for which the system displays power-law three-sublattice order, seem to be universally determined by the power-law exponent of the equilibrium spin-spin correlation function. Since the worm length distribution is expected to control the manner in which successive configurations decorrelate with each other, we attempt to understand this universality by focusing here on the worm length distribution (and related statistical properties) in this interesting regime.

1.3.5 Pocket algorithm for hard dimers

Krauth and Moessner developed a highly efficient cluster algorithm for dimers on a 2d lattice[95]. This algorithm makes use of the symmetries of the system to construct a transition graph between two dimer configurations. A transition graph can be thought of as a overlay of two dimer configurations. Fig[1.6] shows the transition graph of a dimer model on a 2d lattice with and without the presence of monomers. The pocket cluster algorithm proceeds as follows:
A randomly chosen symmetry axis $\mathcal{S}$ and an initial dimer is chosen. Two sets of geometrically identical lattices are constructed. Lattice $\mathcal{A}$ which has the initial dimer configurations and a pocket lattice $\mathcal{P}$ which is empty to begin with. The initial dimer is deleted from $\mathcal{A}$ and placed in $\mathcal{P}$. The algorithm then proceeds as a loop over all the elements in $\mathcal{P}$. Each element of $\mathcal{P}$ is taken. It is then reflected about the symmetry axis and placed in $\mathcal{A}$. This will obviously violate hard core constraints for neighbours of this reflected dimer in $\mathcal{A}$. All the dimers which violate the hardcore constraints are then removed from $\mathcal{A}$ and placed in $\mathcal{P}$. The loop over dimers in $\mathcal{P}$ is repeated until all dimers in $\mathcal{P}$ are exhausted. This will happen when a reflected dimer placed in $\mathcal{A}$ doesn't violate anymore hardcore constraints. In this process we have in fact constructed a transition

graph and flipped the initial cluster into the final cluster. Since the transition graph is symmetric about the symmetry axis $\mathcal{C}$, the interior of the transition graph even though flipped about the symmetry axis remains unchanged. In effect we have only flipped the dimers along the outer boundary of the transition graph. In this thesis we will generalise this algorithm to equilibrate hard squares on a cubic lattice.

1.4 Overview of the Thesis

In Chapter. 2 we develop a simple model for the worm length distribution of the dual worm algorithm used for the frustrated Ising model, which predicts that the worm length distribution is a power law, with the power-law exponent $(1+\theta)$ being a universal function of the equilibrium exponent η_s for spin-spin correlations at the three-sublattice ordered wavevector. Our starting point will be the well-known statement, alluded to in the Introduction that the histogram of head-to-tail distances of the worm is given by the equilibrium defect-antidefect correlator. Using standard results from the Kosterlitz-Thouless description of the power-law three-sublattice ordered phase, we conclude that the defect-antidefect correlator has a power-law form, with exponent $\eta_m = 1/4\eta_s$. Since the defect moves in a manner that preserves detailed balance (with antidefect held fixed), we interpret this power-law correlation between the defect and antidefect to be the result of a random walk performed by the defect in the presence of a static logarithmic potential that attracts it to the fixed antidefect. In this heuristic picture, the worm length is thus mapped to the time τ_r of first return to origin of a random-walker that starts at the origin and moves in a logarithmic central potential. Using standard results from random walk theory, this gives us a prediction

$$\theta = \eta_m/2 \equiv 1/8\eta_s. \tag{1.44}$$

This is our basic result. It provides a rationale for the observed universality noted earlier, and a simple parameter-free (but approximate) fit to the observed statistics of worm lengths, independent of the detailed (and somewhat complicated) worm construction protocols employed by the DEP and myopic algorithms [49]. As will be clear from the results presented here, this prediction works reasonably well (especially given its parameter-free character) both at non-zero temperature in the critical phase associated with the two-step melting of three-sublattice order, and in the zero temperature critical phase that obtains on the triangular lattice. However, clear deviations from the prediction are quite apparent in both regimes. These deviations reflect the need to have a more accurate description of the worm dynamics that goes beyond the picture of a random-walker in an effective static potential.

In Chapter. 3 we investigate the effect of increasing ferromagnetic next-next-nearest

neighbor interactions on the nature of the two-step melting transition of the three-sublattice ordered phase using sophisticated but efficient worm algorithms developed in [49]. We find that the two-step melting pinches-off into an effective single critical melting line (which separates the three-sublattice ordered phase and a paramagnet), which on further increasing the strength of the ferromagnetic next-next-nearest neighbor interactions resolves into a first-order melting transition. To further characterize this effective critical line we turn to the six-state clock model studied by Cardy [96] for reasons explained below. The six-fold symmetric ground state of the six-state clock model has a similar two-step melting transition with an intermediate power-law ordered phase which pinches-off via a multi-critical point into a first order line. A self-dual line whose equation is known passes through this multi-critical point [96, 97]. Simulating parameter values and comparing the extracted critical exponents along this one dimensional line allows us to numerically determine this multi-critical point and thus verify a conjuncture by Dorey et. al. that this multi-critical point lies in the universality class of the Z_6 parafermionic CFT constructed and solved by Zamolodchikov and Fateev [98]. On comparing the scaling behavior of the binder cumulants constructed from the three-sublattice order parameter and the ferromagnetic order parameter in the triangular lattice model with the binder cumulants constructed from corresponding order-parameters in the six-state clock model we find similarities which helps us predict the location of a possible multi-critical point M_c in the effective critical line that we observe in the triangular lattice model. We were then able to numerically obtain the value of the critical exponents with high accuracy along this effective critical line and we find that at the predicted M_c the critical exponents are comparable to the exactly calculated values of the Z_6 parafermionic CFT within error-bars.

In Chapter. 4 we study a model of hard squares at full packing on a cubic lattice using local Monte Carlo moves and cluster Monte Carlo algorithms. Clusters are constructed using global reflection symmetries of the partition function. Each hard square can be assigned a direction (its normal) to define three types of hard squares: x,y and z. At the isotropic point, when the fugacities of all three types of hard squares are equal, we find that the system is in a sublattice ordered state. We also study the evolution of the system as a function of anisotropy in the fugacities. As the fugacity of z type hard square, z_z is reduced relative to z_x and z_y we find that the system undergoes a continuous transition into a bi-layered phase. These bi-layers are occupied predominantly by x and y type hard squares with relatively few z type hard squares. Each bilayer, when viewed along the z axis, can be thought of as a square lattice with a mixture of dimers and hard squares at close to full packing. The dimers correspond to the x and y type hard squares lying entirely within the bi-layer and hard squares correspond to the z type hard squares. The rare x and y type hard squares that straddle two bi-layers correspond to a dimer defect on both the bi-layers that they touch. This allows an

analogy to the recently studied problem of hard-squares and dimers at full packing on the square lattice[66]. In this analogy, decreasing the fugacity of z type hard squares would then decrease the fugacity of hard squares in the two dimensional problem. Most of the correlation between different bilayers is transmitted by rare x and y hard squares that straddle two bilayers. We further wish to explore this analogy in future work.

Chapter 2

Statistical properties of worm algorithms

2.1 Models

Ising models on triangular and kagome lattices with antiferromagnetic nearest neighbor interactions are among the simplest models of geometric frustration [17, 99]. For these models, the pattern of nearest-neighbour bond energies can be represented in terms of dimer models on the corresponding dual lattice (honeycomb and dice respectively) [49]. When further neighbour interactions are absent, there is a macroscopic degeneracy of minimum energy spin configurations, which corresponds to a $T = 0$ ensemble of dimer configurations on the dual lattice. For the triangular lattice antiferromagnet, this $T = 0$ ensemble is made up of all perfect matchings (fully-packed dimer configurations) on the honeycomb lattice, while the $T = 0$ dimer configurations on the dice lattice have exactly one dimer touching each three-coordinated site and an even number of dimers touching each six-coordinated site. The former ensemble has power-law dimer correlations with power-law exponent $\eta_d = 2$ (at the uniform and the three-sublattice wavevectors). This corresponds to power-law three-sublattice order for the spins, with power-law exponent $\eta_s = 1/2$ at $T = 0$ [17, 43]. The Kagome lattice antiferromagnet in this limit is a short-range correlated spin liquid [99], corresponding to short-range dimer correlations.

At $T = 0$ for the nearest neighbour triangular antiferromagnet, the relationship between η_d and η_s can be understood in terms of a coarse-grained height model [83, 100, 101, 102] description of the ensemble of fully-packed dimer configurations on the honeycomb lattice. In this representation, the spin operator at the three sublattice wavevector corresponds to $\exp(i\pi h)$ (where h is the height field) while the dimer operator has a uniform part given in terms of the gradient ∇h and a second piece $\exp(2\pi i h)$ at the three-sublattice wavevector. Dimer correlations at the uniform wavevector fall of

as $1/r^2$ independent of the stiffness of the height model, while correlations at the three-sublattice wavevector decay with power-law exponent η_d controlled by the stiffness of the height model. Spin correlations at the three-sublattice wavevector fall of as a power law with exponent η_s (with $\eta_d = 4\eta_s$). When all fully-packed dimer configurations have equal weight, $\eta_d = 2$.

A second-neighbour ferromagnetic interaction J_2 on the triangular lattice, with $|J_2| \propto T$ in the $T \to 0$ limit, favours three-sublattice ordered fully-packed dimer configurations over others, and gives rise to a $\eta_d < 2$ and $\eta_s < 1/2$. Indeed, η_s decreases monotonically with increasing $|J_2|/T$ (in this zero temperature limit), until the system develops long-range three-sublattice order when $\eta_s = 1/9$ is reached [101]. In the coarse-grained height representation, this is understood by noting that $|J_2|/T$ tunes the stiffness of the height model, thereby influencing the value of η_s (and of $\eta_d = 4\eta_s$). Monomers in this fully-paked dimer model correspond, in the Coulomb gas (CG) description of the coarse-grained height model [83, 102], to a magnetic charge $+1$ (antimonomers have magnetic charge -1). As a result, the monomer-antimonomer correlator decays as a power law with an exponent $\eta_m = 1/\eta_d = 1/4\eta_s$. In terms of the argument θ of the complex three-sublattice order parameter of the spin model, these monomers are half-vortices.

A fixed nonzero value of second-neighbor ferromagnetic interaction induces long-range three-sublattice order on both lattices at low enough temperature, which can then melt via a two-step process, wherein the intermediate state has power-law ordered spin correlations at the three-sublattice wavevector, with power-law exponent η_s that ranges from $1/9$ (at the low-temperature end) to $1/4$ (at the high-temperature end) [101, 47, 22]. When spin correlations display power-law three-sublattice order, the dimer correlations also have a power-law form, with exponent $\eta_d = 4\eta_s$. At non-zero T, the dimer representation of bond-energies now allows defects with three dimers touching a three-coordinated site, greatly increasing the entropy of allowed configurations. The worm algorithm now makes other defects (Section. 2.2) apart from monomers. However, we can still think of these defects as half-vortices (or the corresponding antidefect) in the argument θ [103, 104, 105] of the fourier component of the spin density at the three-sublattice wavevector. Since the power-law ordered phase is described by a Gaussian theory for θ, the defect-antidefect correlator is again expected to decay with exponent $\eta_m = 1/4\eta_s = 1/\eta_d$ (where η_d, the dimer correlation exponent, is again related to the power-law exponent η_s via $\eta_d = 4\eta_s$). [See Fig.2.1]

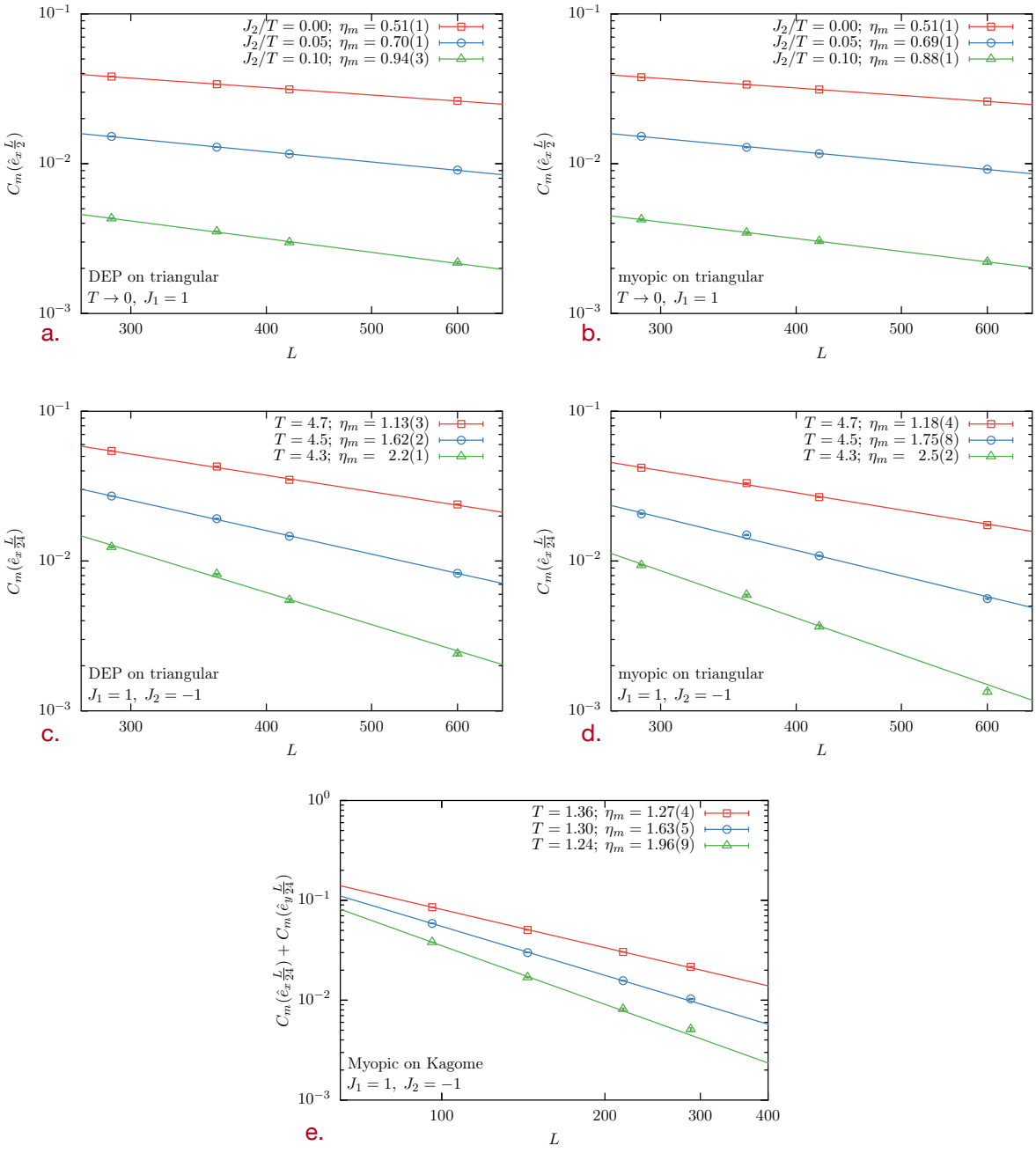

Figure 2.1: The lattice size L dependence of the defect correlator $C_m\left(\frac{L}{24}\right)$ at separation $\frac{L}{24}$ on periodic $L \times L$ Kagome lattices using the myopic worm algorithm for three values of T at which the system is in the power-law ordered critical phase. Lines denote fits to a power-law form $\propto 1/L^{\eta_m}$.

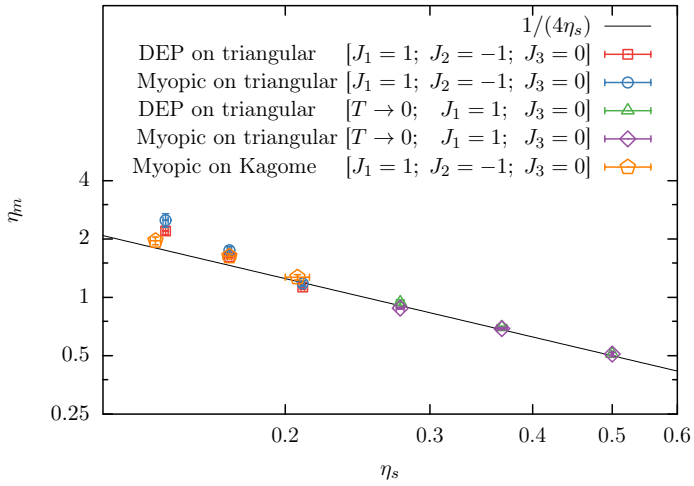

Figure 2.2: η_m extracted from the L dependence of defect correlator as a function of η_s in simulations employing the DEP and myopic worm algorithms. The line denotes the theoretically expected dependence $\eta_m = 1/4\eta_s$.

2.2 Algorithms

2.2.1 Dual Representation and dual worm updates

We begin with a summary of the dual representation of the frustrated Ising antiferromagnet on the triangular lattice: One represents every configuration of the triangular lattice Ising model in terms of configurations of dimers on links of the dual honeycomb lattice, with a dimer placed on every dual link that intersects a *frustrated* nearest neighbour bond of the triangular lattice (Fig. 4.1). For our purposes here, a frustrated bond of the triangular lattice is one that connects a pair of spins pointing in the same direction. When $J_1 > 0$ (corresponding to the interesting case of frustrated antiferromagnetism), this implies that every *minimally frustrated* spin configuration, which minimizes the nearest-neighbour exchange energy by ensuring that every triangle of the triangular lattice has exactly one frustrated bond, corresponds to a defect-free dimer cover of the dual honeycomb lattice, in which there is exactly one dimer touching each dual site of the honeycomb lattice.

At non-zero temperature, more general configurations also contribute to the partition sum. These have a nonzero density of *defective triangles*, *i.e.* triangles in which all three spins are pointing in the same direction. In dual language, these correspond to honeycomb lattice sites with three dimers touching the site. Thus, in dual language, the configuration space at nonzero temperature is that of a generalized honeycomb lattice dimer model, with either one or three dimers touching each dual site. This dimer model inherits boundary conditions from the original spin model: We choose to work with $L_x \times L_y$ samples with periodic boundary conditions on the Ising spins along two

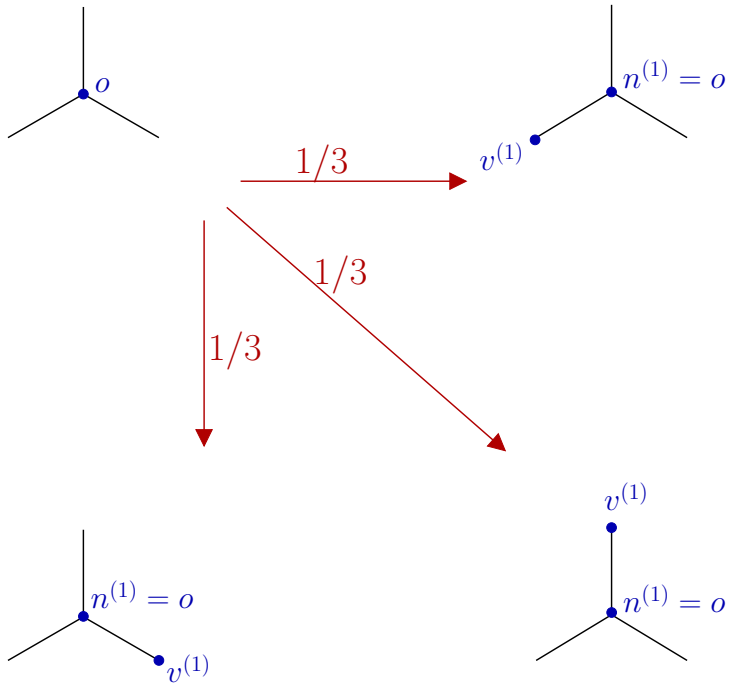

Figure 2.3: The first step of the myopic worm construction on the dual honeycomb lattice: A start site o is chosen randomly. The tail of the worm remains static at this start site until the worm construction is complete. In this first step, the head of the worm moves to one of the three neighbours of the start site with probability $1/3$, regardless of the local dimer configuration. The neighbour thus reached is our first vertex site $v^{(1)}$. Viewed from the point of view of this vertex, the start site o is the first entry site $n^{(1)}$.

principal directions $\hat{x}$ and $\hat{y}$ of the triangular lattice. This translates to global constraints on the dual description which are spelled out in detail when we describe our algorithm.

All of this generalizes readily to the Kagome lattice antiferromagnet. The idea is again to work with the dual representation in terms of a generalized dimer model on the dual lattice. The dual lattice is now the dice lattice, which is a bipartite lattice with one sublattice of three-coordinated sites and a second sublattice of six-coordinated sites (Fig. 4.1). Every spin configuration on the Kagome lattice corresponds to a dimer configuration on the dice lattice, with either one or three dimers touching the three-coordinated sites, and an even number of dimers touching the six-coordinated sites. As before, a frustrated bond is one that connects a pair of nearest neighbour spins pointing in the same direction, and is represented by a dimer on the dual link that is perpendicular to this bond. Minimally frustrated spin configurations, that minimize the nearest-neighbour exchange energy, now correspond to dimer configurations with exactly one dimer touching each three-coordinated dice lattice site. Periodic boundary conditions of the $L_x \times L_y$ spin system again translate to global constraints (see below).

The dual worm approach,[81] on which both cluster algorithms are based, is rather simple to explain in general terms: One first maps the spin configuration of the system

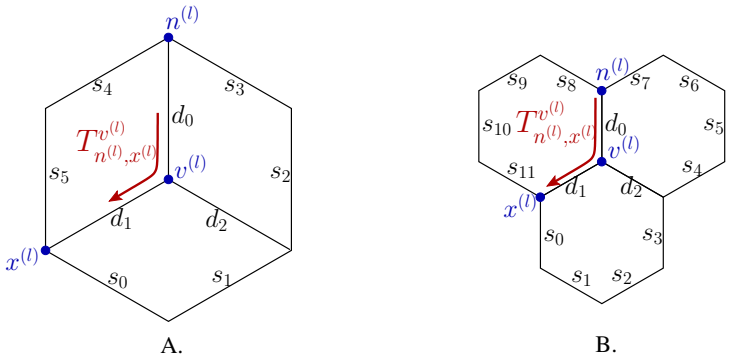

Figure 2.4: The probabilistic step of the myopic algorithm: After arriving at the vertex site $v^{(l)}$ from the entry site $n^{(l)}$ we choose to exit via $x^{(l)}$ (which is one of the neighbours of $v^{(l)}$) with probability given by the probability table T. A) When the spin interactions extend upto next-next-nearest neighbours on the Kagome lattice, knowledge of the local dimer configuration consisting of dimer states from s_0 to s_5 and d_0, d_1 and d_2 suffices to compute entries of the table T. B) When the spin interactions extend upto next-next-nearest neighbours on the triangular lattice, knowledge of the local dimer configuration consisting of dimer states from s_0 to s_{11} and d_0, d_1 and d_2 suffices to to compute entries of T.

to the corresponding dual configuration of dimers. Each dimer configuration is thus assigned a Boltzmann weight of the "parent" spin configuration from which it was obtained. Next, one updates the dual dimer configuration in a way that preserves detailed balance. In this way, one obtains a new dimer configuration, which is then checked to see if it satisfies certain global winding number constraints (spelled out in detail below) that must be obeyed by any dimer configuration that is dual to a spin configuration with periodic boundary conditions. If the global constraints are satisfied, one maps the new dimer configuration back to spin variables, to obtain an updated spin configuration which can differ from the original spin configuration by large nonlocal changes. Since the procedure explicitly satisfies detailed balance, one obtains in this way a valid algorithm for the spin model being studied.

For the triangular lattice Ising antiferromagnet, we have developed two strategies for constructing rejection-free updates of the generalized dimer model on the dual honeycomb lattice. As mentioned in the Introduction, one of these generalizes readily to the generalized dice lattice dimer model which is dual to the frustrated Kagome lattice Ising model, while the other is specific to the generalized honeycomb lattice dimer model.

The strategy that generalizes readily to the dice lattice case is one in which we deliberately *do not* keep track of the local dimer configuration of the dual lattice at alternate steps of the worm construction in order to ensure that detailed balance can be satisfied without any final rejection step. Since this strategy involves being deliberately short-sighted at alternate steps of the construction, we dub this the "myopic"

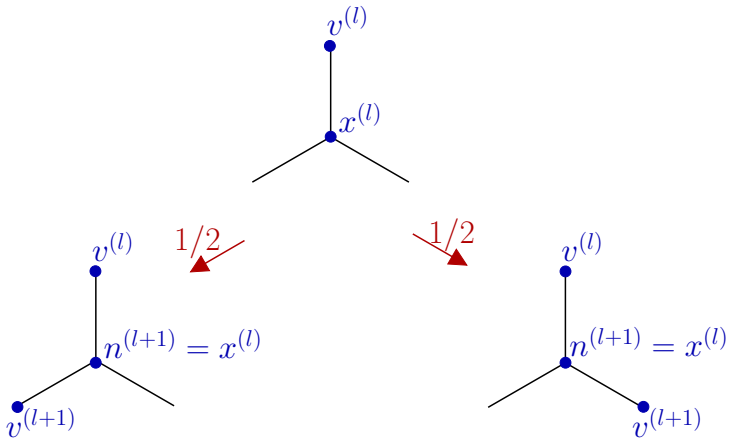

Figure 2.5: The *myopic* step of the myopic worm algorithm on the dual honeycomb lattice: After arriving at an exit site $x^{(l)}$ from a vertex site $v^{(l)}$, the next vertex site $v^{(l+1)}$ is chosen to be one of the two *other* neighbours of $x^{(l)}$ with probability $1/2$. Viewed from this new vertex site $v^{(l+1)}$, $x^{(l)}$ becomes the entry site $n^{(l+1)}$.

worm algorithm. Below we begin with a detailed description of how this works for the generalized dimer models on the honeycomb and dice lattices which are dual to the physics of the frustrated Ising models on the triangular and Kagome lattices.

2.2.2 Myopic worm algorithm

On the honeycomb lattice this myopic worm algorithm consists of the following steps: We begin by choosing a random "start site" o on the honeycomb lattice. Regardless of the local dimer configuration in the vicinity of this site, we move from the start site to one of the three neighbouring sites, with probability $1/3$ each (Fig. 2.3). The neighbouring site reached in this way is our first "vertex site" $v^{(1)}$. In our terminology, we have "entered" this vertex site from the start site o. Therefore, the start site is the "entry site" $n^{(1)}$ for this vertex. Next, we choose one of the neighbours of $v^{(1)}$ as the "exit site" $x^{(1)}$, via which we can exit this vertex. When we arrive at vertex site $v^{(1)}$ from entry site $n^{(1)}$, and leave this vertex site via exit site $x^{(1)}$, we flip the dimer state of the dual links $\langle n^{(1)} v^{(1)} \rangle$ and $\langle v^{(1)} x^{(1)} \rangle$. The choice of exit site $x^{(1)}$ via which we exit from a vertex site $v^{(1)}$, given that we arrived at vertex site $v^{(1)}$ from a particular entry site $n^{(1)}$, is probabilistic (Fig. 2.4), with probabilities specified in a probability table T whose structure we now discuss.

For any vertex site v encountered in our process, these probabilities are given by a probability table T^v_{nx}, where n is the entry site from which we have entered the vertex and x is the exit site we wish to leave from. Entries in this probability table are constrained by the requirement of local detailed balance. In order to state these constraints on T^v in a way that makes subsequent analysis easy, we rewrite this table as a three-by-three matrix M^v_{ij} $(i, j = 1, 2, 3)$ by choosing a standard convention to label the three

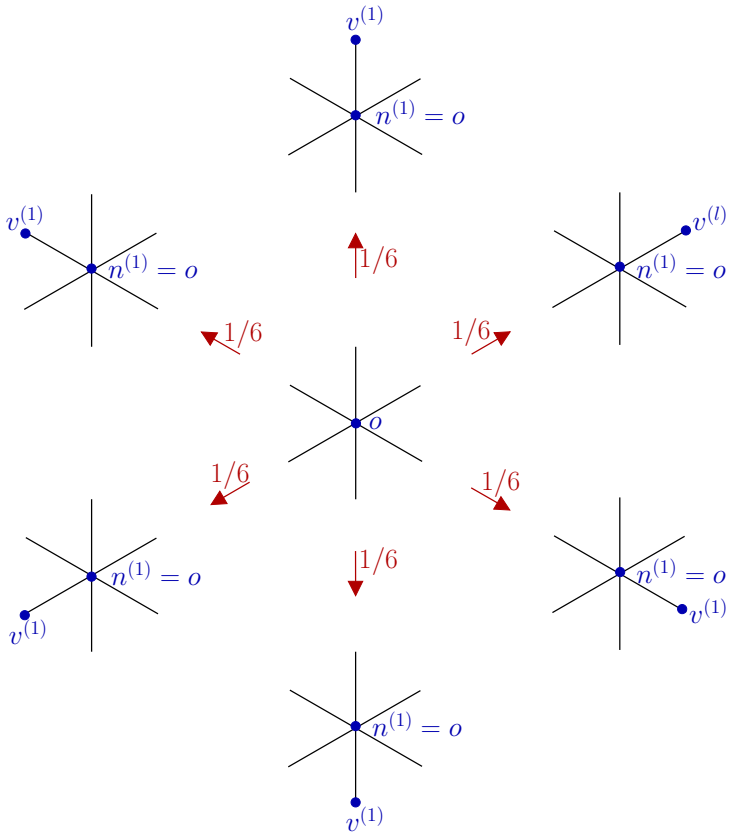

Figure 2.6: The first step of the myopic worm construction on the dual dice lattice: A start site o is chosen randomly from one of the six-coordinated sites on the dice lattice. The tail of the worm remains static at this start site until the worm construction is complete. In this first step, the head of the worm moves to one of the six neighbours of the start site with probability $1/6$, regardless of the local dimer configuration. The neighbour thus reached is our first vertex site $v^{(1)}$. Viewed from the point of view of this vertex, the start site o is the first entry site $n^{(1)}$.

neighbours of v by integers running from one to three. Thus, if n is the i^{th} neighbour of v and x is the j^{th} neighbour of v according to this convention, we write $T^v_{nx} = M^v_{ij}$.

We denote by w^v_n the Boltzmann weight of the dual dimer configuration before we flip the dimer states of dual links $\langle nv\rangle$ and $\langle vx\rangle$. In the same way, w^v_x, for each choice of x, denotes the corresponding Boltzmann weight after these flips are implemented. As is usual for all worm algorithms, these weights for the intermediate configurations encountered during this myopic construction are obtained from the Boltzmann weight of the generalized dimer model with the proviso that the "infinite energy cost" of violating the generalized dimer constraints at the start site and current site ("head" and "tail" of the worm in worm algorithm parlance) are ignored when keeping track of the weights of these intermediate configurations.

We choose the T matrices to satisfy a local detailed balance condition that depends

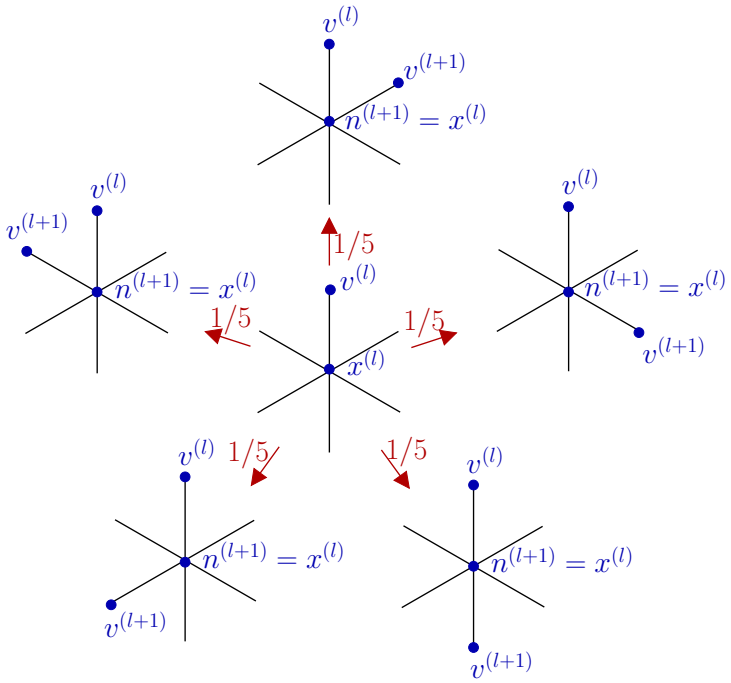

Figure 2.7: The *myopic* step of the myopic worm algorithm on the dual dice lattice: After arriving at an exit site $x^{(l)}$ (which, by construction, is always a six-coordinated site) from a vertex site $v^{(l)}$, the next vertex site $v^{(l+1)}$ is chosen to be one of the five *other* neighbours of $x^{(l)}$ with probability $1/5$. Viewed from this new vertex site $v^{(l+1)}$, $x^{(l)}$ becomes the entry site $n^{(l+1)}$.

on these weights

$$w_n^v T_{nx}^v \quad = \quad w_x^v T_{xn}^v \; . \tag{2.1}$$

Rewriting $w_n^v \equiv W_i^v$ if n is the i^{th} neighbour of v, and $w_x^v \equiv W_j^v$ if x is the j^{th} neighbour of v, we can write these detailed balance conditions in terms of the matrix M_{ij}^v and the weights W_i^v (with $i, j = 1, 2, 3$) as

$$W_i^v M_{ij}^v = W_j^v M_{ji}^v \; , \tag{2.2}$$

As is usual in the analysis of such detailed balance constraints, we define the three-by-three matrix $A_{ij}^v = W_i^v M_{ij}^v$ and note that the detailed balance condition is now simply the statement that A^v is a symmetric matrix which satisfies the three constraints

$$\sum_j A_{ij}^v \quad = \quad W_i^v \; for \; i = 1, 2, 3 \tag{2.3}$$

For interactions that extend up to next-next-nearest neighbours on the triangular lattice, the three weights W_i^v that enter these equations differ from each other only

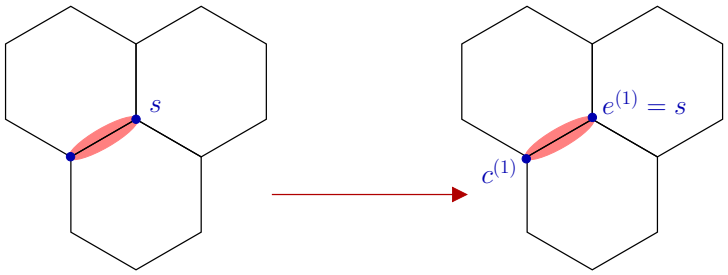

Figure 2.8: If the randomly chosen start site s is touched by only one dimer, we move along that dimer to reach a new pivot site $c^{(1)}$ in the first step of the DEP worm construction. The start site s becomes our first entry site $e^{(1)}$.

due to factors that depend on the dimer state, d_0, d_1, d_2 of the the three links emanating from v and the twelve dual links surrounding v, whose dimer state has been denoted s_0, $s_1 \ldots s_{11}$ in Fig. 2.4. This feature allows us to tabulate all possible local environments of v, and analyse these constraint equations in advance to determine and tabulate the A^v (and thence determine M^v) in advance. In practice, if the weights permit it, we use the "zero-bounce" solution given in Ref. [106] and Ref. [107], else the "one-bounce" solution given there.

Having reached the exit $x^{(1)}$ of the vertex $v^{(1)}$ in this manner, we now need to choose the next vertex $v^{(2)}$ which we will enter next from this site $x^{(1)}$. This is the myopic part of our procedure: *This next vertex $v^{(2)}$ is randomly chosen to be one of the two other neighbours of $x^{(1)}$ (other than the previous vertex $v^{(1)}$) with probability $1/2$ each*(Fig. 2.5). After making this choice, $x^{(1)}$ becomes the entry site $n^{(2)}$ for this next vertex $v^{(2)}$, and the previous probabilistic procedure is repeated at this next vertex $v^{(2)}$ in order to choose the next exit site $x^{(2)}$ from which we will exit $v^{(2)}$.

In this manner, we go through a sequence of vertices until the exit site $x^{(k)}$ of the $k^{\rm th}$ vertex equals the start site o. When this happens, one obtains a new dimer configuration which again has either one dimer touching each honeycomb site, or three dimers touching a honeycomb site. This new dimer configuration can be accepted with probability one since our procedure builds in detailed balance with respect to the Boltzmann weight of the generalized dimer model.

It is straightforward to prove this explicitly using the notation we have developed above. To this end, we first note that the forward probability for constructing a particular worm to go from an initial configuration $\mathcal{C}_i$ to a final configuration $\mathcal{C}_f$ takes on the product form

$$P(\mathcal{C}_i \to \mathcal{C}_f) \;=\; \frac{1}{3} \times T^{v^{(1)}}_{n^{(1)}x^{(1)}} \frac{1}{2} T^{v^{(2)}}_{n^{(2)}x^{(2)}} \ldots \frac{1}{2} T^{v^{(k)}}_{n^{(k)}x^{(k)}} \tag{2.4}$$

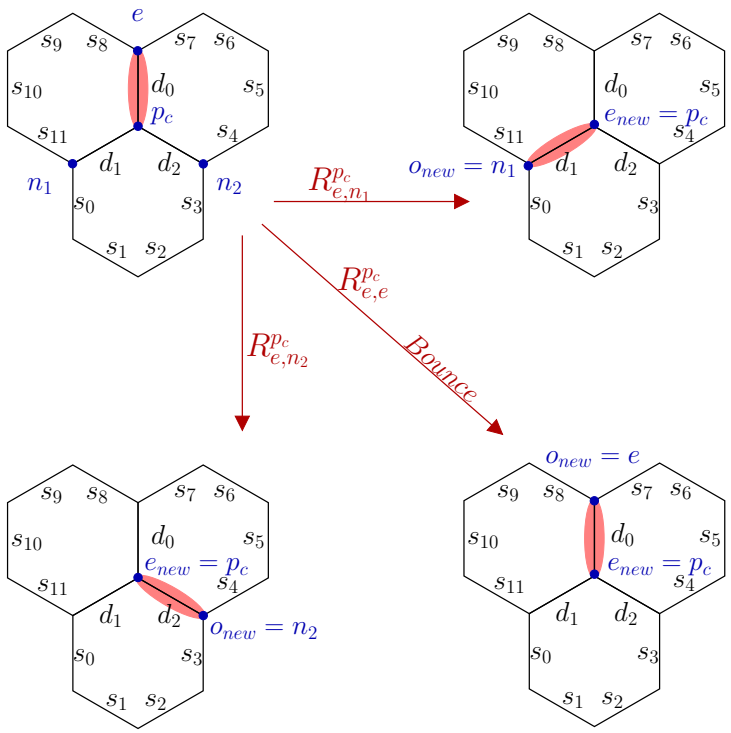

Figure 2.9: The pivot step of the DEP worm construction when one arrives at a central pivot site p_c from an entry site e and there is only one dimer touching p_c. We pivot the dimer from the link $\langle p_c e\rangle$ to the link $\langle p_c o_{new}\rangle$ with probabilities determined by the corresponding elements of the probability table R. o_{new}, which is the new overlap site, can either one of the two neighbours n_1 and n_2 of the central pivot site p_c or the entry site e from which we came to p_c. The central pivot site p_c now becomes the new entry site e_{new} from which this new overlap site o_{new}has been reached, and the next step is an overlap step. On the dual honeycomb lattice, knowledge of the local dimer configuration consisting of dimer states from s_0 to s_{11} and d_0, d_1 and d_2 suffices to calculate R when the interactions extend up to next-next-nearest neighbours on the triangular lattice.

while the reverse probability takes the form

$$P(\mathcal{C}_f \to \mathcal{C}_i) \;=\; \frac{1}{3} \times T^{v^{(k)}}_{x^{(k)} n^{(k)}} \frac{1}{2} T^{v^{(k-1)}}_{x^{(k-1)} n^{(k-1)}} \cdots \frac{1}{2} T^{v^{(1)}}_{x^{(1)} n^{(1)}} \tag{2.5}$$

As noted earlier, while the weights w that appear in the intermediate steps of the construction are computed ignoring the violation of the generalized dimer constraints at two sites, the initial and final weights $w^{v^{(1)}}_{n^{(1)}}$ and $w^{v^{(k)}}_{x^{(k)}}$ have no such caveats associated with them. Indeed, we have

$$w^{v^{(1)}}_{n^{(1)}} \;\equiv\; w(\mathcal{C}_i)\;, \tag{2.6}$$

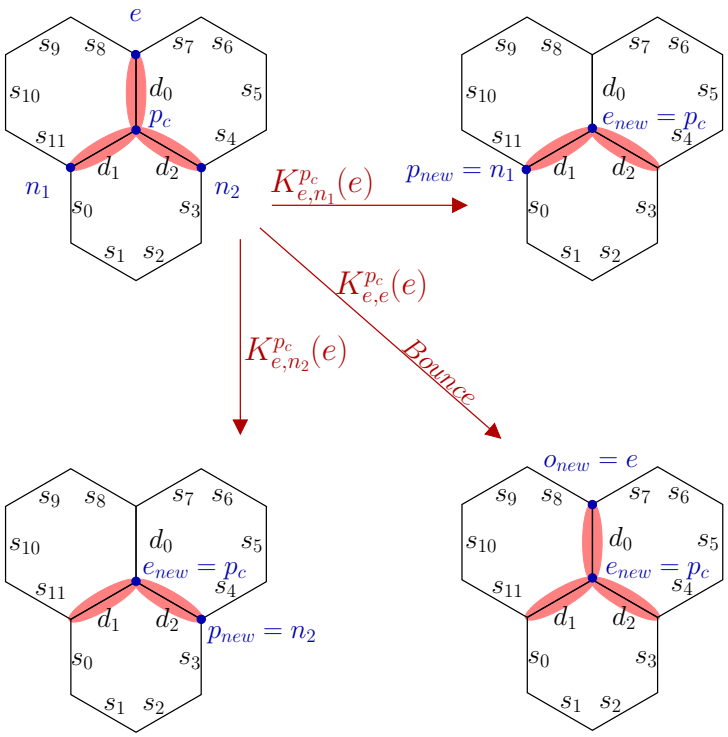

Figure 2.10: The pivot step of the DEP worm construction when one arrives at a central pivot site p_c from an entry site e and there are three dimers touching p_c: At this point, one has three options, with probabilities determined by corresponding entries of the probability table K: We can choose to exit to one of the two neighbours n_1 or n_2, or bounce back to the entry site e. If we choose to exit through either n_1 or n_2, we move along the dimer connecting the central pivot site p_c to this chosen exit which becomes our new pivot site p_{new}, and delete the dimer on the link $\langle p_c e\rangle$. The third option is to move along the dimer connecting the central pivot site p_c back to the entry site e, and e then becomes our new overlap site o_{new}. On the dual honeycomb lattice, knowledge of the local dimer configuration consisting of dimer states from s_0 to s_{11} and d_0, d_1 and d_2 suffices to determine K when the interactions extend upto next-next-nearest neighbours on the triangular lattice.

the physical Boltzmann weight of the initial configuration, while

$$w^{v^{(k)}}_{x^{(k)}} \equiv w(\mathcal{C}_f)\ , \tag{2.7}$$

the physical Boltzmann weight of the final configuration.

Now, since our choice of transition probabilities obeys

$$w^{v^{(p)}}_{n^{(p)}} T^{v^{(p)}}_{n^{(p)}x^{(p)}} = w^{v^{(p)}}_{x^{(p)}} T^{v^{(p)}}_{x^{(p)}n^{(p)}} \tag{2.8}$$

for all $p = 1, 2 \ldots k$, and since

$$w^{v^{(p)}}_{x^{(p)}} \equiv w^{v^{(p+1)}}_{n^{(p+1)}} \tag{2.9}$$

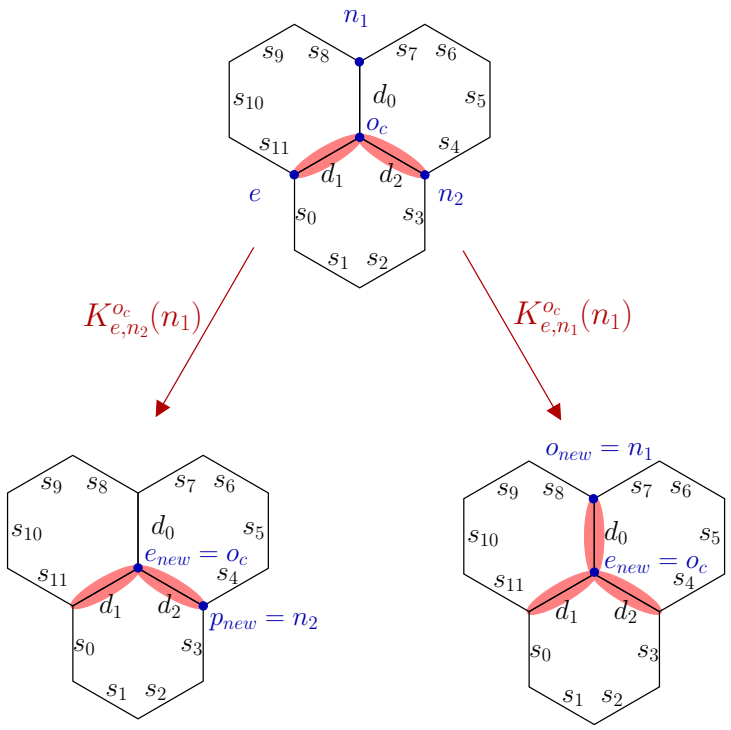

Figure 2.11: The overlap step of the DEP worm construction: One arrives at a central overlap site o_c from an entry site e. At this stage, one uses the probability table K to choose one out of two options: If we choose to exit along the empty link (in this case $\langle o_c n_1 \rangle$), we *deposit* a dimer on the empty link, and move along it making n_1 our new overlap site o_{new}. The central overlap site o_c now becomes the new entry site e_{new} from which we enter the new overlap site o_{new}. On the other hand, we may choose to exit along the link $\langle o_c n_2 \rangle$ to reach our new pivot site $p_{new} = n_2$. The central overlap site o_c now becomes the new entry site e_{new}, from which we enter the new pivot site p_{new}. On the dual honeycomb lattice, knowledge of the local dimer configuration consisting of dimer states from s_0 to s_{11} and d_0, d_1 and d_2 suffices to determine the probability table K, when the interactions extend upto next-next-nearest neighbours on the triangular lattice.

for all $p = 1, 3 \ldots k-1$, we may write the following chain of equalities

$$
\begin{aligned}
& w(\mathcal{C}_i) P(\mathcal{C}_i \to \mathcal{C}_f) = \\
& = w^{v^{(1)}}_{n^{(1)}} \times \frac{1}{3} T^{v^{(1)}}_{n^{(1)} x^{(1)}} \frac{1}{2} T^{v^{(2)}}_{n^{(2)} x^{(2)}} \cdots \frac{1}{2} T^{v^{(k)}}_{n^{(k)} x^{(k)}} \\
& = \frac{1}{3} \times T^{v^{(1)}}_{x^{(1)} n^{(1)}} w^{v^{(1)}}_{x^{(1)}} \frac{1}{2} T^{v^{(2)}}_{n^{(2)} x^{(2)}} \cdots \frac{1}{2} T^{v^{(k)}}_{n^{(k)} x^{(k)}} \\
& = \frac{1}{3} \times T^{v^{(1)}}_{x^{(1)} n^{(1)}} w^{v^{(2)}}_{n^{(2)}} \frac{1}{2} T^{v^{(2)}}_{n^{(2)} x^{(2)}} \cdots \frac{1}{2} T^{v^{(k)}}_{n^{(k)} x^{(k)}} \\
& = \frac{1}{3} \times T^{v^{(1)}}_{x^{(1)} n^{(1)}} \frac{1}{2} T^{v^{(2)}}_{x^{(2)} n^{(2)}} w^{v^{(2)}}_{x^{(2)}} \cdots \frac{1}{2} T^{v^{(k)}}_{n^{(k)} x^{(k)}} \\
& \ldots \\
& = w^{v^{(k)}}_{x^{(k)}} \times \frac{1}{3} T^{v^{(k)}}_{x^{(k)} n^{(k)}} \frac{1}{2} T^{v^{(k-1)}}_{x^{(k-1)} n^{(k-1)}} \cdots \frac{1}{2} T^{v^{(1)}}_{x^{(1)} n^{(1)}} \\
& = w(\mathcal{C}_f) P(\mathcal{C}_f \to \mathcal{C}_i)
\end{aligned}
\tag{2.10}
$$

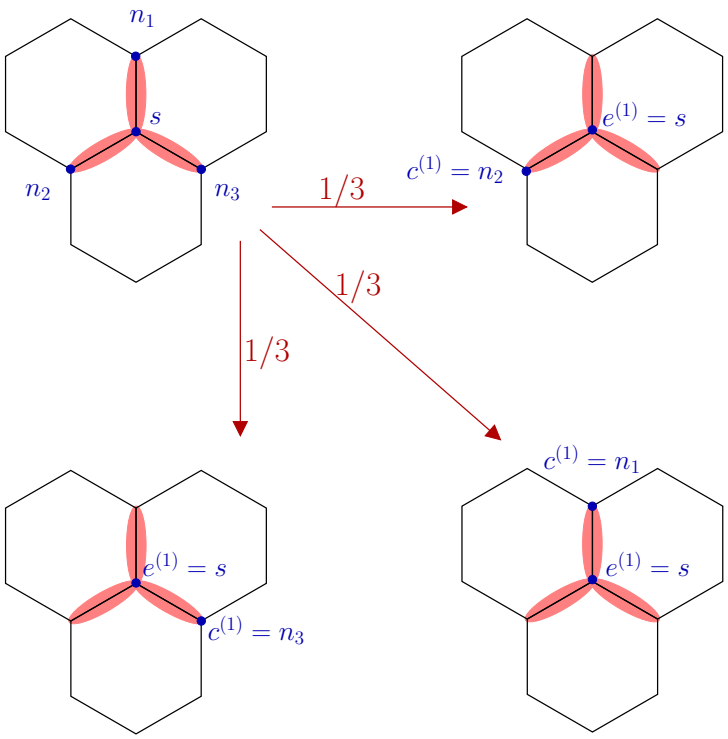

Figure 2.12: The first step of the DEP worm construction when the randomly chosen start site s is touched by three dimers: We move along any one of the three dimers with probability $1/3$, to reach a new pivot site $c^{(1)}$. The start site s becomes our first entry site $e^{(1)}$.

Thus, our procedure explicitly obeys detailed balance, and this myopic worm construction provides a rejection-free update scheme that can effect large changes in the configuration of a generalized honeycomb lattice dimer model with one or three dimers touching each honeycomb site.

To translate back into spin language, we need to take care of one additional subtlety: Although the procedure outlined above gives us a rejection-free nonlocal update for the generalized dimer model with Boltzmann weight inherited from the original spin system, we cannot translate this directly into a rejection-free nonlocal update for the original spin system since we are working on a torus with periodic boundary conditions for the spin system. The reason has to do with the fact that the periodic boundary conditions of the spin system translate to a pair of global constraints: In every valid dimer configuration obtained from a spin configuration with periodic boundary conditions, the number of empty links crossed by a path looping around the torus along $\hat{x}$ or $\hat{y}$ must be even, since the absence of a dimer on a dual link perpendicular to a given bond of the spin system implies that the spins connected by that bond are antiparallel. This corresponds to constraints on the global winding numbers of the corresponding dimer model, which must be enforced by any Monte Carlo procedure. Note that these constraints are on the parity of these winding numbers, which are in any case only defined modulo 2 unless one is at $T = 0$.

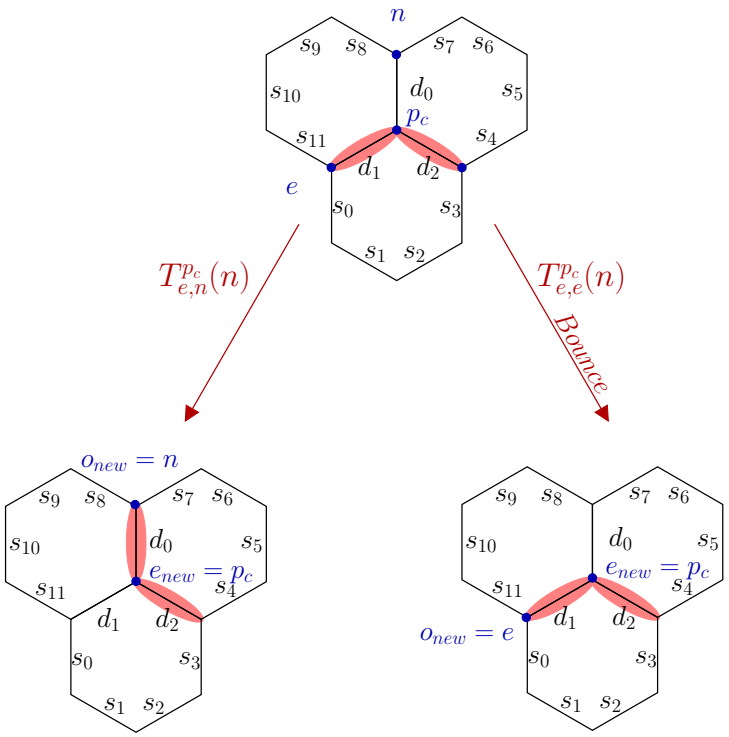

Figure 2.13: The pivot step of the DEP worm construction when one arrives at a central pivot site p_c from an entry site e, and there are two dimers touching p_c: We can exit to the neighbour n, which is the neighbour not connected to the central pivot site p_c by a dimer, or bounce back by exiting through the entry site e. If we choose to exit through the neighbour n, we flip the dimer on the link $\langle p_c e\rangle$ to the link $\langle p_c n\rangle$. We then move along this dimer to reach our new overlap site $o_{new} \equiv n$. If we choose to bounce back, the entry site e becomes our new overlap site o_{new}. The central pivot site p_c now becomes our new entry site e_{new} in either case. The probability table T is used to determine which option is chosen. On the dual honeycomb lattice, knowledge of the local dimer configuration consisting of dimer states from s_0 to s_{11} and d_0, d_1 and d_2 suffices to calculate T when the interactions extend upto next-next-nearest neighbours on the triangular lattice.

Therefore, to convert this rejection-free myopic worm update procedure for dimers into a valid update scheme for the original spin system, we test the winding numbers (modulo 2) of the new dimer configuration to see if it satisfies these two global constraints. If the answer is yes, we translate the new dimer configuration back into spin language by choosing the spin at the origin to be up or down with probability $1/2$ and reconstructing the remainder of the spin configuration from the positions of the dimers. If, however, the new dimer configuration is in an illegal winding sector, we repeat the previous spin configuration in our Monte Carlo chain.

This procedure generalizes readily to the Kagome lattice Ising antiferromagnet with interactions extending up to next-next-nearest neighbour spins. Since most of the required generalizations are self-evident, we merely point out some of the key differences here. Our myopic worm update procedure now begins with a randomly chosen six-

coordinated site as the start site o. With probabilities $1/6$ each, we choose one of its neighbours as the first vertex site $v^{(1)}$ (Fig. 2.6). The start site o thus becomes the entry site $n^{(1)}$ from which we enter the first vertex $v^{(1)}$. The choice of the first exit site $x^{(1)}$ via which we exit the first vertex is again dictated by a three-by-three probability table (Fig. 2.4).

For any vertex v, this probability table is determined by solving detailed balance equations completely analogous to the ones displayed earlier for the honeycomb lattice case. In the dice lattice case, the three weights W_i^v depend on the dimer states s_0, s_1 $\ldots$ s_5 of the six dual links shown in Fig. 2.4, and on the dimer states d_0, d_1, d_2 of the three links emanating from v. Therefore, we are again in a position to solve these equations for all possible local environments of v and tabulate these solutions for repeated use during the worm construction.

As in the honeycomb case, having arrived at $x^{(1)}$, we choose the next vertex $v^{(2)}$ in a myopic manner: Without regard to the local dimer configuration, we randomly pick, with probability $1/5$ each, one of the other neighbours (other than $v^{(1)}$) of $x^{(1)}$ as the next vertex $v^{(2)}$ (Fig. 2.7). $x^{(1)}$ now becomes the entry site $n^{(2)}$ from which we enter this second vertex $v^{(2)}$. The exit $x^{(2)}$ is again chosen from the pre-tabulated probability table, and the process continues until the k^{th} exit $x^{(k)}$ equals then start site o.

Clearly, our earlier proof of detailed balance goes through unchanged, and this myopic worm construction again gives a rejection-free way of updating the dual dimer model in accordance with detailed balance. To translate this into an update scheme for the original spin model, we must again check that the new dimer configuration is in a legal winding sector, and if the new configuration is in an illegal winding sector, we must repeat the original spin configuration in our Monte Carlo chain.

2.2.3 DEP worm algorithm

The other strategy we have developed is specific to the honeycomb lattice dimer model that is dual to the triangular lattice Ising antiferromagnet. Since it involves deposition, evaporation, and pivoting of dimers, we dub this the DEP worm algorithm. The DEP worm construction begins by choosing a random start site s. The subsequent worm construction consists of so-called "overlap steps" and "pivot steps". Pivot steps are carried out when one reaches a "central" "pivot site" from a neighbouring "entry site", while overlap steps are carried out when one reaches a central "overlap site" from a neighbouring entry site. Details of some of the subsequent pivot steps in this construction depend on whether the randomly chosen start site s is touched by three dimers or by one dimer, *i.e.* if the corresponding triangle is defective or minimally frustrated. Therefore we describe these two branches of the procedure separately, but use a unified notation so as to avoid repetition of the aspects that do not depend on the branch

chosen.

Branch I

Let us first consider the case when the randomly chosen start site s is touched by exactly one dimer(Fig. 2.8). In this case, we move along the dimer touching s to its other end. The site at the other end of this dimer becomes our first central site $c^{(1)}$, at which we must now employ a pivot step with $c^{(1)}$ as the first pivot site. For the purposes of this first pivot step, the start site s becomes the entry site $e^{(1)}$ from which we have arrived at this pivot site $c^{(1)}$ by walking along this dimer.

Before proceeding further, it is useful to elucidate the nature of a general pivot move encountered in our algorithm: In a pivot step, after one arrives at the central pivot site $p_{\rm c}$ from an entry site e (as we will see below, e could be the previous overlap site $o_{\rm old}$, or a previous pivot site $p_{\rm old}$) by moving along a dimer connecting e to $p_{\rm c}$, the subsequent protocol depends on whether there is exactly one dimer (Fig. 2.9) touching $p_{\rm c}$ or three (Fig. 2.10). In the first case, one pivots the dimer touching $p_{\rm c}$, so that it now lies on link $\langle p_{\rm c} o_{\rm new}\rangle$ instead of link $\langle p_{\rm c} e\rangle$(Fig. 2.9). Here, $o_{\rm new}$ is one of the neighbours of $p_{\rm c}$, chosen using the element $R^{p_{\rm c}}_{e,o_{\rm new}}$ of a three-by-three probability table $R^{p_{\rm c}}_{\alpha,\beta}$ (where α and β range over the three neighbours of the central site $p_{\rm c}$, and the full structure of this table is specified at the end of this discussion). Note that in some cases, it is possible for $o_{\rm new} = e$ with nonzero probability, if the corresponding diagonal entry of the table is nonzero. After this is done, the next step in the construction will be an overlap step, with $o_{\rm new}$ being the central overlap site and $p_{\rm c}$ playing the role of the new entry site $e_{\rm new}$ from which we have arrived at this central overlap site. The structure of a general overlap step is specified below, after describing the pivot move in the second case, *i.e.* with three dimers touching the central pivot site.

If the central pivot site $p_{\rm c}$ in a pivot step has three dimers connecting it (Fig. 2.10) to its three neighbours n_1, n_2, and e (where e is the entry site from which we arrived at the central pivot site $p_{\rm c}$), we choose one out of three alternatives using a different probability table $K^{c_s}_{\alpha,\beta}(n_p)$, where α and β range over all neighbours of a central site c_s and n_p is a particular privileged neighbour of c_s (in the case being described here, $c_s = p_{\rm c}$ and $n_p = e$): With probabilities $K^{p_{\rm c}}_{e,n_1}(e)$ and $K^{p_{\rm c}}_{e,n_2}(e)$ drawn respectively from this table, we may delete the dimer on link $\langle p_{\rm c} e\rangle$ and reach either n_1 or n_2, and the next step would then be a pivot step, with the neighbour thus reached now playing the role of the new central pivot site $p_{\rm new}$ and $p_{\rm c}$ playing the role of the new entry site $e_{\rm new}$ from which we have reached this new central pivot site. On the other hand, we may "bounce" with probability $K^{p_{\rm c}}_{e,e}(e)$, *i.e.* we simply return from $p_{\rm c}$ to e without deleting any of the three dimers touching $p_{\rm c}$; in this case, the next step will be an overlap step, with e as the new central overlap site $o_{\rm new}$, and $p_{\rm c}$ will play the role of the new entry site

$e_{\rm new}$ from which we have reached this new overlap site (Fig. 2.10). Note that elements of this table $K^{c_s}_{\alpha,\beta}(n_p)$ with $\alpha \neq n_p$ never play any role in the choices made at this kind of pivot step. As we will see below, these elements of the table in fact determine the choices made at a general overlap step in a way that preserves local detailed balance.

Returning to our construction, if the central pivot site $c^{(1)}$ was of the second type and we did not bounce, we would reach a new central pivot site $c^{(2)}$ (with $c^{(1)}$ now becoming the entry site $e^{(2)}$ from which we reach this new pivot site), and we would perform another pivot step as described above. If on the other hand, the central pivot site $c^{(1)}$ was of this first type or if it was of the second type and we bounced, the next step will be an overlap step with a new central overlap site $c^{(2)}$. Since we would have reached $c^{(2)}$ by moving along a dimer connecting it to $c^{(1)}$, $c^{(1)}$ will play the role of the new entry site $e^{(2)}$ for this overlap step (in the bounce case, $c^{(2)} = e^{(1)}$). Having reached the central overlap site $c^{(2)}$ from entry site $e^{(2)}$ in this way, we must employ an overlap step.

Before proceeding with our construction, let us first elucidate the structure of choices at an overlap step after we have reached a central overlap site o_c from an entry site e. e could be the previous pivot site $e = p_{\rm old}$ if the previous step had been a pivot step (as in the example above) or it could be a previous overlap site $e = o_{\rm old}$ if the previous step had also been an overlap step (we will see below that this is also possible). In either case, at a general overlap step, one arrives at the overlap site o_c from entry site e along one of the two dimers touching o_c. Thus, one neighbour of o_c, suggestively labelled $o_{\rm new}$, is *not* connected to the central overlap site o_c by a dimer, while the other two neighbours are connected to o_c by dimers. One of the latter pair of neighbours is of course the entry site e from which we arrived at o_c, while we suggestively label the other as $p_{\rm new}$.

At such an overlap step, one always has two options to choose from, whose probabilities are given as follows by entries of the probability table K introduced earlier(Fig 2.11): One option is to deposit, with probability $K^{o_c}_{e,o_{\rm new}}(o_{\rm new})$, an additional dimer on the originally empty link $\langle o_c o_{\rm new}\rangle$ emanating from o_c. If we do this, $o_{\rm new}$ becomes the new overlap site, which we have entered from o_c, which becomes the new entry site $e_{\rm new}$, and the next step will again be an overlap step. The second option, chosen with probability $K^{o_c}_{e,p_{\rm new}}(o_{\rm new})$, is that we move along the second dimer touching o_c to the other neighbour $p_{\rm new}$, which is connected to o_c by this second dimer. If we do this, $p_{\rm new}$ becomes the new pivot site, which we enter from site o_c, which becomes the new entry site $e_{\rm new}$, and the next step will be a pivot step. As we will see below, the fact that the table K that fixes the probabilities for choosing between these two options is the same as the one used in a pivot step (when the pivot site has three dimers touching it) is crucial in formulating and satisfying local detailed balance conditions that guarantees a rejection-free worm update.

Returning again to our construction, we employ this procedure to carry out an overlap step when we reach the overlap site $o^{(2)}$ from entry site $e^{(2)}$. Clearly this process continues until we encounter the start site s as the new overlap site in the course of our worm construction. When this happens, we obtain a new dimer configuration that satisfies the generalized dimer constraint that each site be touched by one or three dimers.

Branch II

Let us now consider the case when the randomly chosen start site s is touched by three dimers. In this case, we move along one of the three dimers touching s to its other end (with probability $1/3$ each), so that the site at the other end becomes the central pivot site $c^{(1)}$ for a pivot step, and the start site s becomes the entry site $e^{(1)}$ from which we have entered this central pivot site (Fig 2.12). We now implement the protocol for a pivot step (as described in *Branch I*) to reach a new central site $c^{(2)}$. If the next step turns out to be a pivot step, $c^{(2)}$ plays the role of a central pivot site, whereas it becomes the central overlap site if the next step is an overlap step. In either case, $c^{(1)}$ becomes the entry site $e^{(2)}$ for this next step. In this manner, we continue until we reach the start site s as the new central overlap site $c^{(k)}$ for an overlap step. When this happens, the worm construction ends after these k steps, since the start site again has three dimers touching it, and we thus obtain a new dimer configuration that satisfies the generalized dimer constraint that each site be touched by one or three dimers.

The only additional feature introduced in *Branch II* is that one could in principle reach the start site s as the central pivot site of some intermediate pivot step l(Fig. 2.13). In this case, the intermediate configuration reached at this $l^{\rm th}$ step is not a legal one (since it still has two dimers touching s), and we need to continue with the worm construction. This is done using a special "two-by-two" pivot step(Fig. 2.13). In this two-by-two pivot step, one arrives at the two-by-two pivot site (which will always be the start site in our construction) p_c from an entry site e (as in all other steps, e could be a previous central overlap site $o_{\rm old}$ or the previous central pivot site $p_{\rm old}$) by moving along a dimer connecting e to p_c. Unlike the usual pivot step, at which there is only one dimer touching the central pivot site, p_c has a second dimer touching it, which connects p_c to another neighbour n_f. Thus, unlike the usual pivot step, there is just one neighbour of p_c, suggestively labelled $o_{\rm new}$, which is not connected to p_c by a dimer when one arrives at p_c to implement this step. Therefore, our only options are to rotate the dimer which was on link $\langle ep_c\rangle$, to now lie on link $\langle p_c o_{\rm new}\rangle$, or to bounce. The probabilities for these two choices are determined by a probability table $T^{p_c}_{\alpha,\beta}(n_f)$. Here, α and β are both constrained to not equal n_f, making $T^{p_c}_{\alpha,\beta}(n_f)$ a two-by-two matrix. In either case, $o_{\rm new}$ chosen in one of these two ways becomes the new central overlap site

of the next step, which must be an overlap step, and the process continues.

This new configuration thus obtained upon completing the worm construction initiated either using *Branch I* or *Branch II* can now be accepted with probability one if the probabilities with which we carried out each of the intermediate pivot steps and overlap steps obeyed local detailed balance. Local detailed balance at a pivot step in which the pivot site is touched by one dimer requires that the probability table $R^{p_c}_{e,o_f}$ obeys the conditions

$$w^{p_c}_e R^{p_c}_{e,o_f} \;=\; w^{p_c}_{o_f} R^{p_c}_{o_f,e} \;, \tag{2.11}$$

where the $w^{p_c}_n$ is the Boltzmann weight of the dimer configuration in which the link $\langle p_c n\rangle$ connecting p_c to one of its neighbours n is occupied by a dimer and the other two links emanating from p_c are empty. As in all worm constructions, these weights are computed ignoring the fact that the generalized dimer constraint (that each site be touched by exactly one or three dimers) is violated at two sites on the lattice. These conditions again form a three-by-three set of constraint equations of the type discussed in Ref. [107] and Ref. [106], allowing us to analyze these constraints and tabulate solutions in advance for all cases that can be encountered. If the weights permit it, we use the "zero-bounce" solution given in Ref. [107] and Ref. [106], else the "one-bounce" solution given there.

Local detailed balance at a two-by-two pivot step in which the pivot site is touched by two dimers requires that the probability table $T^{p_c}_{\alpha,\beta}(n_f)$ obeys the conditions

$$w^{p_c}_\alpha(n_f) T^{p_c}_{\alpha,\beta}(n_f) \;=\; w^{p_c}_\beta(n_f) T^{p_c}_{\beta,\alpha}(n_f) \;, \tag{2.12}$$

where the $w^{p_c}_\alpha(n_f)$ is the Boltzmann weights of the dimer configurations in which the links $\langle p_c n_f\rangle$ and $\langle p_c \alpha\rangle$ are covered by dimers and the third link is empty. As always, these weights are computed ignoring the fact that the dimer constraints are violated at two sites on the dual lattice. In practice, we tabulate all possible local environments that can arise in such an update step, and use Metropolis probabilities to tabulate in advance the corresponding entries of $T^{p_c}(n_f)$.

Finally, the constraints imposed by local detailed balance at an overlap step are essentially intertwined with the local detailed balance constraints that must be enforced at a pivot step when the pivot site has three dimers touching it. This is because the deletion of a dimer at such a pivot step is the "time-reversed" counterpart of the process by which an additional dimer is deposited at an overlap step. Indeed, this is why we have been careful in our discussion above to draw the probabilities at the pivot step from the same table K as the probabilities that govern the choices to be made at an overlap step.

We use a different probability table $K^{c_s}_{\alpha,\beta}(n_p)$ (where α and β range over all neighbours of a central site c_s and n_p is a particular privileged neighbour of c_s) to decide on the next course of action:

We now describe the structure of the table $K^{c_s}_{\alpha,\beta}(n_p)$. Here, c_s is the central site, which would be the current pivot site in a pivot step with three dimers touching the pivot site, or the current overlap site in an overlap step. n_p is a "privileged neighbour" of c_s; in a pivot step, n_p is the entry site from which we enter the pivot site c_s, while in an overlap step, it is the unique neighbour of c_s that is not connected to c_s by a dimer. Clearly, local detailed balance imposes the following constraints on this probability table K:

$$w^{c_s}_{\alpha}(n_p)K^{c_s}_{\alpha,\beta}(n_p) \;=\; w^{c_s}_{\beta}(n_p)K^{c_s}_{\beta,\alpha}(n_p)\;. \tag{2.13}$$

Here both α and β can be either the site n_p or the two other neighbours n_1 and n_2 of the central site c_s. $w^{c_s}_{n_1}(n_p) = w^{c_s}_{n_2}(n_p)$ denotes the weight of the configuration with both links $\langle c_s n_1\rangle$ and $\langle c_s n_2\rangle$ covered by a dimer and the link $\langle c_s n_p\rangle$ unoccupied by a dimer. On the other hand, $w^{c_s}_{n_p}(n_p)$ denotes the weight of the configuration in which all three links $\langle c_s n_1\rangle$, $\langle c_s n_2\rangle$ and $\langle c_s n_p\rangle$ are covered by dimers. As before, these weights are computed ignoring the fact that the generalized dimer constraint (that each site be touched by exactly one or three dimers) is violated at two sites on the lattice.

Choices for the tables R and K consistent with these local detailed balance constraints, can be computed using the same strategy described in our construction of the myopic worm update. Again, the weights that enter these constraints on K (R) depend only on the dimer states d_0, d_1, and d_2 of the three links emanating from the central site c_s (pivot site p_c), and the dimer states s_0, $s_1 \ldots s_{11}$ of the twelve links surrounding this site, allowing us to tabulate in advance all possible local environments and the corresponding solutions for K and R. The formal proof of detailed balance uses these local detailed balance constraints to construct a chain of equalities relating the probabilities for an update step and its time-reversed counterpart in exactly the same way as the proof given in the previous discussion of the myopic worm update. Therefore, we do not repeat it here for the present case.

With this background, we use the DEP and myopic algorithms [49] in the triangular case and the myopic algorithm in the Kagome case to simulate the classical Ising model

$$H \;=\; J_1 \sum_{\langle RR'\rangle} \sigma_R\sigma_{R'} + J_2 \sum_{\langle\langle RR'\rangle\rangle} \sigma_R\sigma_{R'}\;, \tag{2.14}$$

where $\langle RR'\rangle$ and $\langle\langle RR'\rangle\rangle$ denote nearest-neighbor and next-nearest-neighbor links of the lattice in question, and $\sigma_R = \pm 1$ are the Ising spins on sites R of the triangular

or kagome lattice. In our convention, $J_{1/2} > 0$ corresponds to an antiferromagnetic coupling, while $J_{1/2} < 0$ correspond to a ferromagnetic coupling. We focus here on the case with $J_1 > 0$ and $J_2 < 0$, and study the statistics of worms generated by these algorithms in the power-law three-sublattice ordered phase on both lattices.

2.3 Random walker in a logarithmic potential with absorbing boundary conditions

As mentioned earlier, we model the worms created by the worm algorithms by making a heuristic connection to a random walk in a central logarithmic potential. The idea is simple: The worm construction proceeds by moving a defect at the head of the worm through the dual lattice until it comes back to its initial location and annihilates with the tail (at which an antidefect is held fixed). Since the equilibrium defect-antidefect correlator in the power-law three-sublattice ordered phase is also of a power-law form and since the worm construction preserves detailed balance in the enlarged configuration space with one defect and one anti-defect, we take the point of view that the head of the worm performs a random walk while interacting with the fixed tail via a static potential determined by the logarithm of the equilibrium defect-antidefect correlator. In other words, the worm construction can be thought of as a random walk in a central potential $V(r) = -\ln(C_{\text{defect}}(r)) = k_B T \eta_m \ln(r)$.

With this motivation, we now recapitulate some standard results for the return time statistics of a d-dimensional continuous-time random walker in an attractive radial potential $V(r) = \tilde{A} \ln r$ with $\tilde{A}/k_B T = \eta_m$. To obtain the statistics of first return times, we impose an absorbing boundary condition at the origin. This boundary condition implies that the walk ends when the walker reaches its origin. The Langevin equation reads:

$$\frac{d\boldsymbol{r}}{dt} = -\frac{\tilde{A}}{r}\hat{\boldsymbol{r}} + \boldsymbol{\xi}(t), \tag{2.15}$$

with,

$$\langle \xi_i(t)\xi_j(t')\rangle = 2k_B T \delta_{ij}\delta(t-t') \tag{2.16}$$

where $i, j = 1, ..., d$.

The equivalent Fokker-Planck equation for the probability distribution $P(r,t)$ for the position of the walker at time t is:

$$\frac{dP}{dt} = k_B T \boldsymbol{\nabla} \cdot \left(\frac{A}{r}\hat{r}P + \boldsymbol{\nabla} P \right) \tag{2.17}$$

with $A = \tilde{A}/k_B T$.

Since the potential is radially symmetric, we can define the radial probability distri-

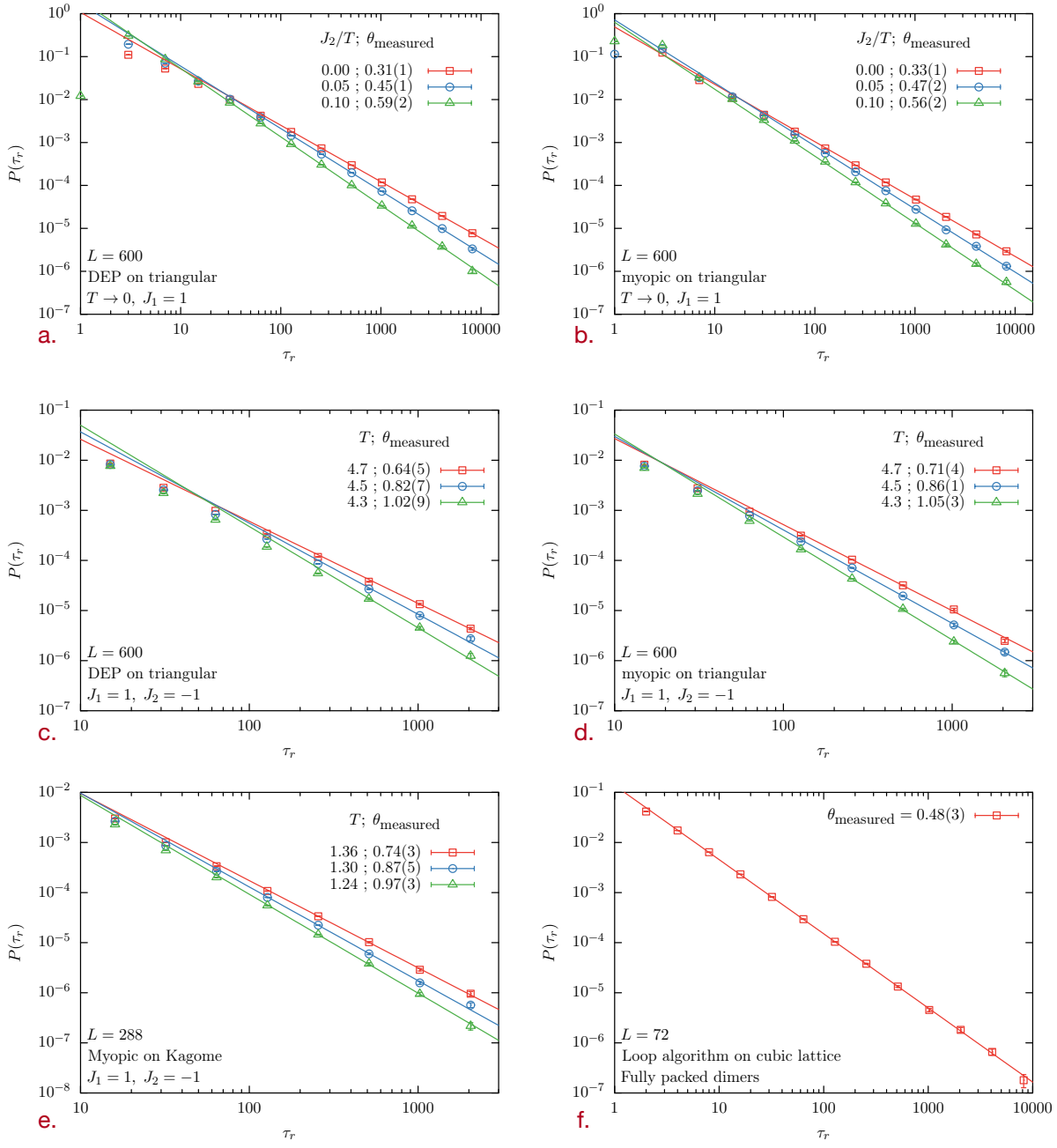

Figure 2.14: Probability distribution $P(\tau_r)$ of the number of sites of the dual lattice visited (τ_r) in one completed worm of the myopic algorithm for a 288×288 Kagome lattice for three values of T at which the system is in the power-law ordered critical phase. Lines denote fits to a power-law form $\propto \frac{1}{{\tau_r}^{1+\theta_{\text{measured}}}}$.

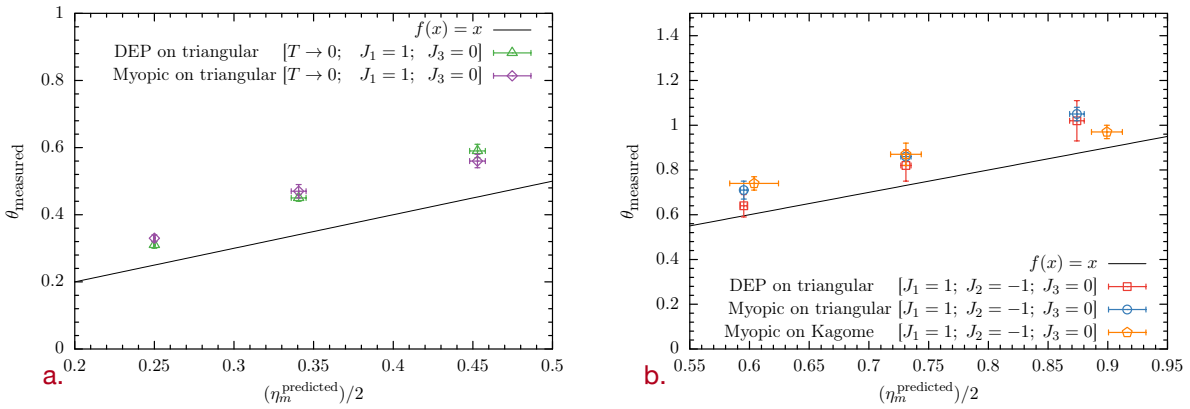

Figure 2.15: The persistence exponent θ extracted from $P(\tau_r)$ as a function of η_m in simulations employing the DEP and myopic worm algorithms. The line denotes the expected dependence in dimension $d < 2$.

bution by writing $\boldsymbol{r} = (r, \Omega)$ and integrating over the angle variable as:

$$Q(r,t) = r^{d-1} \int d\Omega P(r,\Omega,t) \tag{2.18}$$

Eq.(2.17) then reduces to a one-dimensional Fokker-Planck equation:

$$\frac{\partial Q}{\partial t} = k_B T \frac{\partial}{\partial r}\left(\frac{b}{r}Q + \frac{\partial Q}{\partial r}\right) \tag{2.19}$$

where $b = A + 1 - d$

For a free random walk in an effective dimension d', the corresponding one dimensional Fokker-Planck equation would be

$$\frac{\partial Q}{\partial t} = k_B T \frac{\partial}{\partial r}\left(\frac{b'}{r}Q + \frac{\partial Q}{\partial r}\right) \tag{2.20}$$

where $b' = 1 - d'$.

Thus a random walker in an attractive central potential in dimension d can be viewed as a free random walker in an effective dimension d', with

$$d' = d - A \tag{2.21}$$

The survival probability of a random walk $S(t)$, is the probability that the random walk has not reached its origin. If $S(t)$ decays as a power law, the exponent of the power law is defined as the 'persistence exponent' θ in random walk literature. The probability of first return to origin $F(0,t) = -\partial S(t)/\partial t$ for a random walker in dimension d' has

been calculated as [108, 109]:

$$F(0,t) = \begin{cases} 1/t^{2-(d'/2)}, & \text{for } d' < 2 \\ 1/(t\ln^2(t)), & \text{for } d' = 2 \\ 1/t^{(d'/2)}, & \text{for } d' > 2 \end{cases} \tag{2.22}$$

In terms of the persistence exponent θ,

$$F(0,t) \propto 1/t^{1+\theta}. \tag{2.23}$$

Thus,

$$\theta \propto \begin{cases} 1-(d'/2), & \text{for } d' < 2 \\ (d'/2)-1, & \text{for } d' > 2 \end{cases} \tag{2.24}$$

For $d' = 2$, the survival probability decays logarithmically and the persistence exponent is not defined. Since $A \equiv \eta_m$ and $d = 2$, we find $d' = 2 - \eta_m$. Also since $\eta_m \in (1/2, 9/4)$ (see below) is always positive, $d' < 2$ throughout the power-law regimes studied here.

Thus we obtain

$$\theta = \eta_m/2 \equiv 1/8\eta_s. \tag{2.25}$$

in the power-law regimes studied here.

2.4 Observables

Defect-antidefect correlator: During the worm construction, a defect-antidefect pair is created on the dual lattice, and the antidefect is then moved (keeping the defect fixed) through the dual lattice (in a manner satisfying detailed balance in the enlarged configuration space) until it returns to the location of the defect and annihilates it, producing a legal dimer configuration that can be mapped back to a spin configuration. As noted earlier, the defect-antidefect correlator $C_m(\vec{r})$ is proportional to the histogram of the *head* to *tail* distance $\vec{r}_m$ which can be accumulated during the worm construction [83]. We choose a normalization convention where this histogram, when summed over $\vec{r}$, gives the mean length of worms constructed by the algorithm (in other words, we measure the number of times the head to tail separation is $\vec{r}$ per worm). In the power-law three-sublattice ordered phase we expect $C_m(\vec{r}) \sim 1/r^{\eta_m}$, with $\eta_m = 1/4\eta_s$.. During the worm construction, the worm can wind across the periodic boundary conditions of the lattice. Even if the worm winds before annihilating, we always record the geometric distance between the head and tail of the worm (modulo the lattice size L in each direction).

Worm length or "return time" distribution: The number of dual lattice sites (with

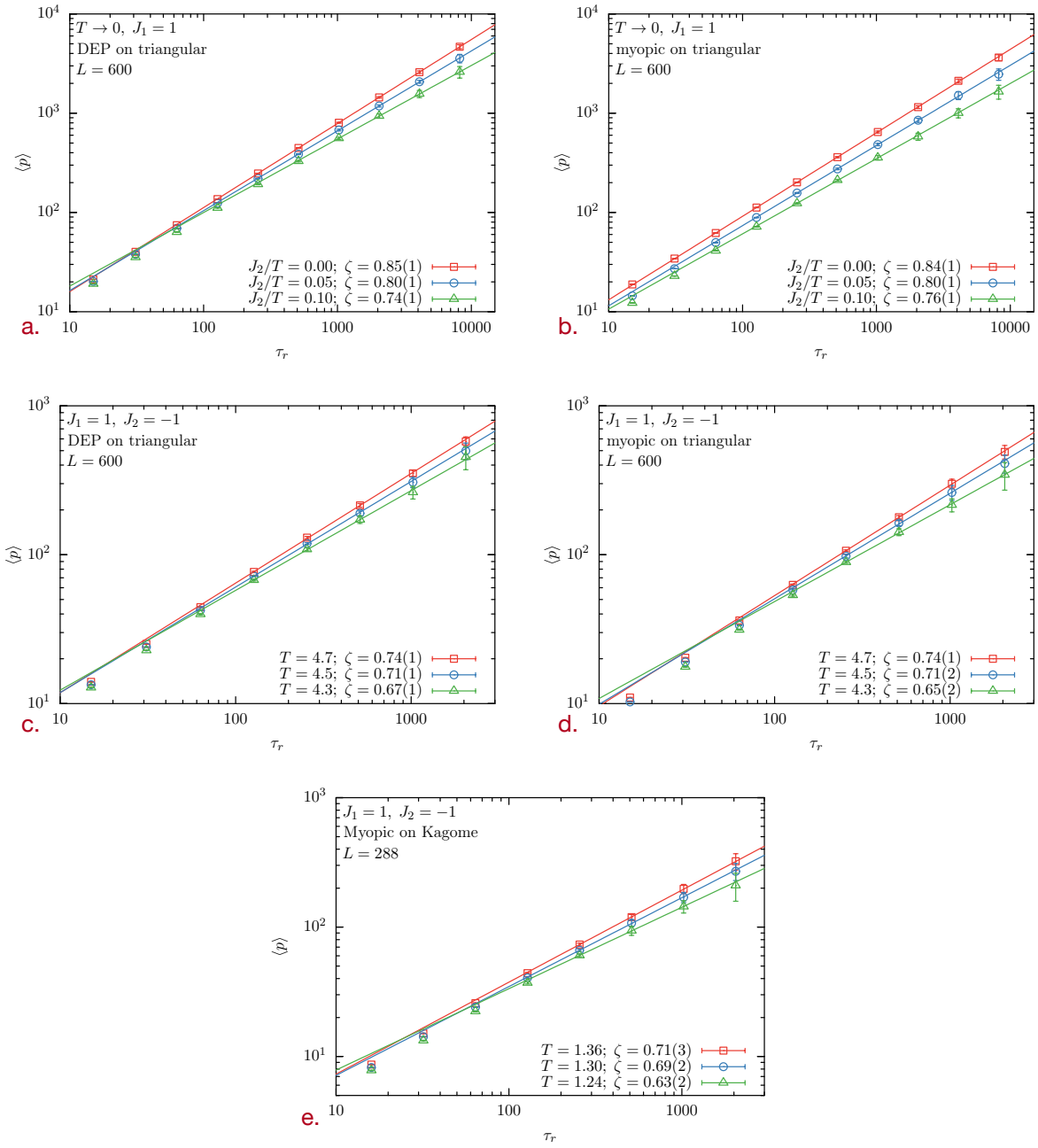

Figure 2.16: Average number of dual links $\langle p \rangle$ flipped by worms of length τ_r for the myopic algorithm in a 288×288 Kagome lattice for three values of T at which the system is in the power-law ordered critical phase. Lines denote fits to a power-law form $\propto {\tau_r}^{\zeta}$.

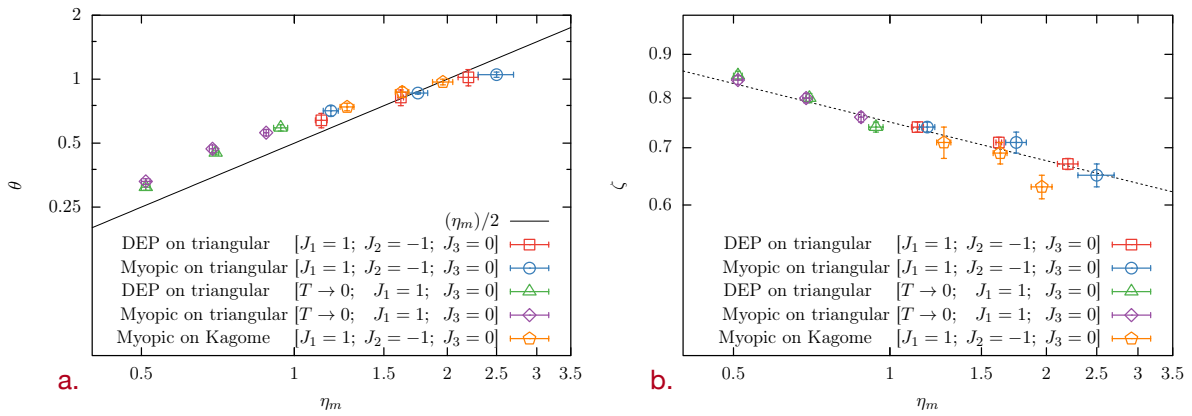

Figure 2.17: ζ extracted from the τ_r dependence of the average number of flipped dual links $\langle p \rangle$, plotted as a function η_m for all cases studied here. The dotted-line is a guide to the eye, suggesting that ζ depends in a universal way on η_m, and the dependence may be a power law.

multiplicities, if a site is visited more than once) visited by the head of the worm during the worm construction defines the length of the worm, which corresponds in our random walk analogy, to the return time of the walk. Histogramming this at the end of each worm construction gives us the return time probability distribution, $P(\tau_r)$ of the worms. From Eq.(2.23), we see that our simple random walk model would predict $P(\tau_r) \sim 1/\tau_r^{1+\theta}$, with $\theta = \eta_m/2 = 1/8\eta_s$.

Average worm length: We also measure the average length of a worm, $\langle v \rangle$. As noted earlier, our defect-antidefect correlator is normalized to ensure that $\langle v \rangle = \sum_{\vec{r}} C_m(\vec{r})$. Thus we expect $\langle v \rangle \sim L^{2-\eta_m}$. Interestingly, $\langle v \rangle$ can also be obtained from the return time probability distribution $P(\tau_r)$ as $\langle v \rangle = \sum_{\tau_r} \tau_r P(\tau_r)$. If we assume that the dominant contribution to this sum comes from the regime where $P(\tau_r) \sim 1/\tau_r^{1+\theta}$, and introduce an upper cutoff $\tau_{\text{cut-off}}(L)$ beyond which which $P(\tau_r)$ contributes sub-leading terms to the sum, then the L dependence of $\langle v \rangle$ should be controlled by the L dependence of the cutoff $\tau_{\text{cut-off}}$. If we assume $\tau_{\text{cut-off}}(L) \sim L^b$, then $\langle v \rangle \sim L^{b(1-\theta)}$. Comparing the two results for the form of $\langle v \rangle$ we obtain $b(1-\theta) = 2 - \eta_m$. Thus, our simple random walk model prediction of $\theta = \eta_m/2$ (Eq.(1.44)) corresponds to $b = 2$.

Average number of flipped links per worm: When a worm retraces its path, it flips the dimers along the retraced path again, in effect not flipping them in the first place. Thus counting the number of flipped links is equivalent to measuring the perimeter of the closed path defined by the worm. We measure the average number of flipped links per worm $\langle p \rangle$ as a function of the return time τ_r of the worm.

Average number of flipped spins per worm: After mapping back to the original spin configuration, we can measure the average number of spins on the direct lattice flipped by one worm update. This is equivalent to measuring the area enclosed by the closed worm. Since the worm is on a torus, this area can be the either be the inner or

outer area with respect to the worm. We choose to always work with the smaller area, and the corresponding number of flipped spins. In our measurements, we keep track of the average number of flipped spins $\langle a \rangle$ defined in this way, and study its dependence on the average number of flipped links $\langle p \rangle$ introduced earlier.

2.5 Results

All our measurements are performed on lattice sizes of upto 600×600 lattice sites for the triangular lattice antiferromagnet and upto 288×288 unit cells (with three sites per unit cell) for the Kagome lattice antiferromagnet. For studying the statistics of worms, we perform one worm update per Monte Carlo step (MCS) and measure all the requisite histograms and averages during the worm construction. If after the worm construction the dimer configuration is not physical, we discard the measurements made during that worm construction. All our data is averaged over 1×10^8 MCS.

We have performed such measurements in all five cases mentioned in Section. 2.2: In the $T \to 0$ limit on the triangular lattice, we study both the DEP and myopic algorithms at three values of $J_2/T = 0.00, 0.05$ and 0.10 all of which are in the power-law ordered phase. To access the $T > 0$ power-law ordered phase, we set $J_1 = 1$ and $J_2 = -1$. On the triangular lattice, we study both the algorithms in the power-law ordered phase at $T = 4.3, 4.5$ and 4.6, and on the Kagome lattice we study the myopic algorithm in the power-law ordered phase at $T = 1.24, 1.30$ and 1.36 (all temperatures are measured in units of $J_1 = 1$).

The defect-antidefect correlator $C_m(\hat{e_x}\frac{L}{s})$ is measured at separation $\hat{e_x}\frac{L}{s}$ (with $s = 2$ for the zero temperature measurements and $s = 24$ for the nonzero temperature measurements) on periodic $L \times L$ lattices as a function of lattice size L for $L = 288, 360, 420$ and 600 on the triangular lattice and $L = 96, 144, 216$ and 288 on the Kagome lattice ($\hat{e}_x$ is one of the Bravais lattice vectors). Fig. 2.1 show this correlator in the $T \to 0$ limit for the DEP and myopic worm algorithms respectively on the triangular lattice. Figs. 2.1 shows this correlator in the $T > 0$ regime for the DEP and myopic worm algorithms respectively on the triangular lattice. Fig. 2.1 shows the correlator in the $T > 0$ regime for the myopic worm algorithm on the Kagome lattice. In all the above cases we extract η_m by fitting a power law to the L dependence of the correlator. Fig. 2.2 plots the best-fit η_m obtained in this way versus the spin correlation exponent η_s (this exponent is measured by fitting the equilibrium spin correlator at the three sublattice wavevector to a power-law form) for each of these five cases. As can be seen, the data agrees very well with the theoretical prediction of $\eta_m = 1/4\eta_s$ for the $T \to 0$ case. We note that for $T > 0$ cases, the agreement is less impressive but still reasonable.

We measured the probability distribution of return times $P(\tau_r)$ as a function of τ_r for

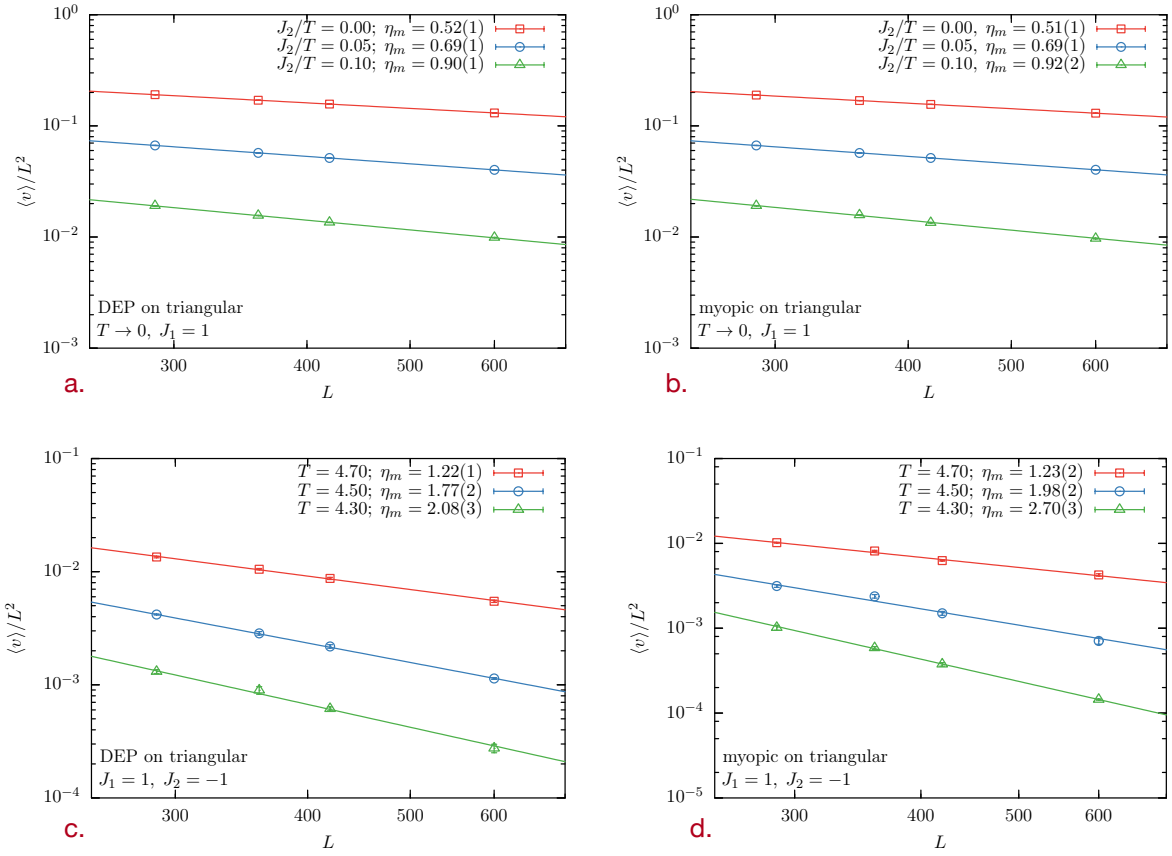

Figure 2.18: The lattice size L dependence of the average number of dual lattice sites visited per worm $\langle v \rangle$ using the myopic worm algorithm on the triangular lattice for three values of T at which the system is in the power-law ordered critical phase. Since $\langle v \rangle / L^2 \sim 1/L^{\eta_m}$, the power-law fits give us an alternate measurement of η_m.

$L = 600$ on the triangular lattice and $L = 288$ on the Kagome lattice. Figs. 2.14, 2.14 show the return time distribution in the $T \to 0$ limit for the DEP and myopic worm algorithms respectively on the triangular lattice. Figs. 2.14, 2.14 show the distribution in the $T > 0$ power-law ordered phase for the DEP and myopic worm algorithms respectively on the triangular lattice. Fig. 2.14 shows the distribution in the $T > 0$ power-law ordered phase for the myopic worm algorithm on the Kagome lattice. In all the above cases we extract θ by fitting power laws with exponent $1 + \theta$ to the tail of the distribution. Fig. **??** shows the measured value of θ as a function of $\eta_m^{\text{predicted}}/2 = 1/(8\eta_s)$ for the $T \to 0$ and the $T > 0$ cases respectively. The theoretical prediction of $\theta = \eta_m^{\text{predicted}}/2$ is seen to give a reasonable account of the measured values of θ in the $T > 0$ cases, although deviations are clearly visible. In the $T \to 0$ cases, we note that the prediction of our simple random walk model appears to deviate more significantly from the measured value of θ.

By way of comparison with a better-understood example, we also studied the return time distribution of a direct lattice worm algorithm for the fully-packed dimer model [84], on the 3-dimensional cubic lattice. In this case too, the worm creates a monomer-antimonomer pair, and propagates the antimonomer through the lattice until it recombines with the monomer at the starting site. The defect-antidefect correlator on the cubic lattice is controlled by the emergent Coulomb interaction between the monomer and antimonomer. Since this is a power-law potential rather than a logarithmic potential, the effective dimension d' in this case is $d' = d = 3$, and the return time statistics is therefore expected to be identical to that of the usual random walk in three dimensions [108]. Fig. 2.14 shows our measurement $\theta = 0.48 \pm 0.03$ of the persistence exponent, which agrees within errors with the exact value of $1/2$ predicted by Eq. 2.24 for $d' = 3$. This value of θ is also consistent with the results for the worm length distributions in Ref. [94], for a worm algorithm on the pyrochlore lattice.

We also measured the average number of flipped dual links per worm, $\langle p \rangle$, as a function of τ_r for $L = 600$ on the triangular lattice and $L = 288$ on the Kagome lattice. Figs. 2.16 shows this functional dependence in the $T \to 0$ power-law ordered phase for the DEP and myopic worm algorithms respectively on the triangular lattice. Figs. 2.16 shows this function in the $T > 0$ power-law ordered phase for the DEP and myopic worm algorithms respectively on the triangular lattice. Figs. 2.16 shows this functional dependence in the $T > 0$ power-law ordered phase for the myopic worm algorithm on the Kagome lattice. In all the above cases we find that $\langle p \rangle$ is a power of τ_r. The exponent ζ is obtained by fitting to a power-law form. Fig. 2.17 shows the value of ζ thus obtained, plotted as a function of η_m for each of these five cases. Though we do not have a theoretical prediction for this dependence, we note all the measured data points seem to fall on a single curve, suggesting a universal origin for this dependence.

We also measured the average number of flipped spins per worm on the direct lattice

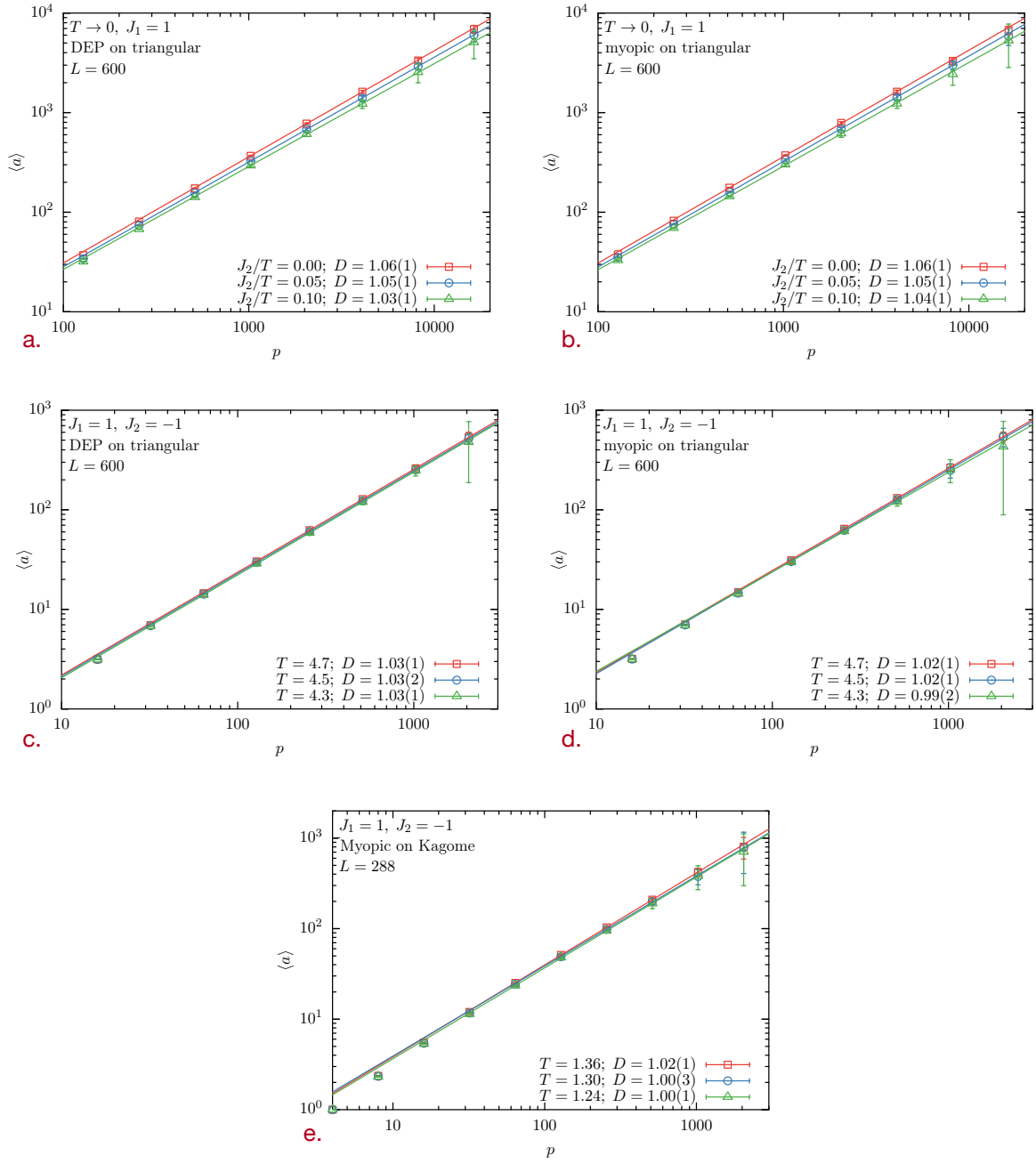

Figure 2.19: Average number of spins $\langle a \rangle$ flipped by worms that flip p dual links for the myopic algorithm in a 288×288 Kagome lattice for three values of T at which the system is in the power-law ordered critical phase. Lines denote fits to a power-law form $\propto p^D$.

$\langle a \rangle$ as a function of p, the number of flipped dual links, for $L = 600$ on the triangular lattice and $L = 288$ on the Kagome lattice. Figs. 2.19 shows the distribution in the $T \to 0$ limit for the DEP and myopic worm algorithms respectively on the triangular lattice. Figs. 2.19 shows the distribution in the $T > 0$ case for the DEP and myopic worm algorithms respectively on the triangular lattice. Figs. 2.19 shows the distribution in the $T > 0$ case for the myopic worm algorithm on the Kagome lattice. In all the above cases we extract the exponent D by fitting this functional dependence to a power law form. For worms that do not intersect themselves before closing, this would amount to plotting the enclosed area as a function of perimeter of the worm, and the exponent D could then be interpreted as the fractal dimension of the cluster constructed by the worm. However, when we perform the fits, we find that the fractal dimension $D \approx 1$ in all the five cases studied. To understand this better, we looked at the actual traces of the worms in all cases and found that the worms defined by these algorithms intersect themselves very often. The spin cluster obtained from such a worm consists of many small components and the area of the individual components does not scale with the measured total perimeter. For such worms, it is quite natural that the total perimeter and the area scale in the same way, *i.e.* $D \approx 1$.

We can also extract η_m from the lattice size L dependence of the average number of dual sites visited per worm $\langle v \rangle$ (as discussed in Section. 2.4) using the relation $\langle v \rangle / L^2 \sim 1/L^{\eta_m}$. Figs. 2.18 shows the power-law fits in the $T \to 0$ limit for the DEP and myopic worm algorithms respectively on the triangular lattice. Figs. 2.18 shows the power-law fits in the $T > 0$ regime for the DEP and myopic worm algorithms respectively on the triangular lattice. The extracted value of η_m matches within error-bars to the value of η_m extracted from the defect-antidefect correlator as seen in Figs. 2.1 for $T \to 0$ and $T > 0$ respectively. In the noninteracting dimer model limit of the dual dimer model ($T \to 0$ and $J_2/T = 0$), it is well known that $\eta_m = \frac{1}{2}$ and we find that our measurement of $\langle v \rangle / L^2 \sim 1/L^{0.52(2)}$ is in very good agreement. However we note that a previous study of a worm algorithm for the square ice model in the free dimer limit [110] concluded that $\langle v \rangle$ is $\langle v \rangle \sim L^{1.665(2)}$, which is at odds with what one would expect when $\eta_m = 1/2$ (the values of η_m and η_d are the same for the noninteracting dimer model on the honeycomb and the square lattice).

2.6 Conclusions

A similar heuristic picture for the worm-length distribution is possible in other applications of worm algorithms to two-dimensional critical points/phases, and it would be interesting to ask how well the analogs of Eq.(1.44) do in these cases. In the opposite direction, the readily discernible deviations of the measured values of θ from the pre-

diction of the simple random walk model underscore the importance of incorporating the back-reaction of worm motion on the underlying dimer configuration, rather than thinking in terms of a fixed static potential provided by the dimer configuration. We leave this as an interesting direction for future work.

Chapter 3

Triangular lattice Ising antiferromagnet with nearest and next-nearest neighbor couplings

3.1 Introduction

The Ising antiferromagnet on the triangular lattice [17], is a prototypical example of a frustrated magnet characterized by a macroscopic degeneracy of minimum energy spin configurations that give rise to a nonzero entropy density in the low temperature limit at $B = 0$ [17]. The geometry of the triangular lattice leads to competing nearest neighbor exchange interactions resulting in geometric frustration. One manifestation of this geometric frustration and the resulting degeneracy is that the system does not develop any long-range order all the way down to $T = 0$ [17]. Instead, the $T \to 0$ limit is characterized by power-law correlations of the Ising spins at the three-sublattice wavevector Q [43]. This provides a simple example of a classical spin-liquid. Experimental interest in geometric frustration has been long standing. Many transition-metal oxides crystallize in geometrically frustrated lattices based on triangles or tetrahedrons that share corners, edges or faces [24]. Examples include anhydrous alums[25, 26], jarosites[27, 28], Herbertsmithite[29], Kapellasite[30], pyrochlores[31, 32], spinels[33, 34], magnetoplumbites[35, 36], garnets[36], ordered NaCl[37, 38], and many other structure types[24]. A system based on non-colloidal monolayers has also been shown to approximate the triangular lattice Ising antiferromagnet in many ways[39]. Recently, a new class of rare-earth-based frustrated antiferromagnets have been discovered with effective Ising spins arranged on a perfect triangular lattice[40]. Given the abundance of geometric frustration in nature, many other types of geometrically frustrated models which exhibit spin-liquid behavior have also been analytically and numerically studied in search for a spin-liquid. Few examples include

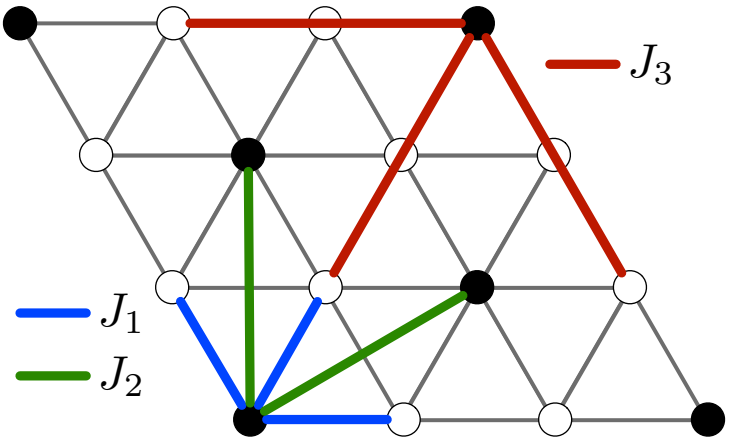

Figure 3.1: A 4×4 triangular lattice with nearest neighbor interaction: J_1 (shown in red), next-nearest neighbor interaction: J_2 (shown in green) and next-next-nearest neighbor interaction: J_3 (shown in blue). The filled circles represent up (down) spins and the empty circles represent down (up) spins. A ferromagnetic J_2 stabilizes "ferrimagnetic three-sublattice order with a net magnetic moment in which spins of one of the three sublattices of the triangular lattice point upward (downward) and the spins on the other two sublattices point downward (upward).

spin-ice[18, 19], pyrochlores[20], Kagome lattice models[21, 22] and Kagome ice[23].

The $T \to 0$ spin-liquid ground state of the triangular Ising antiferromagnet can be destabilized into seven distinct ordered ground states by introducing sub-leading next-nearest and next-next-nearest neighbor exchange couplings [42]. Ferromagnetic next-nearest neighbor couplings, stabilize long-range ferrimagnetic three-sublattice order below a critical temperature [47]. The three-sublattice ordered phase has a net magnetic moment and it distinguishes between the three sublattices of the triangular lattice with all spins on two sub-lattices pointing in one direction and the spins on the third sub-lattice pointing in the opposite direction. Very similar behavior is also seen in the Ising antiferromagnet on the Kagome lattice [22]. In the Kagome case, the $T = 0$ limit is a classical spin-liquid with short-ranged correlations, and next-nearest-neighbor couplings again induce long-range three-sublattice order below a critical temperature. The three-sublattice order in this case distinguishes between the three sublattices of the underlying triangular Bravais lattice structure.

Triangular Ising antiferromagnet with sub-leading ferromagnetic next-next nearest neighbor coupling has been used to model the monolayer adsorption of inert gases on graphite substrates [45]. The potential on the graphite surface has hexagonal symmetry and the adsorbed gas molecules tend to sit on the hexagonal centers forming a triangular net. Owing to the large effective size of the gas molecules, the nearest site occupation is unfavorable. By assigning an 'up' spin to the occupied sites and a 'down' spin to vacant sites, this model can be mapped to a triangular lattice Ising antiferromagnet.

The three-sublattice ordered state is known to melt in a two-step manner, with an intermediate-temperature phase characterized by power-law three-sublattice order of the Ising spins σ: $\langle\sigma(\vec{R})\sigma(0)\rangle \sim cos(\mathrm{Q}.\vec{R})/|\vec{R}|^{\eta(T)}$ with the temperature dependent power-law exponent $\eta(T) \in (1/9, 1/4)$ [47, 103].

Ferromagnetic next-next-nearest neighbor couplings J_3 also destabilize the spin-liquid phase preferred by the antiferromagnetic nearest-neighbor interactions at low temperatures by facilitating a so-called stripe ordered phase which has been shown to melt via a first order transition at a finite temperature[49]. The stripe ordered phase consists of alternating single ferromagnetic columns or rows of oppositely oriented spins. In a system with competing ferromagnetic next-nearest and next-next-nearest neighbor interactions, the three-sublattice ordered phase is known to undergo a first order transition into the striped phase when the next-next-nearest neighbor interactions dominate [49].

In this work we investigate the anti-ferromagnetic Ising model on a triangular lattice with competing ferromagnetic next-nearest and next-next-nearest neighbor interactions (henceforth referred to as the triangular lattice model) using sophisticated but efficient Monte-Carlo worm algorithms developed in Ref. [49]. We find similarities in the phase diagram that we numerically obtain for the triangular lattice model with the six-state clock model studied by Cardy [96]. We then numerically characterize the phase diagram of the six-state clock model using a Monte-Carlo Wolff cluster algorithm and compare it to the phase diagram of the triangular lattice model using a host of numerical techniques. This similarity in the phase diagram of the triangular lattice model and the six-state clock model is not accidental. The six-state clock model supports a six-fold symmetric ground state which can be mapped to the six-fold symmetric ground state that we see in the triangular lattice model. The six-fold symmetric ground state of the six-state clock model has a two-step melting transition with an intermediate power-law ordered phase[96] which pinches off via a multicritical point into a first-order line[97]. A self-dual line whose equation is known passes through this multicritical point[96, 97, 98]. Simulating parameter values and comparing the extracted critical exponents along this self-dual line allows us to numerically characterize this multicritical point and its neighborhood. On comparing the scaling behavior of various quantities in this neighborhood with that of the neighborhood of a similar multicritical point in the triangular lattice model allows us to numerically pin-point the location of the multicritical point in the phase diagram of the triangular lattice model.

We numerically verify a conjecture on the six-state clock model and obtain new results on both the six-state clock model and the triangular lattice model which we summarize below:

$a.$ On the six-state clock model, we present conclusive numerical evidence (by way of numerically obtaining multicritical exponents) of the conjecture that the multicritical

point at which the two-step melting phase pinches off belongs to the universality class of a Z_6 parafermionic CFT.
$b.$ On the six-state clock model, we numerically show that the line of first-order transitions which was previously conjectured to extend upto the multicritical point [97] becomes weakly first-order before meeting the multicritical point.
$c.$ We numerically obtain a phase diagram of the triangular lattice anti-ferromagnet with competing next-nearest and next-next-nearest neighbor interactions.
$d.$ We numerically show that there exists a multicritical point in the triangular lattice anti-ferromagnet with competing next-nearest and next-next-nearest neighbor interactions that belongs to the universality class of a Z_6 parafermionic CFT. To this end, we numerically extract multicritical exponents which match (within error-bars) the values predicted by the Z_6 parafermionic CFT.

The rest of the chapter is broadly organized as follows: In Section. 3.2 we discuss the various numerical techniques that we use to characterize the phase diagram in both the models. In Section 3.3, we define and numerically study the six-state clock model. In Section 3.4, we do the same for the antiferromagnetic Ising model on the triangular lattice with competing next-nearest and next-next-nearest neighbor ferromagnetic interactions. We conclude in Section. 3.5 with a summary of our conclusions and discuss future directions.

3.2 Methods

To distinguish between and numerically characterize the ordered, disordered and critical phases and the various phase transitions that we encounter in both our models, we use the disconnected two-point correlation function (henceforth referred to as the correlation function). The correlation function for a local order-parameter $\mathcal{O}(r)$ is defined as:

$$C_{\mathcal{O}}(r) = \langle \mathcal{O}(r+a) \cdot \mathcal{O}^*(a) \rangle \tag{3.1}$$

averaged over all sites a, where r is the distance between the two sites at a and $r+a$.

For $T < T_c$, when there is long-range order in $\mathcal{O}$, $C_{\mathcal{O}}(r) \to |A|^2$ as $r \to \infty$ where $A = \langle \mathcal{O} \rangle$ is the value of the order-parameter in the ordered phase. At the critical point at $T = T_c$, $C_{\mathcal{O}}(r) \sim 1/r^{\eta_{\mathcal{O}}}$, where $\eta_{\mathcal{O}}$ is a critical exponent. In case of a two-step melting transition with a critical phase between T_1 and T_2, the upper and lower critical transition temperatures of the two-step melt respectively, $\eta_{\mathcal{O}}$ becomes a temperature dependent critical exponent, $\eta_{\mathcal{O}}(T) \forall T \in [T_1, T_2]$. In the disordered phase at $T > T_c$, $C_{\mathcal{O}}(r) \sim \exp(-r/\xi)$ where ξ is a small finite correlation length. In our simulations we look at the averaged correlation function at a fixed distance L/a along the natural $\hat{x}$ and $\hat{y}$ axes of our lattice, where a is a proper divisor of the system size L. $C_{\mathcal{O}}(L/a)$

then has the same functional dependence on system size L for the various phases as described above, although in practice due to our finite-size lattice we may not see the exponential decay in the disordered phase. Since ξ diverges as $T \to T_c$, for T slightly greater than T_c even though the system is in a disordered phase, $\xi > L/a$. So any decay of the correlation function faster than $1/L^d$ where $d = 2$ is the dimension of the lattice is considered to be an indication of the system being disordered.

We also look at the fourth-order binder cumulant to study the phase transitions. The binder-cumulant for a n-component order-parameter $\mathcal{O}$ is defined as:

$$U_{\mathcal{O}}(L) = 1 - \frac{n\langle \mathcal{O}(L)^4 \rangle}{(n+2)\langle \mathcal{O}(L)^2 \rangle^2} \tag{3.2}$$

As $L \to \infty$, to leading order, $U_{\mathcal{O}}(L) \sim 0$ in the disordered limit and $U_{\mathcal{O}}(L) \sim 2/(n+2)$ in the ordered limit. In case of a continuous phase transition $U_{\mathcal{O}}(L)$ as a function of decreasing temperature T is a monotonically increasing function bounded between $[0, 2/(n+2)]$ with an inflection point approaching $(U^*_{\mathcal{O}}, T_c)$ as $L \to \infty$ where $U^*_{\mathcal{O}}$ is a L-independent universal value $\ni 0 < U^*_{\mathcal{O}} < 2/(n+2)$. Since at criticality, $U_{\mathcal{O}}(L)$ approaches $U^*_{\mathcal{O}}$, the *crossing* point of various $U_{\mathcal{O}}(L)$ can be used to determine T_c. At $L = \infty$, $U_{\mathcal{O}}(L)$ becomes a step-function which jumps from 0 to $2/(n+2)$ at T_c as we decrease T. In practice for finite size systems although $U^*_{\mathcal{O}}$ has leading order L-dependent corrections, in our simulations we find them to be small enough to be ignored. Our error-bars accommodate any finite-size effects on $U^*_{\mathcal{O}}$. In a two-step melting scenario, $U_{\mathcal{O}}(L)$ is still monotonically increasing as a function of decreasing T bounded by $[0, 2/(n+2)]$. However, since we have a critical phase between T_2 and T_1, the upper and lower critical temperatures of the two-step melt respectively, $U_{\mathcal{O}}(L) \to U^*_{\mathcal{O}}(T)$, a $L-$independent but $T-$dependent universal value between T_1 and T_2 in the $L \to 0$ limit. Hence $U_{\mathcal{O}}(L)$ for various L *stick* throughout the critical region between T_2 and T_1. First order transitions cause $U_{\mathcal{O}}(L)$ to become non-monotonic and no longer be bounded between $[0, 1/a]$. Negative peaks develop in $U_{\mathcal{O}}(L)$ for large system sizes between the $T \to T_c$ fixed point and the $T \to \infty$ fixed point with peak heights diverging with increasing L as L^2 and peak position approaching T_c as $L \to \infty$. The emergence of the negative peaks has been attributed to the presence of multiple peaks (phase co-existence) in the order-parameter distribution which occurs in the vicinity of a first-order transition[111]. In the vicinity of a weak first-order transition, phase-coexistence still occurs leading to negative peaks in $U_{\mathcal{O}}(L)$, but the peak heights diverge with increasing L as L^b, where $b < 2$. This feature can hence be used to differentiate between a first-order and a weak first-order transition.

We also look at correlation ratios of the form $V_{\mathcal{O}}(L) = C_{\mathcal{O}}(L/a)/C_{\mathcal{O}}(L/a')$. For $a > a'$ it can be easily seen that the dimensionless ratio $V_{\mathcal{O}}(L) \to 0$ in the disordered phase and $V_{\mathcal{O}}(L) \to 1$ in the ordered phase for $L \to \infty$. At a critical point, from finite-size

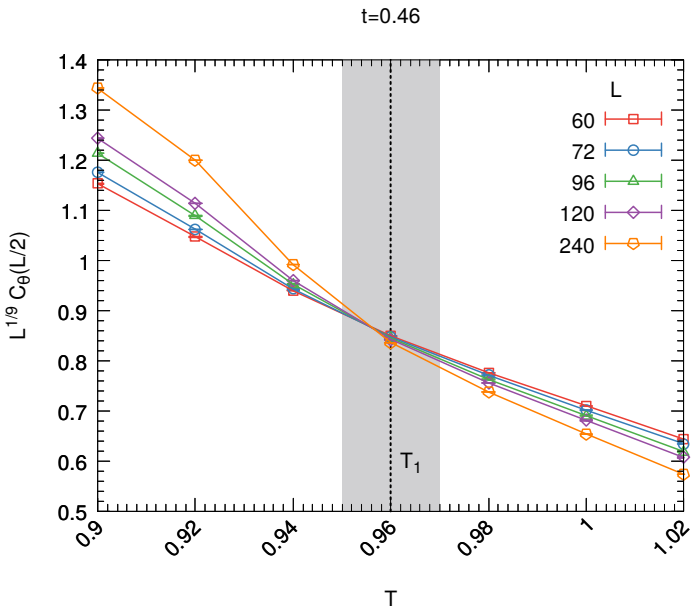

Figure 3.2: The two-point correlation function of the three-sublattice order parameter $\cos(\theta)$, $C_\theta(\vec{r})$ at separation $\vec{r} = \hat{e}_x \frac{L}{2}$ rescaled by a factor $L^{1/9}$, as a function of temperature T for various system sizes L at $t = 0.46$. At $T_1 = 0.96(1)$, we see a crossing for the various system sizes. Lines are cubic splines and a guide for the eye.

arguments, $V_{\mathcal{O}}(L)$ becomes scale invariant causing this quantity to *cross* for various L at a critical, $L-$independent value $V^*_{\mathcal{O}} \ni 0 < V^*_{\mathcal{O}} < 1$. In case of a two-step melting transition with a critical phase between T_1 and T_2, the upper and lower critical transitions of the two-step melting respectively, $V_{\mathcal{O}}(L)$ will *stick* through out the critical phase for various L, defining a $L-$independent but $T-$dependent critical value $V_{\mathcal{O}}(T)^*$.

A simple histogram of the order-parameter distribution $P(|\mathcal{O}|)$ also gives great insight into the nature of the phase transition. $P(|\mathcal{O}|)$ is obtained during the Monte-Carlo run which samples configurations based on their weight in the partition function of the system and hence directly corresponds to the weight of the order-parameter $\mathcal{O}$ in the Landau free-energy of the effective Hamiltonian. Thus $P(|\mathcal{O}|)$ develops a peak at a non-zero value of $|\mathcal{O}|$ when the system is in the ordered phase and peaks at 0 when the system is in the disordered phase with respect to the order-parameter $\mathcal{O}$. In case of a continuous transition between the ordered and disordered phases, the peak position shifts smoothly from a non-zero value to 0 with increasing temperature. In case of a first-order order to disorder transition, at the transition temperature $P(|\mathcal{O}|)$ develops a two-peak structure with peaks at 0 and the ordered value of $|\mathcal{O}|$ corresponding to the phase coexistence at a first-order transition. In case of a weak first-order transition the distance between the two co-existence peaks is smaller than that of a first-order transition with decreasing distance corresponding to decreasing weakness of the first-order transition.

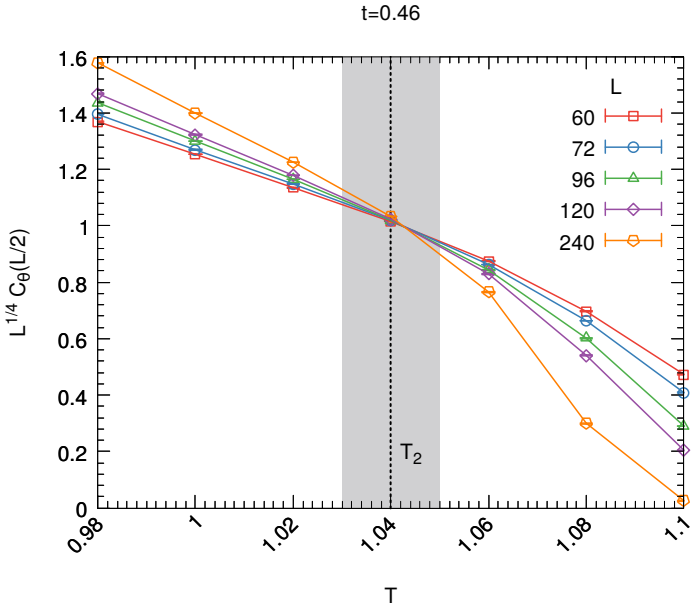

Figure 3.3: The two-point correlation function of the three-sublattice order parameter $\cos(\theta)$, $C_\theta(\vec{r})$ at separation $\vec{r} = \hat{e}_x \frac{L}{2}$ rescaled by a factor $L^{1/4}$, as a function of temperature T for various system sizes L at $t = 0.46$. At $T_2 = 1.04(1)$, we see a crossing for the various system sizes. Lines are cubic splines and a guide for the eye.

3.3 Six-state clock model

The Hamiltonian of the six-state clock model can be written as [96]:

$$H = \sum_{\langle ij \rangle} V(\theta_i - \theta_j). \tag{3.3}$$

where $\sum_{\langle ij \rangle}$ is the sum over nearest neighbor pairs of the lattice and θ_i, a multiple of $2\pi/6$ is an angular variable defined on each site of the lattice. The potential V is defined as:

$$V(\theta) = K_1[1 - cos(\theta)] + K_2[1 - cos(2\theta)] + K_3[1 - cos(3\theta)]. \tag{3.4}$$

where, $\theta \equiv \theta(r) = \theta_i - \theta_j$ and $r \equiv r_{ij}$ is the distance between sites i and j.

The ground state of the clock model is a six-fold symmetry phase which can be mapped to the ground state of the triangular lattice model. In the phase diagram of the six-state model, this ground state melts via various transitions depending on the values of K_1, K_2 and K_3, including a two-step melting scenario and a first order melting scenario which are separated by a multicritical point $\mathfrak{M}$[96, 112, 97]. To simplify our discussion we look at the phase diagram in a (t, T) plane where t is a line defined in the (K_1, K_2, K_3) space which is of interest to us. To this end, the six-state model can be

parameterized in terms of t, α and β along the lines of Ref. [97] as:

$$\begin{aligned} K_1 &= \frac{1}{3}\log\left(t/\left[(\beta-\alpha t)(\alpha-2\beta t)\right]\right); \\ K_2 &= \frac{1}{3}\log\left((\alpha-2\beta t)/\left[t(\beta-\alpha t)\right]\right); \\ K_3 &= \frac{1}{6}\log\left((\beta-\alpha t)^2/\left[(\alpha-2\beta t)t^2\right]\right); \end{aligned} \tag{3.5}$$

$\alpha = 3-\sqrt{6}$ and $\beta = \sqrt{6}-2$ defines a self-dual line, t, in the phase diagram of the model, which passes through a multicritical point at $t = t_{\mathfrak{M}}$[112]. For $t < t_{\mathfrak{M}}$ the six-fold symmetric ground state is separated from the disordered state by a first-order transition[97]. For $t > t_{\mathfrak{M}}$, the ground state melts via a two-step transition defined by a lower and upper critical transition temperatures T_1 and T_2 with a critical phase in between which pinches off at the multicritical point $\mathfrak{M}$[96, 112]. This critical phase is defined by a temperature dependent critical exponent, $\eta(T) \in [1/9, 1/4]$ for $T \in [T_1, T_2]$[105]. The self dual line passes through this critical phase. It was conjectured that the multicritical point at $t = t_{\mathfrak{M}}$ belongs to the universality class of the Z_6 self-dual parafermionic CFT given by Zamolodchikov and Fateev [98]. Naturally, it begs to be asked if this multicritical point is similar to the one we see at the intersection of a line of first order transitions and the pinch-off point of a two-step melting transition in the triangular lattice model as discussed in Section. 3.4. To this end, we first perform detailed simulations on the square lattice six-state clock model. Below we give details about our analysis of the six-state clock model. We perform simulations in the (t, T) parameter space for a fixed $\alpha = 3-\sqrt{6}$ and $\beta = \sqrt{6}-2$. The complex order-parameter $\exp(i\theta)$ captures the six states of the six-fold symmetric ground state. We also look at the order parameters $\exp(2i\theta)$ and $\exp(3i\theta)$. As we explain in Section. 3.4 these three order parameters find direct analogues in the triangular lattice model. The simulations for the six-state clock model were done on a square lattice with toric boundary conditions using a Wolff cluster algorithm [70] for upto 240×240 lattices. The respective correlations functions for the three order-parameters described above are labeled as $C_\theta(r)$,$C_{2\theta}(r)$ and $C_{3\theta}(r)$ respectively. We also look at the binder-cumulants for the 1-component order parameter $cos(\theta)$, $U_\theta(L)$ and the 2-component order parameter $cos(3\theta)$, $U_{3\theta}(L)$.

We first look at $t = 0.46 > t_{\mathfrak{M}}$ at which we show that the system melts via a two-step melting transition. At the lower critical transition temperature T_1 of the two-step melt, the two-point correlation function of the six-fold symmetric order parameter $\exp(i\theta)$, $C_\theta(r) \sim 1/r^{1/9}$. Hence, $C_\theta(L/2)$ rescaled by a factor $L^{1/9}$, plotted as a function of temperature T should become a $L-$independent quantity at T_1 and *cross* for various system sizes at $T = T_1$. Using a similar argument, $L^{1/4}C_\theta(L/2)$ plotted as a function of T, should cross for various L at $T = T_2$. Fig. 3.2 and 3.3 show a *crossing* in $L^{1/9}C_\theta(L/2)$ and $L^{1/4}C_\theta(L/2)$ as a function of T for various L at $T_1 = 0.96(1)$ and $T_2 = 1.04(1)$

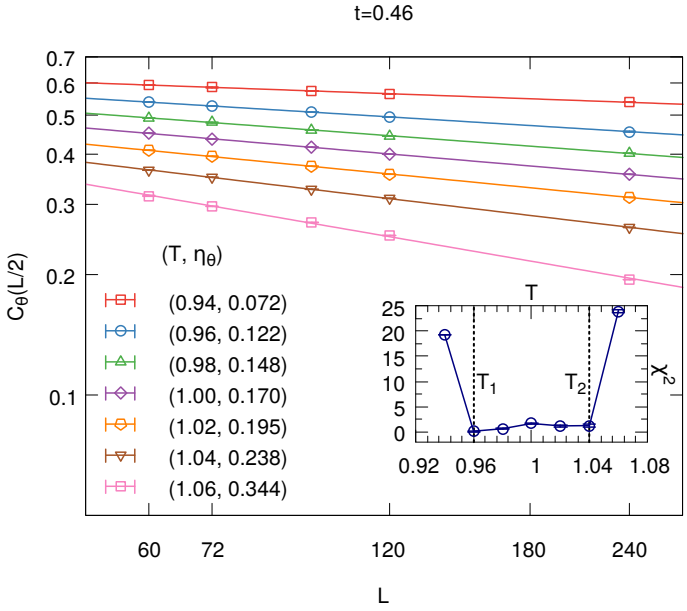

Figure 3.4: The two-point correlation function of the three-sublattice order parameter $\cos(\theta)$, $C_\theta(\vec{r})$ at separation $\vec{r} = \hat{e}_x \frac{L}{2}$ as a function of system size L, for various values of temperatures ($T \in [0.94, 1.06]$) at $t = 0.46$. The straight lines are power-law fits of $1/L^{\eta_\theta}$ to $C_\theta(L/2)$. Inset shows the χ^2 of the power-law fits of $1/L^{\eta_\theta}$ to $C_\theta(L/2)$ as a function of the temperature.

respectively. Fig. 3.4 shows $C_\theta(L/2)$ plotted as a function of system size L for various $T \in [0.94, 1.06]$. Lines are power-law fits to $1/L^{\eta_\theta}$. η_θ increases with increasing T with $\eta_\theta = 0.122 \sim 1/9$ at $T = T_1 = 0.96$ and $\eta_\theta = 0.238 \sim 1/4$ at $T = T_2 = 1.04$. Inset of Fig. 3.4 shows the χ^2 of the power-law fits of $C_\theta(L/2)$ to $1/L^{\eta_\theta}$ as a function of T. Since the two-step melting is bounded by the lower and upper critical transition temperatures, T_1 and T_2 respectively and the correlation function goes to zero as a power-law only in the critical phase between T_1 and T_2 and we see a clear minima in the χ^2 of the fits between $T_1 = 0.96$ and $T_2 = 1.04$ (indicated by dashed vertical lines) as expected. The width (in temperature) of the two-step melting phase at $t = 0.46$ is $\Delta T = 0.08$. As we further decrease t, in the limit $t \to t^+_{\mathfrak{M}}$, the two-step melting phase pinches off and the width of the two-step melting phase, $\Delta T \to 0$. But, in practice, due to the finite-size nature of our lattice simulations and finite Monte-Carlo time, ΔT can only be resolved if $\Delta T > \delta T_1$ or δT_2, the error-bar on T_1 and T_2 respectively. Thus, the pinch-off point overestimates the value of $t_{\mathfrak{M}}$.

At $t = 0.35$, we find the last resolvable ΔT our methods can afford. Fig. 3.5 and 3.6 show the plots of $L^{1/9} C_\theta(L/2)$ and $L^{1/4} C_\theta(L/2)$ respectively as a function of T for various L at $t = 0.35$. Both show a crossing allowing us to estimate the lower and upper critical transition temperatures $T_1 = 0.99970(25)$ and $T_2 = 1.00000(25)$ respectively, with a $\Delta T = 0.0003$. We hence need other more sensitive methods to estimate $t_{\mathfrak{M}}$,

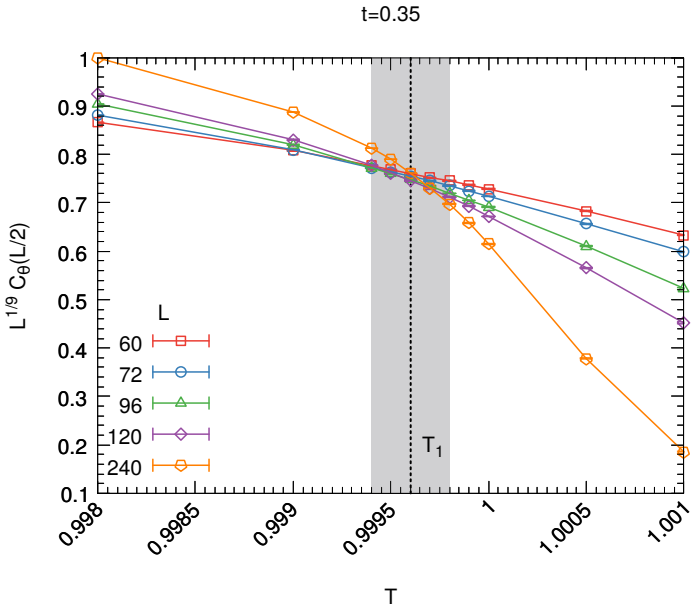

Figure 3.5: The two-point correlation function of the three-sublattice order parameter $\cos(\theta)$, $C_\theta(\vec{r})$ at separation $\vec{r} = \hat{e}_x \frac{L}{2}$ rescaled by a factor $L^{1/9}$, as a function of temperature T for various system sizes L at $t = 0.35$. At $T_1 = 0.9997(5)$, we see a crossing for the various system sizes. Lines are cubic splines and a guide for the eye.

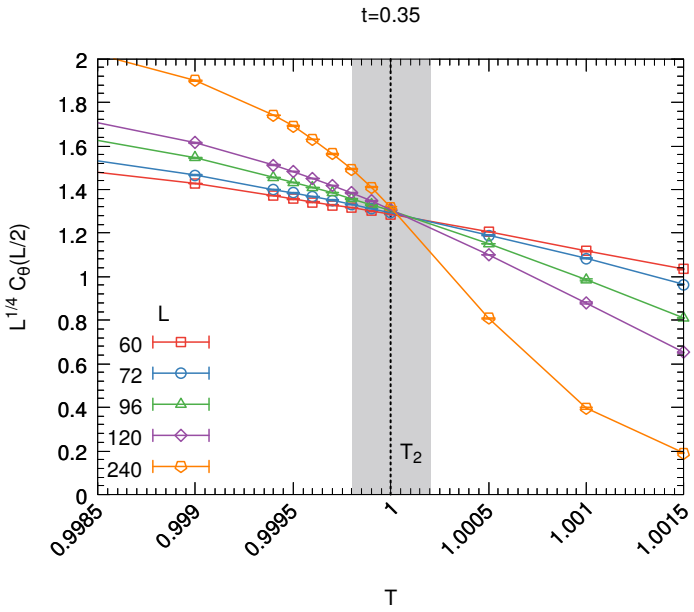

Figure 3.6: The two-point correlation function of the three-sublattice order parameter $\cos(\theta)$, $C_\theta(\vec{r})$ at separation $\vec{r} = \hat{e}_x \frac{L}{2}$ rescaled by a factor $L^{1/4}$, as a function of temperature T for various system sizes L at $t = 0.35$. At $T_2 = 1.0000(5)$, we see a crossing for the various system sizes. Lines are cubic splines and a guide for the eye.

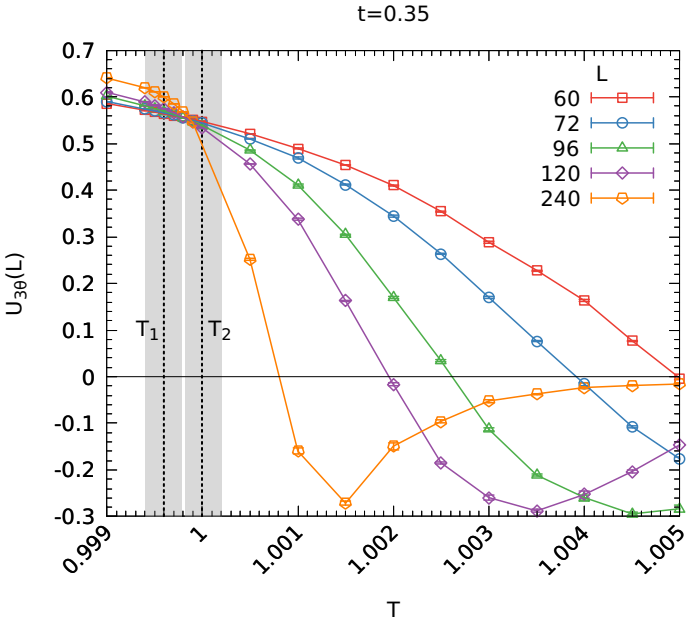

Figure 3.7: T dependence of the binder-cumulant of the order parameter $\cos(3\theta)$, $U_{3\theta}$ at $t = 0.35 > t_{\mathfrak{M}}$ for various L. The dashed vertical lines show T_1 and T_2.

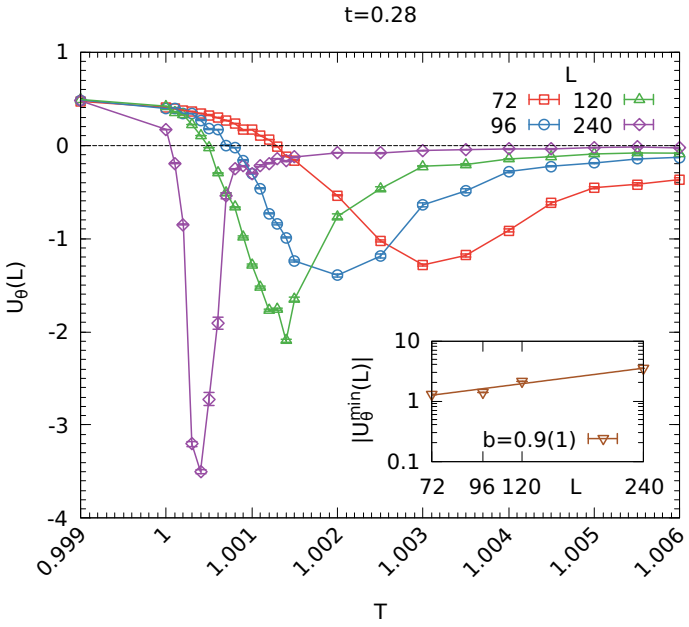

Figure 3.8: T dependence of the binder-cumulant of the three-sublattice order parameter $\cos(\theta)$, U_θ at $t = 0.28 < t_{\mathfrak{M}}$ for various system sizes L. Inset shows the power-law dependence of the magnitude of the peak-height on the system size L. The straight line (inset) is a power-law fit to L^b.

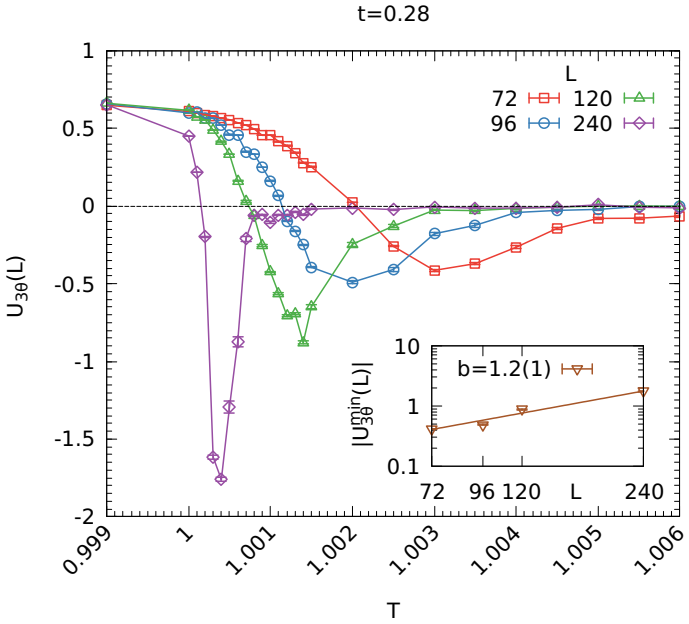

Figure 3.9: T dependence of the binder-cumulant of the order parameter $\cos(3\theta)$, $U_{3\theta}$ at $t = 0.28 < t_{\mathfrak{M}}$ for various system sizes L. Inset shows the power-law dependence of the magnitude of the peak-height on the system size L. The straight line (inset) is a power-law fit to L^b.

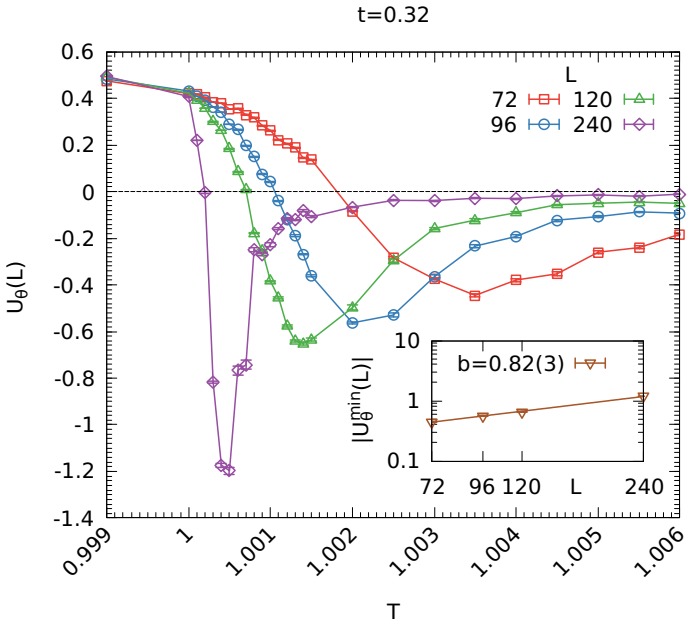

Figure 3.10: T dependence of the binder-cumulant of the three-sublattice order parameter $\cos(\theta)$, U_{θ} at $t = 0.32 < t_{\mathfrak{M}}$ for various system sizes L. Inset shows the power-law dependence of the magnitude of the peak-height on the system size L. The straight line (inset) is a power-law fit to L^b.

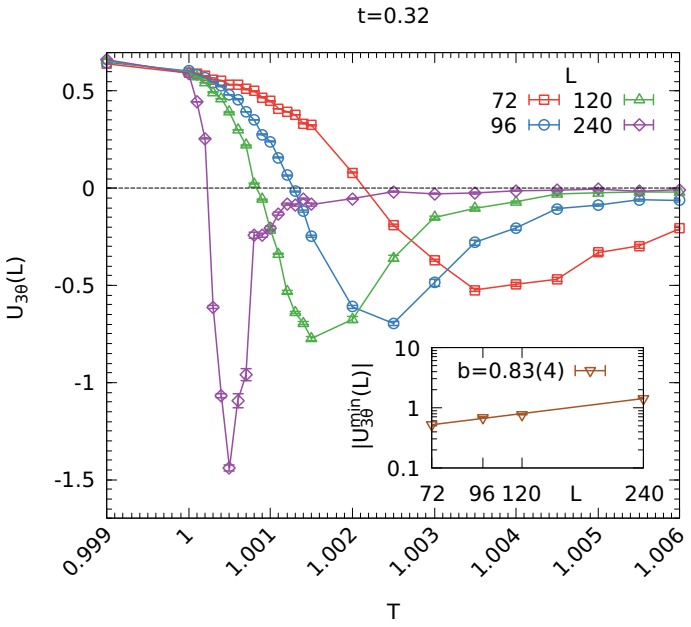

Figure 3.11: T dependence of the binder-cumulant of the order parameter $\cos(3\theta)$, $U_{3\theta}$ at $t = 0.32 < t_{\mathfrak{M}}$ for various system sizes L. Inset shows the power-law dependence of the magnitude of the peak-height on the system size L. The straight line (inset) is a power-law fit to L^b.

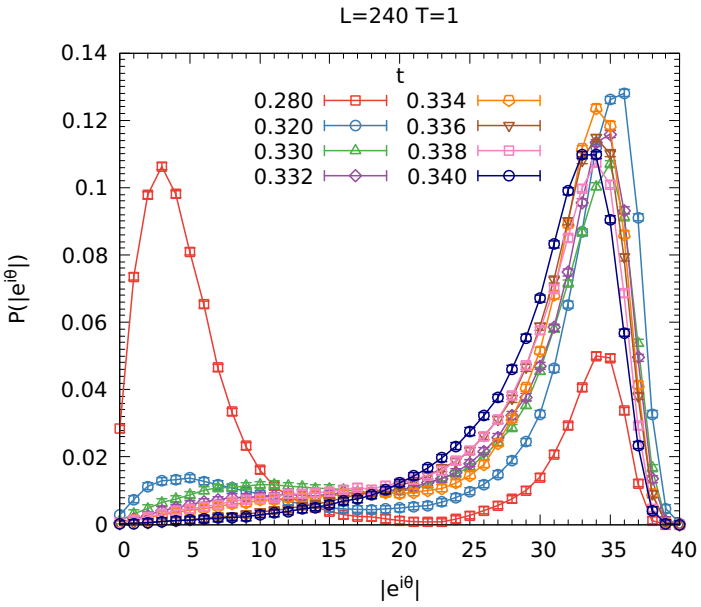

Figure 3.12: Histograms of the three-sublattice order parameter $|e^{i\theta}|$, $P(|e^{i\theta}|)$ at $T = 1$ and $L = 240$ for various values of $t < t_{\mathfrak{M}}$.

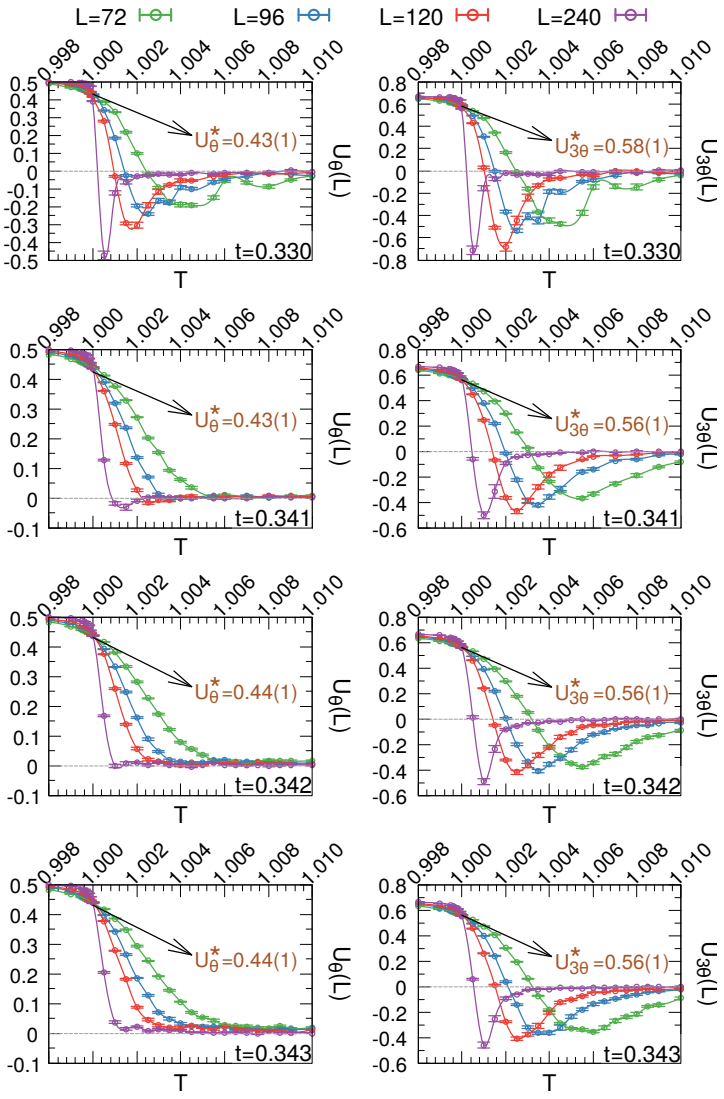

Figure 3.13: T dependence of the binder-cumulants, U_θ (left panel) and $U_{3\theta}$ (right panel) for various $t = 0.330, 0.341, 0.342$ and 0.343. Lines are cubic splines and a guide for the eye.

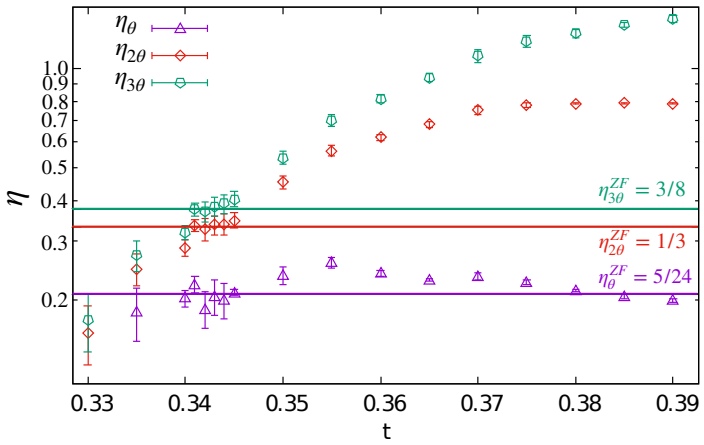

Figure 3.14: Values of η_θ, $\eta_{2\theta}$ and $\eta_{3\theta}$ measured at $T = 1$ of the six-state clock model as a function of t. The solid lines represent the value of η as predicted by the Z_6 self-dual parafermionic conformal field theory constructed by Zamolodchikov and Fateev[98].

which we describe shortly. Fig. 3.7 shows the binder-cumulant $U_{3\theta}(L)$ as a function of T at $t = 0.35$. In the two-step melting phase even though $U_{3\theta}(L)$ should be monotonic and bounded between [0,2/3], we see negative peaks in the binder-cumulant which do not scale with L. This is a an artifact of the proximity of the pinch-off point to a line of weak first-order transitions found at $t < t_{\mathfrak{M}}$. This anomalous behavior of the binder cumulants has been observed before for continuous transitions in the proximity of a weak first order line. As we will show below, $U_{3\theta}(L)$ shows this anomalous behavior for $t = t_{\mathfrak{M}} + \epsilon$, where ϵ is a small positive number, but $U_\theta(L)$ is well behaved (monotonic and bounded between $[0, 1/2]$) for $t > t_{\mathfrak{M}}$. This feature provides a key similarity with the triangular lattice model helping us pin-point the location of the multicritical point on the triangular lattice model.

We then look at $t = 0.28 < t_{\mathfrak{M}}$. Fig. 3.8 and 3.9 show $U_\theta(L)$ and $U_{3\theta}(L)$ respectively as a function of T for various system sizes. Both binder-cumulants show negative peaks which scale with the system size L with a *crossing* behavior at the transition temperature $T = 1$. Inset in Fig. 3.8 and 3.9 plots the height of the negative peaks as a function of system size L. Lines are fits to a power-law of the form L^b. $U^{\min}_\theta(L)$ scales as $L^{0.9}$ and $U^{\min}_{3\theta}(L)$ scales as $L^{1.2}$. As discussed in Section. 3.2, a scaling of the negative peaks in the binder-cumulant softer than L^2 indicates a weak-first order transition at $T = 1$ for $t = 0.28$. At $t = 0.32$, the system continues to exhibit a weak first-order transition at $T = 1$ as seen in the negative peaks of $U_\theta(L)$ and $U_{3\theta}(L)$ shown in Fig. 3.10 and 3.11 respectively. Inset of Fig. 3.10 and 3.11 show that $U^{\min}_\theta(L)$ scales as $L^{0.82}$ and $U^{\min}_{3\theta}(L)$ scales as $L^{0.83}$ at $t = 0.32$, showing the increasingly weak first-order behavior of the melting transition as $t \to t^-_{\mathfrak{M}}$.

As further confirmation of this weakening first-order behavior, we plot the histogram of the order-parameter $P(|exp(i\theta)|)$ as a function of $|exp(i\theta)|$ in Fig. 3.12 at the transi-

tion temperature $T = 1$ for various $t \in [0.28, 0.34] < t_{\mathfrak{M}}$. We see a clear double peak structure at $t = 0.28$. As we increase t, the distance between the two peaks decreases before finally becoming a single peak at $t = 0.34$. As discussed in Section. 3.2 this implies a weakening first-order transition as $t \to t_{\mathfrak{M}}^-$. To determine the extent of this weakening first-order behavior as $t \to t_{\mathfrak{M}}^-$ we look at the behavior of $U_\theta(L)$ and $U_{3\theta}(L)$ as a function of T for various $t \in [0.330, 0.343]$ in Fig. 3.13. The left and right panel show $U_\theta(L)$ and $U_{3\theta}(L)$ respectively. At $t = 0.33$, both $U_\theta(L)$ and $U_{3\theta}(L)$ show negative peaks due to the weak first-order nature of the transition at $t = 0.33$. As we increase t, the height of the negative peaks for both the binder-cumulants decreases and finally at $t = 0.342$, we see that $U_\theta(L)$ becomes monotonic and bounded between $[0, 1/2]$. $U_{3\theta}(L)$ continues to have negative peaks for $t > 0.342$ and well into the two-step melting region at $t = 0.35$ as seen in Fig. 3.7. To accurately determine $t_{\mathfrak{M}}$, we turn to the conjecture by Dorey et. al. that the multicritical point at $t = t_{\mathfrak{M}}$ belongs to the universality class of the Z_6 self-dual parafermionic CFT. This CFT predicts the critical exponents η as $\eta_\theta^{ZF} = 5/24$, $\eta_{2\theta}^{ZF} = 1/3$ and $\eta_{3\theta}^{ZF} = 3/8$ for the order parameters $\exp(i\theta)$, $\exp(i2\theta)$ and $\exp(i3\theta)$ respectively. Since the self-dual line defined by $T = 1$ passes through the multicritical point, we can measure the critical exponents η along this self-dual line and compare them with the values predicted by the CFT to determine $t_{\mathfrak{M}}$. Fig. 3.14 shows the values of η_θ, $\eta_{2\theta}$ and $\eta_{3\theta}$ which were measured by fitting power-laws of the form $1/L^\eta$ to $C_\theta(L/2)$, $C_{2\theta}(L/2)$ and $C_{3\theta}(L/2)$ respectively for various $t \in [0.33, 0.39]$ at $T = 1$. Solid lines show the values of η_θ^{ZF}, $\eta_{2\theta}^{ZF}$ and $\eta_{3\theta}^{ZF}$. At $t = t_{\mathfrak{M}} = 0.342(1)$ we find the best match with the values predicted by the CFT. As discussed above, $t = 0.342$ is the point at which $U_\theta(L)$ becomes monotonic while $U_{3\theta}(L)$ continues to remain non-monotonic for $t > 0.342$. Although we do not have a qualitative argument for why the weak-first order line at $t < t_{\mathfrak{M}}$ effects only $U_{3\theta}(L)$ for $t > t_{\mathfrak{M}}$, as shown in Sec.3.4, this is the same behavior we find in the triangular lattice model.

3.4 Ising antiferromagnet on the triangular lattice with next-nearest and next-next-nearest ferromagnetic interactions.

The Hamiltonian for our model of Ising spins on the triangular lattice can be written as:

$$H = J_1 \sum_{\langle rr' \rangle} \sigma_r \sigma_{r'} + J_2 \sum_{\langle\langle rr' \rangle\rangle} \sigma_r \sigma_{r'} + J_3 \sum_{\langle\langle\langle rr' \rangle\rangle\rangle} \sigma_r \sigma_{r'} \tag{3.6}$$

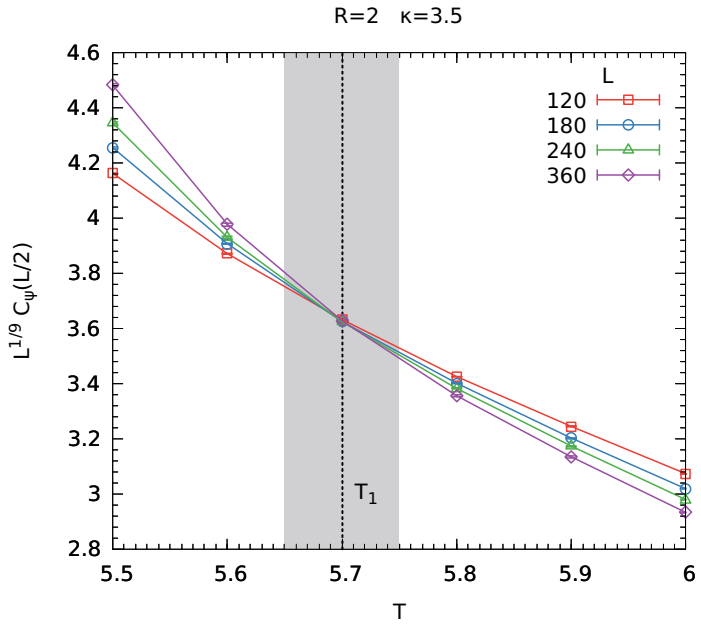

Figure 3.15: The two-point correlation function of the three-sublattice order parameter ψ, $C_\psi(\vec{r})$ at separation $\vec{r} = \hat{e}_x \frac{L}{2}$ rescaled by a factor $L^{1/9}$, as a function of temperature T for various system sizes L at $R = 2$ and $\kappa = 3.5$. At $T_1 = 5.7(1)$, we see a crossing for various system sizes. The error bar on T represents the width of the temperature grid in our simulations. Lines are cubic splines and a guide for the eye.

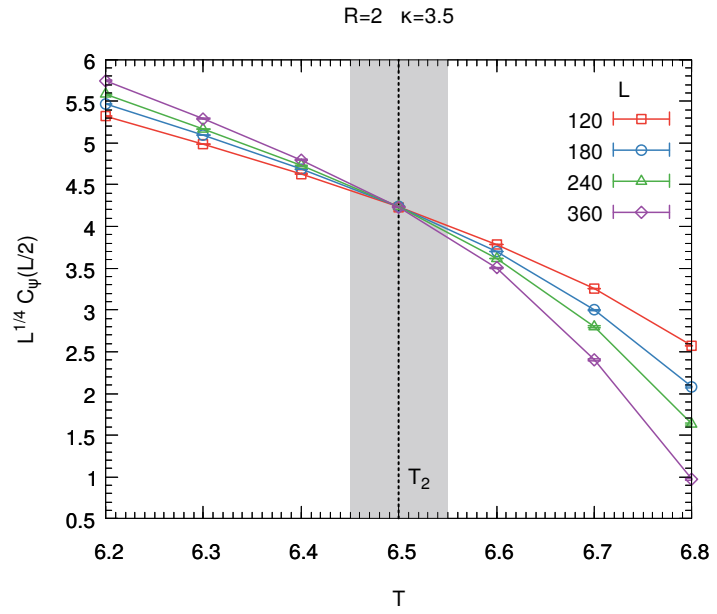

Figure 3.16: The two-point correlation function of the three-sublattice order parameter ψ, $C_\psi(\vec{r})$ at separation $\vec{r} = \hat{e}_x \frac{L}{2}$ rescaled by a factor $L^{1/4}$, as a function of temperature T for various system sizes L at $R = 2$ and $\kappa = 3.5$. At $T_2 = 6.5(1)$, we see a crossing for various system sizes. The error bar on T represents the width of the temperature grid in our simulations. Lines are cubic splines and a guide for the eye.

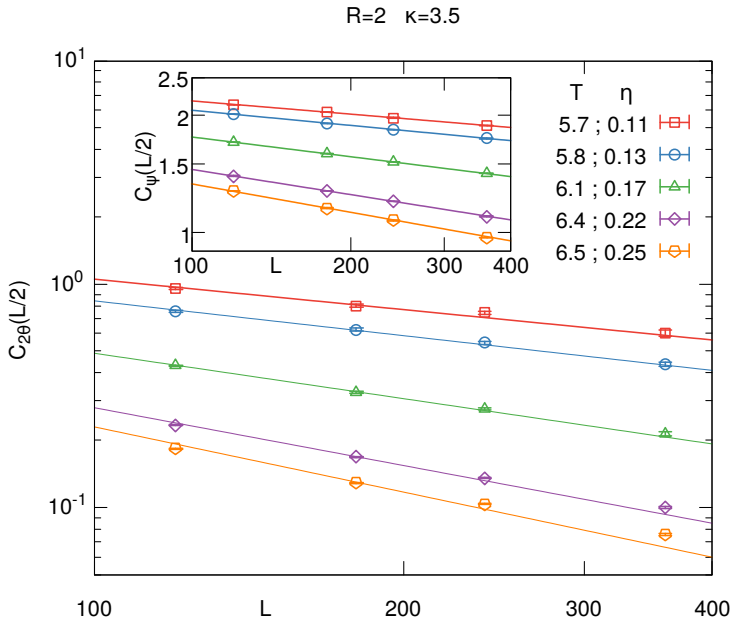

Figure 3.17: The two-point correlation function of $\cos(2\theta)$, $C_{2\theta}(\vec{r})$ at separation $\vec{r} = \hat{e}_x \frac{L}{2}$ as a function of system size L, for various values of temperatures ($T \in [5.7, 6.5]$) at $R = 2$ and $\kappa = 3.5$. The straight lines shown in the figure are combined power-law fits of $1/L^{\eta_\theta}$ to $C_\psi(L/2)$ (shown in inset) and $1/L^{4\eta_\theta}$ to $C_{2\theta}(L/2)$.

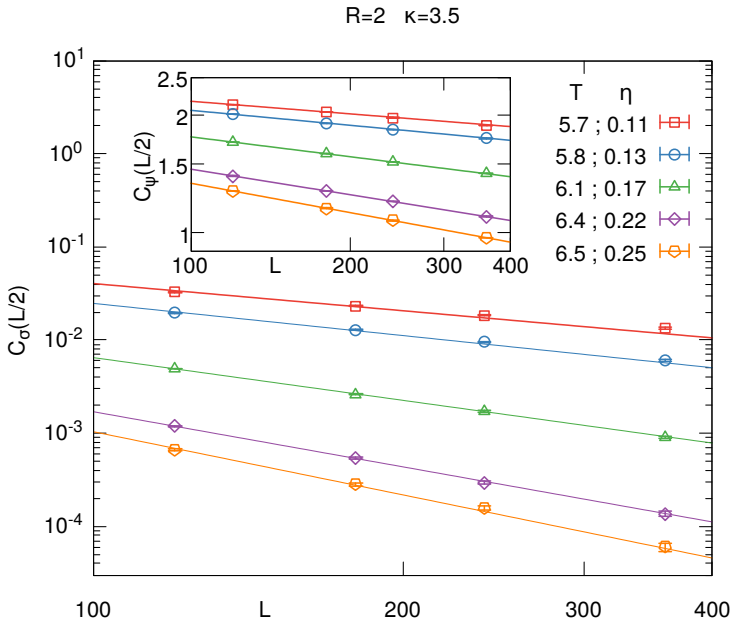

Figure 3.18: The two-point correlation function of σ, $C_\sigma(\vec{r})$ at separation $\vec{r} = \hat{e}_x \frac{L}{2}$ as a function of system size L, for various values of temperatures ($T \in [5.7, 6.5]$) at $R = 2$ and $\kappa = 3.5$. The straight lines shown in the figure are combined power-law fits of $1/L^{\eta_\theta}$ to $C_\psi(L/2)$ (shown in inset) and $1/L^{9\eta_\theta}$ to $C_\sigma(L/2)$.

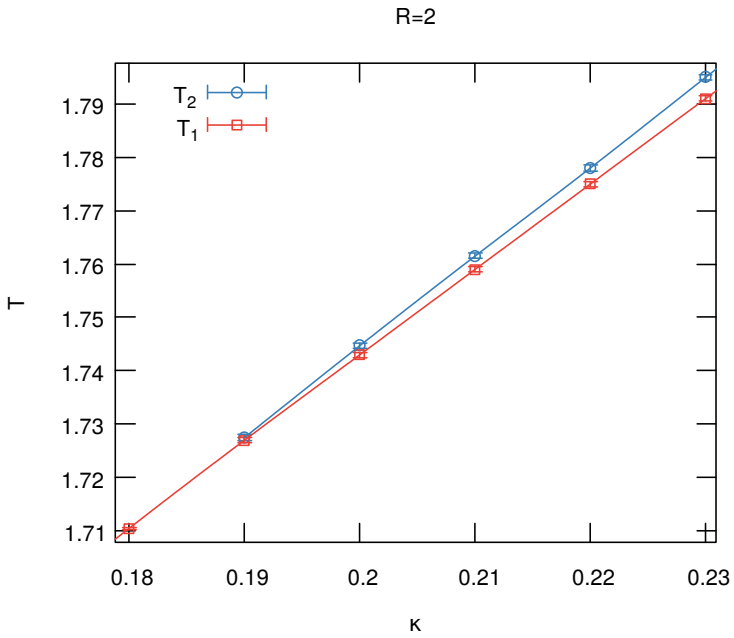

Figure 3.19: The transition temperatures, T_1 and T_2 of the two-step melting phase for $\kappa \in [0.18, 0.23]$.

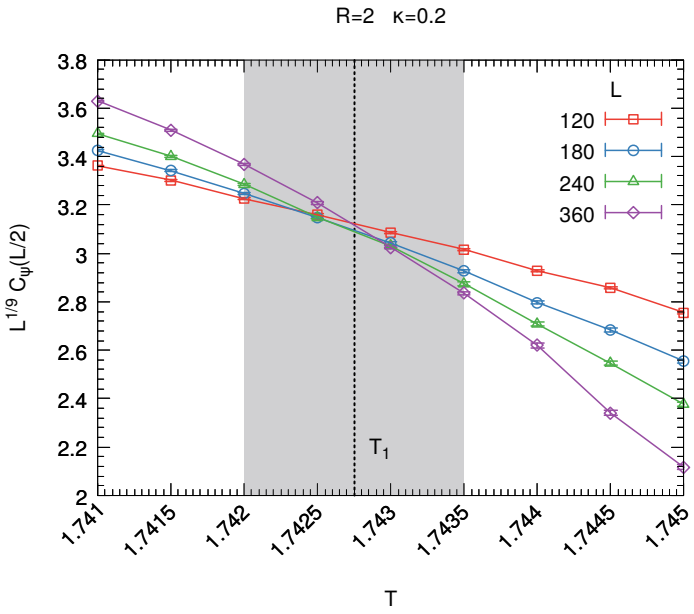

Figure 3.20: The two-point correlation function of the three-sublattice order parameter ψ, $C_\psi(\vec{r})$ at separation $\vec{r} = \hat{e}_x \frac{L}{2}$ rescaled by a factor $L^{1/9}$, as a function of temperature T for various system sizes L at $R = 2$ and $\kappa = 0.2$. At $T_1 = 1.7430(5)$, we see a crossing for the various system sizes. Lines are cubic splines and a guide for the eye.

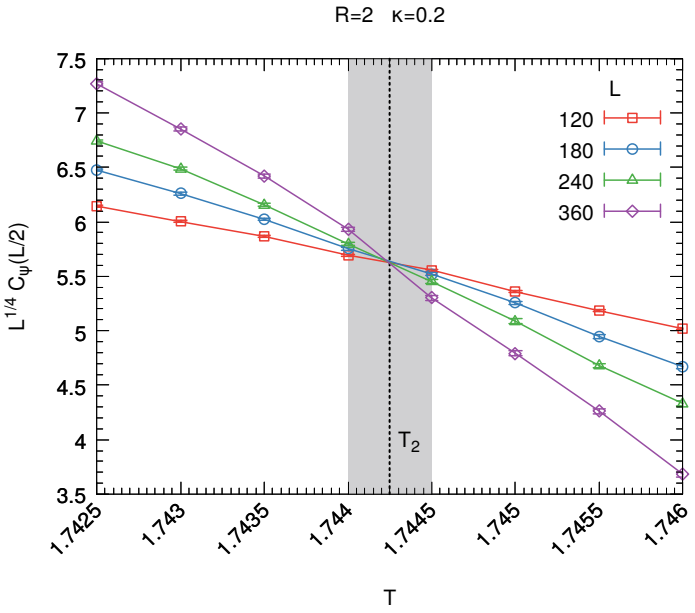

Figure 3.21: The two-point correlation function of the three-sublattice order parameter ψ, $C_\psi(\vec{r})$ at separation $\vec{r} = \hat{e}_x \frac{L}{2}$ rescaled by a factor $L^{1/4}$, as a function of temperature T for various system sizes L at $R = 2$ and $\kappa = 0.2$. At $T_2 = 1.7443(5)$, we see a crossing for various system sizes. Lines are cubic splines and a guide for the eye.

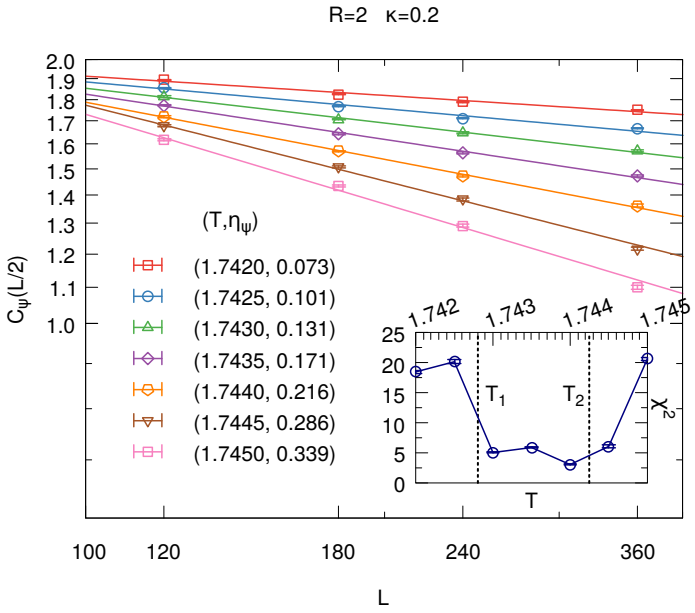

Figure 3.22: The two-point correlation function of the three-sublattice order parameter ψ, $C_\psi(\vec{r})$ at separation $\vec{r} = \hat{e}_x \frac{L}{2}$ as a function of system size L, for various values of temperatures ($T \in [1.7420, 1.7450]$) at $R = 2$ and $\kappa = 0.2$. The straight lines shown in the figure are power-law fits of $1/L^{\eta_\theta}$ to $C_\psi(L/2)$. Inset shows the χ^2 of the power-law fits of $1/L^{\eta_\theta}$ to $C_\psi(L/2)$ as a function of the temperature.

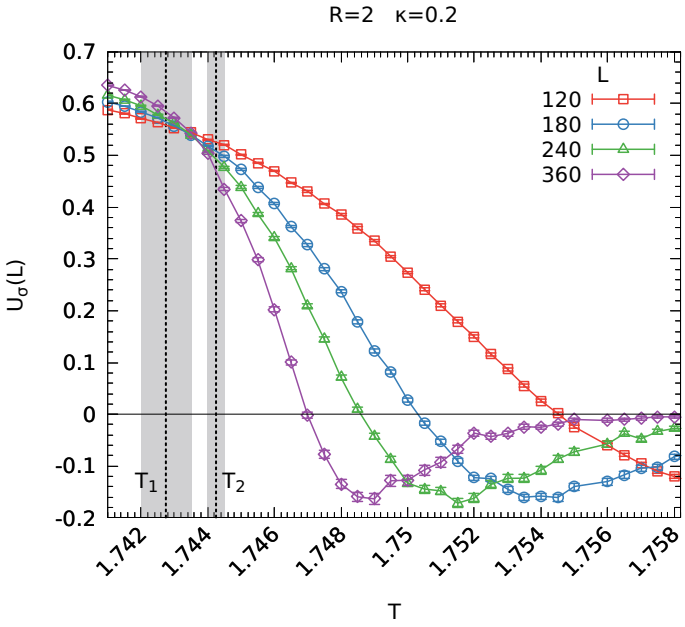

Figure 3.23: T dependence of the binder-cumulant of the order parameter σ, U_σ at $R = 2$ and $\kappa = 0.2 > \kappa_{\mathfrak{M}}$. Lines are cubic splines and a guide for the eye. Dashed vertical lines are T_1 and T_2.

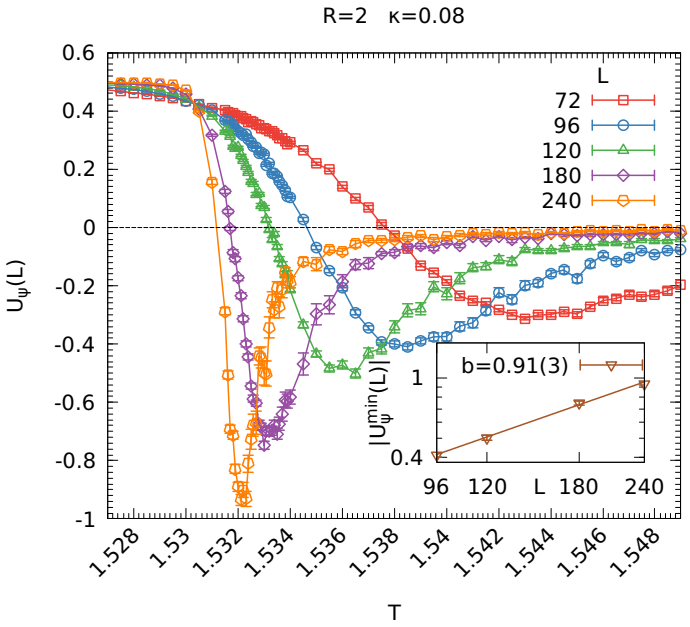

Figure 3.24: T dependence of the binder-cumulant of the order parameter ψ, U_ψ at $R = 2$ and $\kappa = 0.08 < \kappa_{\mathfrak{M}}$ for various system sizes L. Inset shows the power-law dependence of the magnitude of the peak-height on the system size L. The straight line (inset) is a power-law fit to L^b.

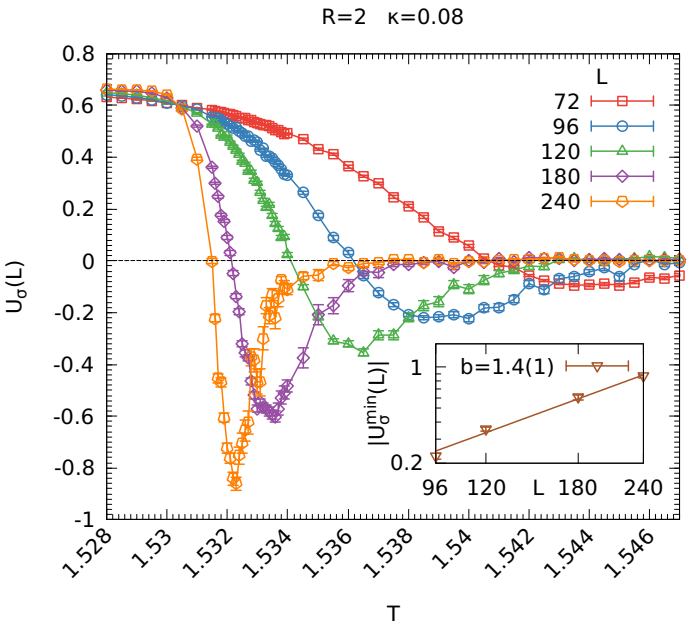

Figure 3.25: T dependence of the binder-cumulant of the order parameter σ, U_σ at $R = 2$ and $\kappa = 0.08 < \kappa_{\mathfrak{M}}$ for various system sizes L. Inset shows the power-law dependence of the magnitude of the peak-height on the system size L. The straight line (inset) is a power-law fit to L^b.

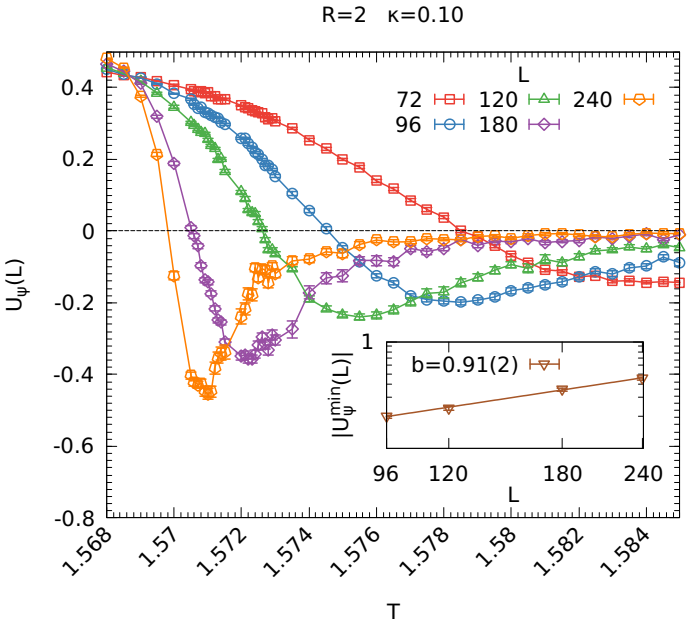

Figure 3.26: T dependence of the binder-cumulant of the order parameter ψ, U_ψ at $R = 2$ and $\kappa = 0.10 < \kappa_{\mathfrak{M}}$ for various system sizes L. Inset shows the power-law dependence of the magnitude of the peak-height on the system size L. The straight line (inset) is a power-law fit to L^b.

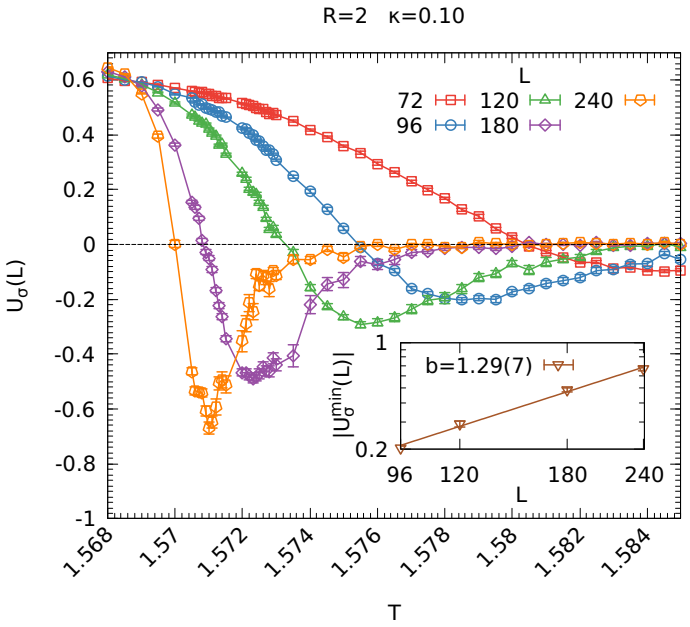

Figure 3.27: T dependence of the binder-cumulant of the order parameter σ, U_σ at $R = 2$ and $\kappa = 0.10 < \kappa_{\mathfrak{M}}$ for various system sizes L. Inset shows the power-law dependence of the magnitude of the peak-height on the system size L. The straight line (inset) is a power-law fit to L^b.

where $\langle rr' \rangle$, $\langle\langle rr' \rangle\rangle$, and $\langle\langle\langle rr' \rangle\rangle\rangle$ denote nearest neighbor, next-nearest neighbor, and next-next-nearest neighbor links of the triangular lattice as shown in Fig. 3.1, and $\sigma_r = \pm 1$ are the Ising spins at sites r of this lattice. In our convention, $J_{1/2/3} > 0$ corresponds to an antiferromagnetic coupling, while $J_{1/2/3} < 0$ corresponds to a ferromagnetic coupling. In our model, J_1 is assumed to be positive (antiferromagnetic) while J_2 and J_3 are negative (ferromagnetic). When $J_2 = J_3 = 0$, the Hamiltonian reduces to a nearest-neighbor antiferromagnetic Ising model on the triangular lattice. As described in the introduction, this model doesn't order even at low temperatures and shows an incipient power-law order at the three-sublattice wavevector in the limit $T \to 0$. Dominating ferromagnetic J_2 stabilizes a ferrimagnetic three-sublattice long-range order below a critical temperature which melts via a two-step melting process via an intermediate power-law phase, while dominating ferromagnetic J_3 stabilizes a striped order below a critical temperature. For a system with ferromagnetic J_2 and ferromagnetic J_3, the system undergoes a first-order transition from the three-sublattice ordered phase into a striped phase when J_3 starts to dominate[49]. In this work we are interested in the effect of competing ferromagnetic J_3 on the nature of the two-step melting process. To better suit this interest we re-parameterize the problem as follows: We fix $J_1 = 1$ and define R and κ such that, $R = -(J_2 + J_3)/J_1$ and $\kappa = -(J_2 - J_3)/J_1$. For a fixed value of R, we can then explore a $\kappa - T$ phase diagram. For $\kappa >> 0$, J_2 dominates stabilizing a three-sublattice order and for $\kappa << 0$, J_3 dominates stabilizing

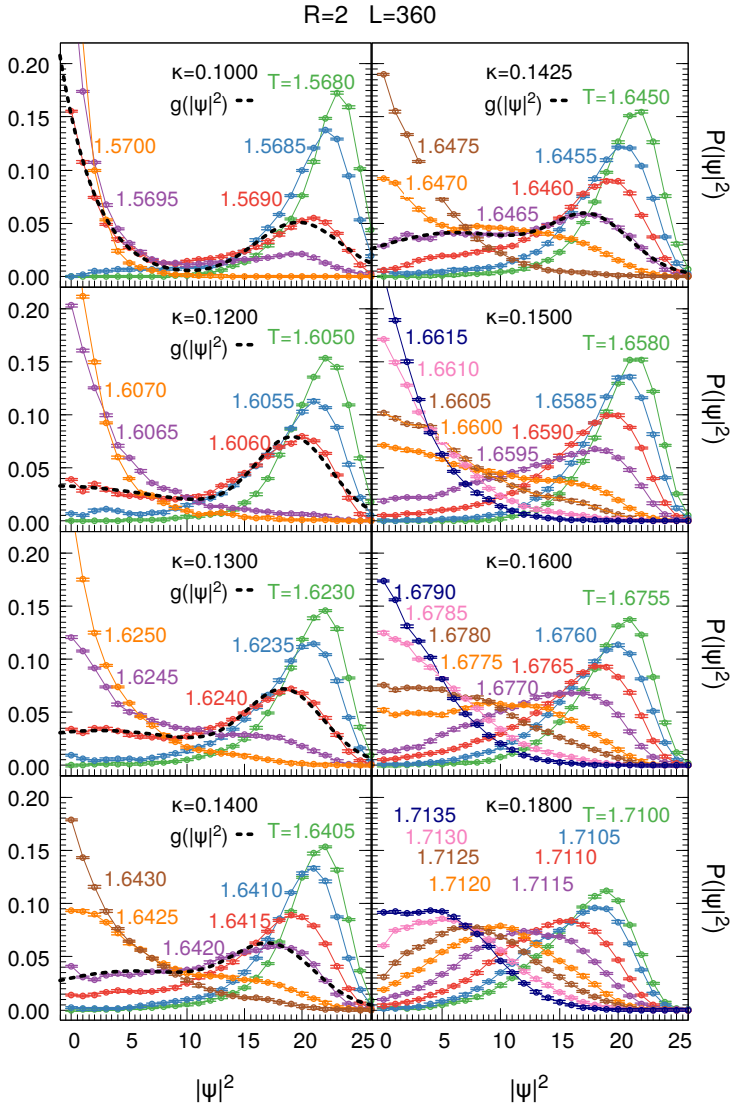

Figure 3.28: Histograms of the three-sublattice order parameter ψ, $P(|\psi|^2)$ at $R = 2$ and $L = 360$ for $\kappa \in [0.1, 0.18]$ at temperatures around the transition temperature. Dashed black lines are a bi-model gaussian fit to the double peak structure at the transition temperature.

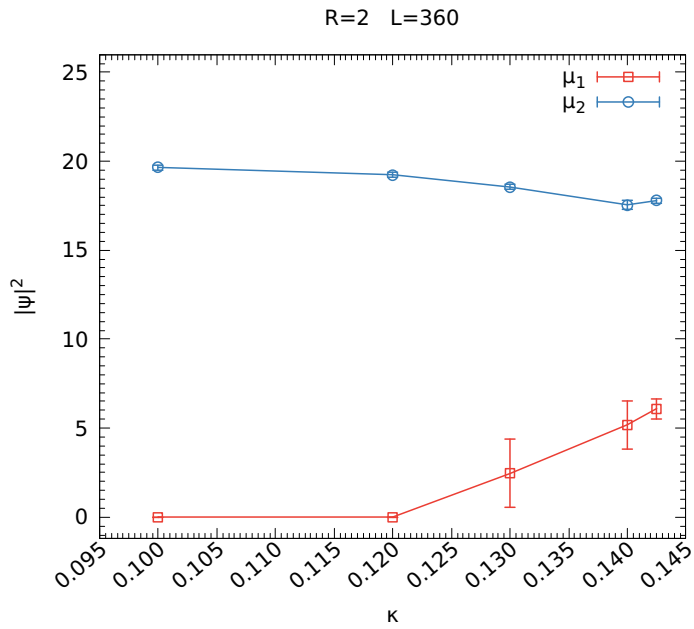

Figure 3.29: The position of the two means μ_1 and μ_2 of the bimodal Gaussian function $g(|\psi|^2)$ used to fit $P(|\psi|^2)$ as a function of $|\psi|^2$ for $\kappa \in [0.1, 0.1425]$.

a striped order. $R >> 1$, implies that $|J_2 + J_3|$ dominates over $|J1|$. $R = 2$ implies $\frac{|J_1+J_2|}{2} = |J_3|$. We first study this scenario to understand the phase diagram of the model. We normalize our temperature as $T = \frac{1}{\beta R}$.

The ferromagnetic order parameter σ is given as $\sigma = \sum_{\vec{r}} \sigma_{\vec{r}}$. We also define a complex three-sublattice order parameter $\psi \equiv |\psi| e^{i\theta}$ along the lines of [103] as follows :

$$\psi = -\sum_{\vec{r}} e^{i\frac{2\pi}{3}(m+n)} \sigma_{\vec{r}} \tag{3.7}$$

where $\theta = \frac{2\pi}{3}(m+n)$ and the sites of the lattice are labeled as $\vec{r} = m\hat{e}_x + n\hat{e}_y$. Additionally, we also define and measure $cos(\theta)$, $cos(2\theta)$ and $cos(3\theta)$ correlators which as explained in Section.3.3 find direct analogues in the six-state clock model. From Eq.[3.7] it is clear that the correlators of $cos(3\theta)$ and $cos(\theta)$ are proportional to the correlators of σ and ψ respectively.

The fact that we have to investigate a critical power-law phase calls for the use of efficient non-local Monte Carlo algorithm, which don't suffer the usual critical slowing-down experienced by local updates. We use two efficient dual-lattice worm algorithms developed in Ref. [49] to numerically investigate the phase diagram of our model at $R = 2$, in the $\kappa - T$ plane. Our data for the triangular lattice model is obtained with $2 * 10^7$ MCS and a $2 * 10^5$ MCS equilibration time. One MCS is defined as one lattice sweep of single spin-flip metropolis updates followed by N_w number of worm updates such that $N_w \times$ average number of dual-lattice sites visited by a worm = N, the number of dual-lattice sites. The largest lattice size we measure is a 360×360 lattice with toric

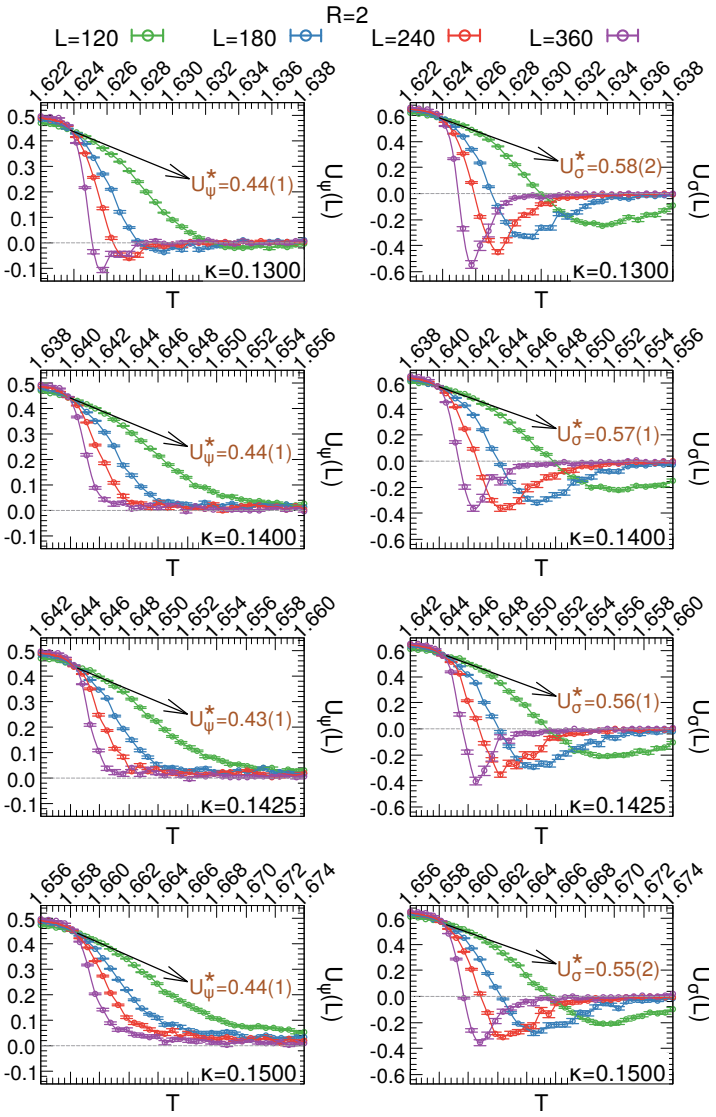

Figure 3.30: T dependence of the binder-cumulants, U_ψ (left panel) and U_σ (right panel) at $R = 2$ for $\kappa \in [0.1300, 0.1500]$. Lines are cubic splines and a guide for the eye.

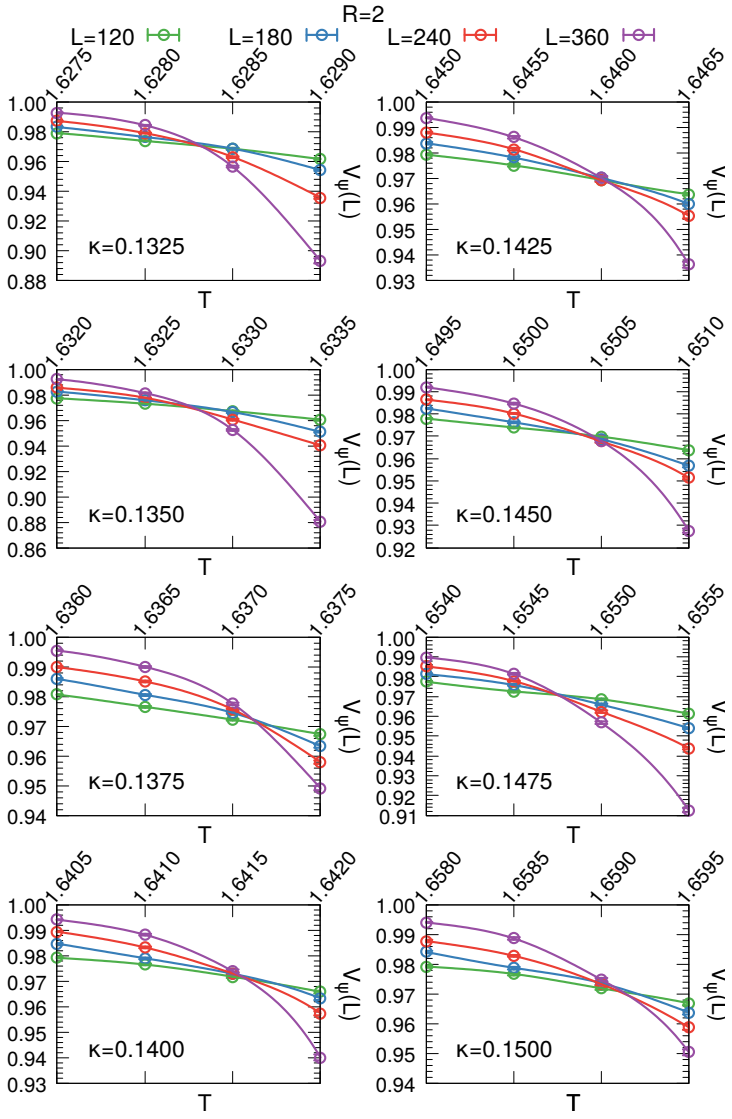

Figure 3.31: Ratio of the two-point correlation functions of ψ at separation $L/2$ and $L/4$, $C_\psi(L/2)/C_\psi(L/4)$ for $\kappa \in [0.1325, 0.1500]$ at $R = 2$ as a function of temperature T. Lines are cubic splines and a guide for the eye.

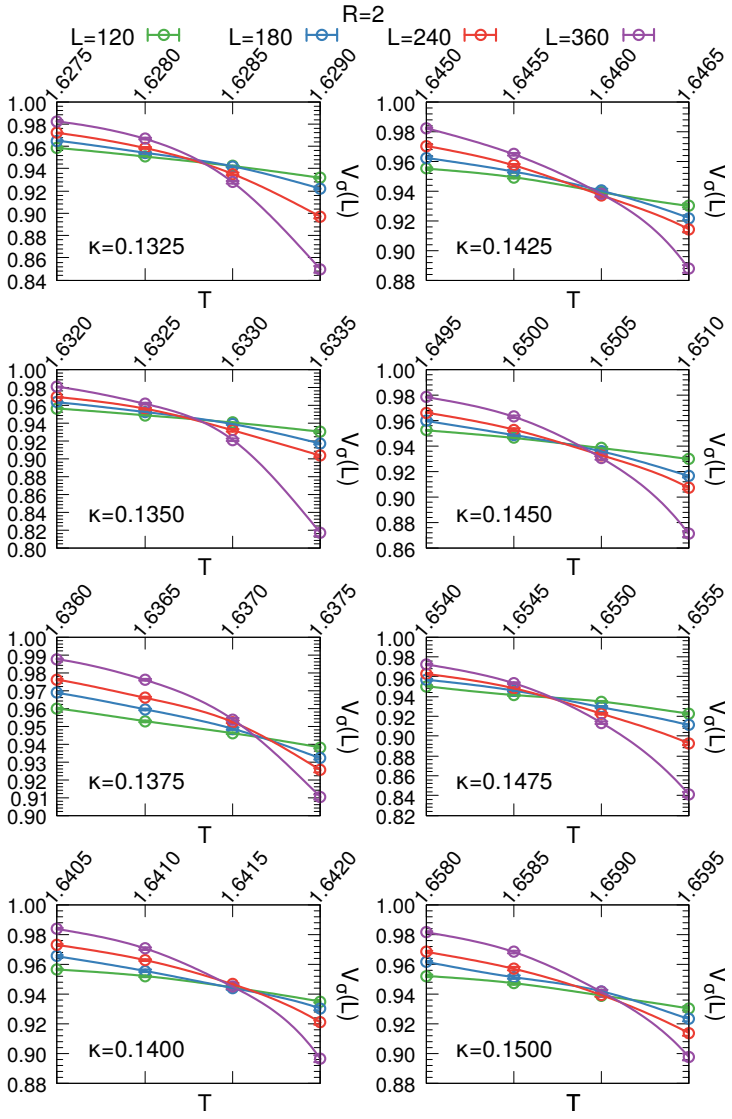

Figure 3.32: Ratio of the two-point correlation functions of σ at separation $L/2$ and $L/4$, $C_\sigma(L/2)/C_\sigma(L/4)$ for $\kappa \in [0.1325, 0.1500]$ at $R = 2$ as a function of temperature T. Lines are cubic splines and a guide for the eye.

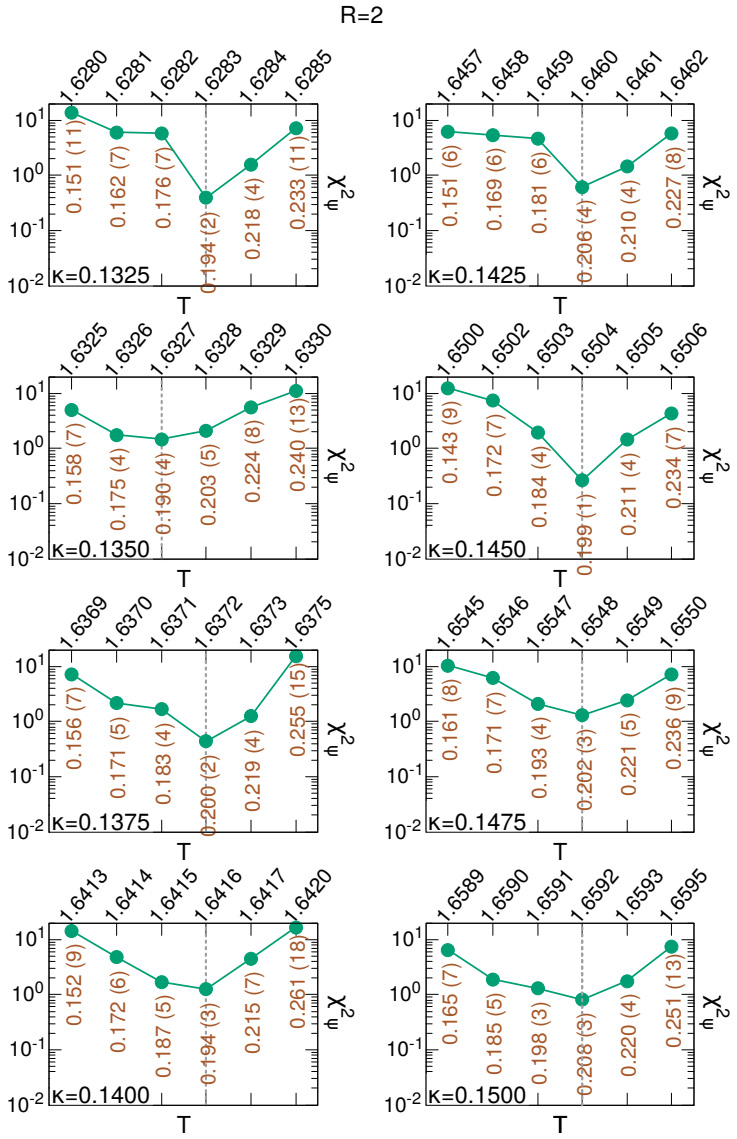

Figure 3.33: χ^2 (green dots) of power-law fits of $1/L^{\eta_\theta}$ to $C_\psi(L/2)$ as a function of T for $\kappa \in [0.1325, 0.15]$ at $R = 2$. The labelled numbers are the values of η_θ of the power-law fit. The grey dotted line corresponds to our estimate of the critical temperature extracted from Fig. 3.31. Lines connect the data points and are a guide for the eye.

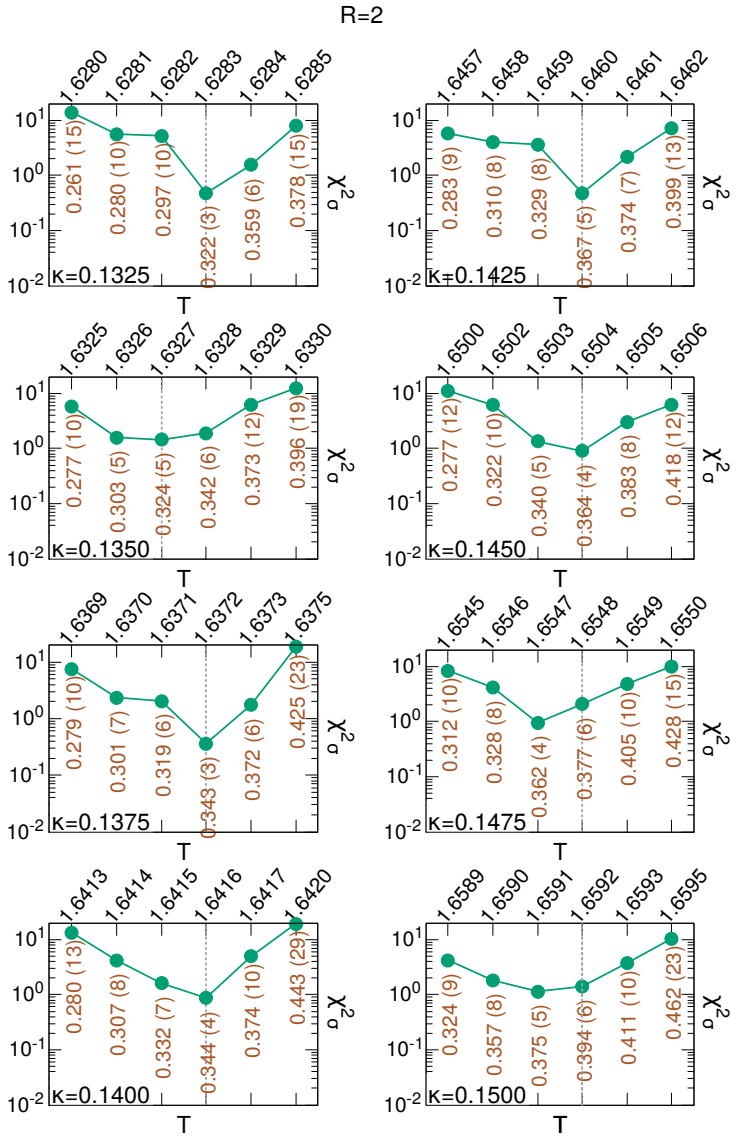

Figure 3.34: χ^2 (solid circles) of power-law fits of $1/L^{\eta_{3\theta}}$ to $C_\sigma(L/2)$ as a function of T for $\kappa \in [0.1325, 0.15]$ at $R = 2$. The labelled numbers are the values of $\eta_{3\theta}$ of the power-law fit. The grey dotted line corresponds to our estimate of the critical temperature extracted from Fig. 3.32. Lines connect the data points and are a guide for the eye.

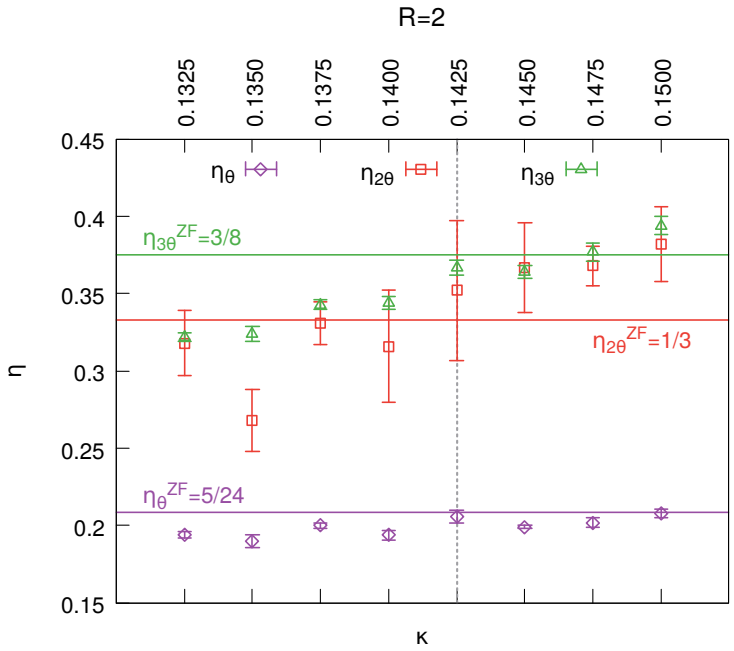

Figure 3.35: Values of η_θ, $\eta_{2\theta}$ and $\eta_{3\theta}$ measured for $\kappa \in [0.1325, 0.15]$. The solid lines represent the value of η as predicted by the Z_6 self-dual parafermionic conformal field theory constructed by Zamolodchikov and Fateev[98].

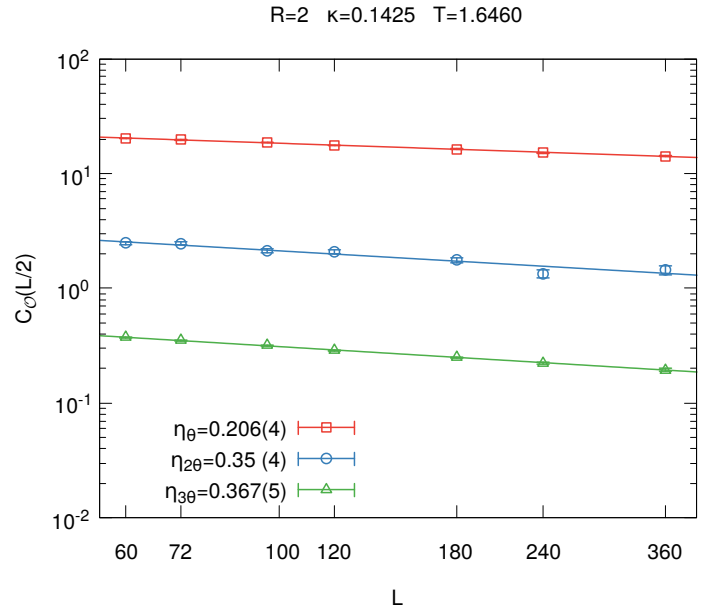

Figure 3.36: L dependence of $C_{\mathcal{O}}(L/2)$ ($\mathcal{O} = \psi, cos(2\theta), \sigma$), evaluated at the estimated location of the multicritical point $\mathfrak{M}$, $[\kappa_{\mathfrak{M}}, T_{\mathfrak{M}}] = [1.1425, 1.6460]$. Lines denote fits to $1/L^{\eta_{\mathcal{O}}}$. C_ψ is rescaled by a factor of 10 for clarity.

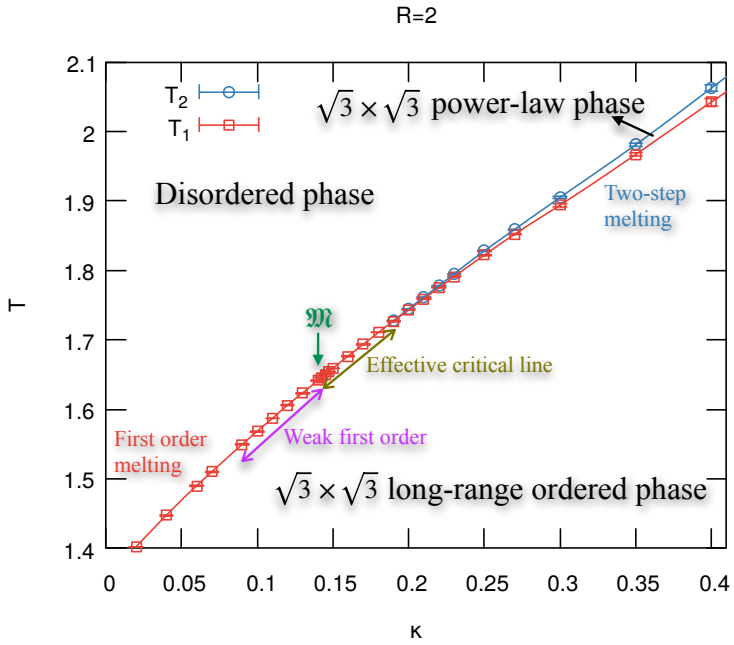

Figure 3.37: $\kappa - T$ phase diagram of the Ising model on the triangular lattice with antiferromagnetic nearest neighbor (J_1), ferromagnetic next-nearest neighbor (J_2) and ferromagnetic next-next-nearest neighbor (J_3) interactions at $R = 2$. Lines are cubic splines and a guide for the eye.

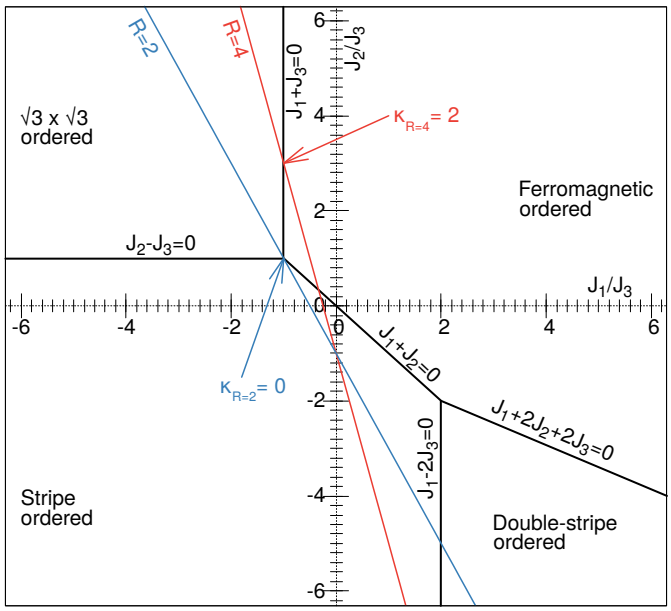

Figure 3.38: The ground-state spin configuration of the J_1, J_2, J_3 Ising model on the triangular lattice for a ferromagnetic J_3. Reproduced from Ref. [42].

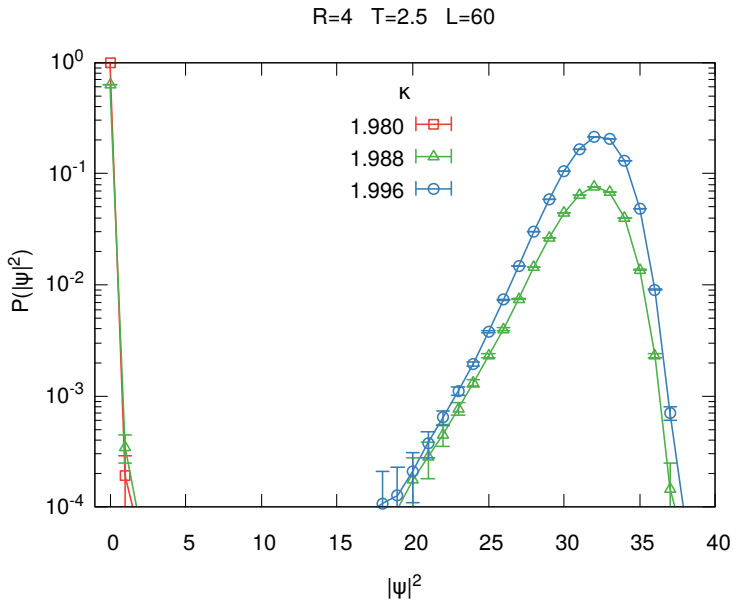

Figure 3.39: Histogram of the three-sublattice order parameter, $P(|\psi|^2)$ for various κ at $R = 4$ for a fixed $T = 2.5$. Lines are cubic splines and a guide for the eye.

boundary conditions.

At $R = 2$ and $\kappa = 3.5$, we find that the effect of the ferromagnetic next-nearest neighbor interactions J_2 clearly dominates over the ferromagnetic next-next-nearest neighbor interactions J_3 and we are in the two-step melting regime with a three-sublattice ordered ground state stabilized by ferromagnetic J_2. The intermediate critical region bounded by T_1 and T_2, the lower and upper critical transition temperatures respectively, is defined by power-law correlations of the three-sublattice order parameter, $C_\psi \sim C_\theta \sim 1/L^{\eta_\theta}$, where $\eta_\theta(T) \in [1/9, 1/4]$ for $T \in [T_1, T_2]$. As in the case of the six-state clock model, this intermediate power-law region accepts a Gaussian description and thus $C_{2\theta} \sim 1/L^{4\eta_\theta}$ and $C_\sigma \sim C_{3\theta} \sim 1/L^{9\eta_\theta}$. Fig. 3.15 and Fig. 3.16 show $C_\psi(L/2)$ rescaled by a factor of $L^{1/9}$ and $L^{1/4}$ respectively as a function of T at $R = 2$ and $\kappa = 3.5$. Following the above arguments both show a *crossing* at $T_1 = 5.70(5)$ and $T_2 = 6.50(5)$ respectively for various L. Fig. 3.17 and Fig. 3.18 show joint fits of $C_\psi(L/2) \sim 1/L^\eta$ with $C_{2\theta} \sim 1/L^{4\eta}$ and $C_\sigma \sim 1/L^{9\eta}$ respectively for $T \in [T_1 = 5.7, T_2 = 6.5]$. We find $\eta \in [0.11 \sim 1/9, 0.25 = 1/4]$ as expected. The width of the two step melting at $R = 2$ and $\kappa = 3.5$ is $\Delta T = 0.8$. As we decrease κ, we find the ΔT decreases and the lower and upper critical transition lines approach a pinch-off point at which $\Delta T \geq \delta T_1, 2$. Fig.3.19 shows T_1 and T_2 as a function of κ for $\kappa \in [0.18, 0.23]$ in the vicinity of the pinch-off point. At $\kappa = 0.2$, we find the last resolvable T_1 and T_2 for which $\Delta T < \delta T_1, 2$. Fig. 3.20 and Fig. 3.21 show $C_\psi(L/2)$ rescaled by a factor of $L^{1/9}$ and $L^{1/4}$ respectively as a function of T at $R = 2$ and $\kappa = 0.2$. Both these functions show a *crossing* at $T_1 = 1.74275(75)$ and $T_2 = 1.74425(25)$ respectively for various L. Fig. 3.22 shows $C_\psi(L/2)$ plotted as a function of system size L for various $T \in [1.742, 1.745]$. Lines are power-law fits to

L_θ^η. η_θ increases with increasing T with $\eta_\theta = 0.13 \sim 1/9$ at $T = 1.743 \sim T_1$ and $\eta_\theta = 0.216 \sim 1/4$ at $T = 1.7440 \sim T_2$. Inset of Fig. 3.22 shows the χ^2 of the power-law fits of $C_\psi(L/2)$ to $1/L^\eta$ as a function of T. We see a clear minima in the χ^2 of the fits between $T_1 = 1.74275$ and $T_2 = 1.74425$ (indicated by dashed vertical lines) as expected. Fig. 3.23 shows the binder-cumulant $U_\sigma(L)$ as a function of T for various L at $\kappa = 0.2$. Even though at $\kappa = 0.2$, the system is in the two-step melting regime, just as in the case of the six-state clock model, we see negative peaks in the binder-cumulant that do not scale with L. This suggests a possible line of weak first-order transitions meeting the pinch-off point of the two-step melting transition defining a multicritical point at similar to the one found in the six-state clock model. As mentioned in Section.3.3, the pinch-off point of the two-step melting transition overestimates the location of a possible multicritical point. Hence we go to a small enough κ and approach $\kappa_{\mathfrak{M}}$ from the left ($\kappa \to \kappa_{\mathfrak{M}}^-$). We look at $\kappa = 0.08 < \kappa_{\mathfrak{M}}$. Fig. 3.24 and 3.25 show $U_\psi(L)$ and $U_\sigma(L)$ respectively as a function of T for various system sizes. Both binder-cumulants show negative peaks which scale with the system size L with a *crossing* behavior at the transition temperature. Inset in Fig. 3.24 and 3.25 plots the height of the negative peaks as a function of system size L. Lines are fits to a power-law of the form L^b. $U_\psi^{\min}(L)$ scales as $L^{0.91}$ and $U_\sigma^{\min}(L)$ scales as $L^{1.4}$. As discussed in Section. 3.2 and seen in Section. 3.3, a scaling of the negative peaks in the binder-cumulant softer than L^2 indicates a weak-first order transition at $\kappa = 0.08$. At $\kappa = 0.1$, the system continues to exhibit a weak first-order transition as seen in the negative peaks of $U_\psi(L)$ and $U_\sigma(L)$ shown in Fig. 3.26 and 3.27 respectively. Inset of Fig. 3.26 and 3.27 show that $U_\psi^{\min}(L)$ scales as $L^{0.91}$ and $U_\sigma^{\min}(L)$ scales as $L^{1.29}$ at $\kappa = 0.1$, showing the increasingly weak first-order behavior of the melting transition as $\kappa \to \kappa_{\mathfrak{M}}^-$. As further confirmation of this weakening first-order behavior, we plot the histogram of the three-sublattice order-parameter $P(|\psi|^2)$ as a function of $|\psi|^2$ in Fig. 3.28 at temperatures across the transition temperature for various $\kappa \in [0.1, 0.18] < \kappa_{\mathfrak{M}}$. The black dashed-lines in the panels for $\kappa = 0.1, 0.12, 0.13, 0.14$ and 0.1425 show a bi-modal Gaussian fit $g(|\psi|^2)$ to the histogram at the transition temperature. We see a clear double peak structure in the histogram for $\kappa = 0.1$ at the transition temperature of $T = 1.5690$. Fig. 3.29 shows the position of the two means μ_1 and μ_2 of $g(|\psi|^2)$ for $\kappa \in [0.1, 0.1425]$. As we increase κ, it is clear that the distance between the two peaks decreases indicating a weakening first-order transition. At $\kappa = 0.18$ from the bottom-left panel of Fig. 3.28 it is clear that the system undergoes a continuous transition indicated by the smoothly shifting position of single peaked histograms of the order parameter across the transition temperature. This is not surprising because, although we found the pinch-ooff point of the two-step melting region to be at $\kappa = 0.2$, the system, just as in the case of the six-state clock model would continue to be in the two-step melting region for $\kappa < 0.2$ and $\kappa > \kappa_{\mathfrak{M}}$. Finite-size and finite-time nature of Monte-Carlo simulations is unable to resolve the two-step melting transition in this

small sliver of κ. To pin-point the location of the multicritical point we draw parallels with the behavior of U_θ and $U_{3\theta}$ of the six-state clock model in the vicinity of the multicritical point and look at U_ψ and U_σ as a function of T in Fig. 3.30 for $\kappa \in [0.13, 0.15]$. The left and right panel show $U_\psi(L)$ and $U_\sigma(L)$ respectively. At $\kappa = 0.13$, both $U_\psi(L)$ and $U_{sigma}(L)$ show negative peaks due to the weak first-order nature of the transition at $\kappa = 0.13$. As we increase κ, the height of the negative peaks for both the binder-cumulants decreases and finally at $\kappa = 0.1425$, we see that $U_\psi(L)$ becomes monotonic and bounded between $[0, 1/2]$. $U_\sigma(L)$ continues to have negative peaks for $\kappa > 0.1425$ and well into the two-step melting region at $\kappa = 0.2$ as seen in Fig. 3.23. This is similar to what we find in the six-state clock model and gives us a clue about the nature and location of a multicritical point. In the six-state clock model, the multicritical line lies on the self-dual line and is defined by the transition temperature $T_{\mathfrak{M}} = 1$. We only had to explore the $1-$dimensional t-space to pinpoint the location of the multicritical point. In the triangular lattice model we need to explore a $2-$dimensional (κ, T) space. To this end, we first accurately determine a line of transition temperatures for $\kappa \in [0.13, 0.15]$. We look at correlation ratios (described in Section. 3.2) $V_\psi(L)$ and $V_\sigma(L)$. Fig. 3.31 and Fig.3.32 show $V_\psi(L)$ and $V_\sigma(L)$ for various L as a function of T for $\kappa \in [0.1325, 0.15]$. As described in Section. 3.2 the *crossing* point of $V(L)$ for various L determines the transition temperature. Using this we are able to determine the transition temperature to an accuracy of $\delta T = 0.0005$, which is the spacing of our temperature grid for these measurements. To further the accuracy of out transition temperature measurements, we look at a finer grid of $\delta T = 0.0001$ around the transition temperature T, defined by the crossing point of $V(L)$ and fit power-laws of the form $1/L^{\eta_\theta}$, $1/L^{\eta_{2\theta}}$ and $1/L^{\eta_{3\theta}}$ to $C_\psi(L/2)$, $C_{2\theta}(L/2)$ and $C_\sigma(L/2)$ respectively for $\kappa \in [0.1325, 0.15]$. For $\kappa < \kappa_{MC}$, we have a line of weak first order transitions. At finite-sizes, they define an effective critical transition because the correlation length is generally very very large at the transition temperature. For $\kappa > \kappa_{\mathfrak{M}}$ and < 0.2, we have a single effective continuous transition due to the unresolvability of the two-step melting as a result of the finite-size and finite-time nature of our simulations. Thus for $\kappa \in [0.1325, \kappa_{\mathfrak{M}}, 0.15]$, we have a single effective transition temperature, defined by effective critical exponents η_θ, $\eta_{2\theta}$ and $\eta_{3\theta}$. Fig. 3.33 and Fig. 3.34 show the χ^2_ψ and χ^2_σ of the $1/L^{\eta_\theta}$ and $1/L^{\eta_{3\theta}}$ fits respectively in a finer grid of temperatures around the transition temperature for $\kappa \in [0.1325, 0.15]$. At the same temperature for a given κ both χ^2_ψ and χ^2_ψ show a clear minima defining a transition temperature with an accuracy of $\delta T = 0.0001$. The points are labelled with the values of the critical exponents η. Fig. 3.35 shows the values of η_θ, $\eta_{2\theta}$ and $\eta_{3\theta}$ as a function of κ for $\kappa \in [0.1325, 0.15]$. Solid lines show the values of η^{ZF}_θ, $\eta^{ZF}_{2\theta}$ and $\eta^{ZF}_{3\theta}$. At $\kappa = \kappa_{\mathfrak{M}} = 0.1425(25)$ we find the best match with the values predicted by the CFT. As shown above, $\kappa = 0.1425$ is the point at which $U_\psi(L)$ becomes monotonic while $U_\sigma(L)$ continues to be non-monotonic for $\kappa = \kappa_{\mathfrak{M}} > 0.1425$ just as in the case of

the six-state clock model. Our best estimate for the location of the multicritical point on the triangular lattice model is $(\kappa_{\mathfrak{M}}, T_{\mathfrak{M}}) = (0.1425(25), 1.6460(1))$. Fig. 3.36 shows the power-law fits of $1/L^{\eta_\theta}$, $1/L^{\eta_{2\theta}}$ and $1/L^{\eta_{3\theta}}$ to $C_\psi(L/2)$, $C_{2\theta}(L/2)$ and $C_\sigma(L/2)$ respectively at $\kappa = 0.1425$ and $T = 1.6460$. We find $\eta_\theta = 0.206(4)$, $\eta_{2\theta} = 0.35(4)$ and $\eta_{3\theta} = 0.367(5)$ which match very well with the values predicted by the Z_6 parafermionic CTF. As further proof of the similarity of the multicritical points in both the models, the critical value of the binder-cumulants, U^*_θ and $U^*_{3\theta}$ of the six-state clock model shown in Fig. 3.13 at $t = t_{\mathfrak{M}} = 0.342$ matches within error-bars of U^*_ψ and U^*_σ of the six-state clock model shown in Fig. 3.30 at $\kappa = \kappa_{\mathfrak{M}} = 0.1425$. Fig. 3.37 summarizes the phase diagram of the triangular lattice model at $R = 2$. Fig. 3.38 reproduces the ground-state sping configurations for a J_1, J_2, J_3 Ising model on a triangular lattice calculated by Tanaka and Uryû for a ferromagnetic J_3. The $R = 2$ line directly connects the three-sublattice ordered state stabilized by a ferromagnetic J_2, with a stripe ordered phase stabilized by a ferromagnetic J_3. The three-sublattice ordered ground-state meets the stripe ordered ground state on the $R = 2$ line at $\kappa = 0$. For $\kappa = \epsilon$, where ϵ is a small number, the three-sublattice ordered state was shown to melt via a first-order transition at a finite temperature [49]. For $\kappa = -\epsilon$ the stripe ordered state was shown to melt via a first-order transition at a finite temperature. Separating the two states it was shown that there is a line of first order transitions. Even though J_1 is antiferromagnetic, a ferromagnetic ground state can be stabilized from a three-sublattice ordered state by decreasing κ (increasing J_3) along the $R = 4$ line. Fig. 3.39 shows the histogram of the three-sublattice order parameter, $P(|\psi|^2)$ at $R = 4$ and a finite $T = 2.5$. At $\kappa = 1.996$, we see a single peak at a non-zero value of $|\psi|^2$, suggesting that the system is in a three-sublattice ordered state. At $\kappa = 1.980$, we a single peak at 0, suggesting that the system is no longer three-sublattice ordered. Instead the system is in a ferromagnetic ordered state. At an intermediate $\kappa = 1.988$, we find that a double peaked structure in the histogram. This suggests that a line of first order transitions separates the three-sublattice ordered state and a ferromagnetic ordered state.

3.5 Summary

The multicritical point in both the models has a two-step melting transition pinching-off on one side and a weakening first order transition on the other side. Numerically, the two-step melting pinches off well before reaching the multicritical point due to finite-size and finite-time effects. This effectively leaves the multicritical point straddled by an effective continuous transition and a weak first-order transition. Distinguishing between a weak-first order transition and a continuous transition using Monte-Carlo methods is very hard, since the weak first-order transition exhibits pseudo-critical be-

havior for system sizes less than the very large correlation length at the weak first-order transition. Recently some sophisticated methods have been proposed to distinguish between the two transitions. In our case, since we already know the expected value of the critical exponents η at the multicritical point, we just need to find the transition temperatures around the vicinity of the multicritical point and measure η to high accuracy, to match with the known values and hence were able to pin-point the multicritical point. The multicritical point on the triangular lattice model is (to our knowledge) the first example of a multicritical point on a microscopic model described by a CFT. There are ordered phases with different melting scenarios in the generalised J_1, J_2 and J_3 Ising models on the triangular and Kagome lattices which probably lead to other types of multicritical points. We wish to return to those in future works. The phase diagram of the Ising antiferromagnet on the Kagome lattice with next-nearest and next-next nearest neighbor interactions has a similar two-step melting transition pinching off into a first-order transition since the ground states stabilized by these interactions on the Kagome lattice are similar to the ones on the triangular lattice. It would be interesting to know the properties of that multicritical point and see if it falls in the same universality class. Recently discovered $TmMgGaO_4$ can be modeled using the effective Hamiltonian:

$$H = J_1 \sum_{\langle ij \rangle} S_i^z S_j^z + J_2 \sum_{\langle\langle ij \rangle\rangle} S_i^z S_j^z - \mu \sum_i S_i^z \tag{3.8}$$

where $i \in$ sites of a triangular lattice with $J_1, J_2 > 0$ and $J_2 \sim 0.09 J_1$. $TmMgGaO_4$ shows stripe order at zero field below $T \sim 0.27K$. This is equivalent to the $J_1 > 0, J_2 = 0$ and $J_3 < 0$ case in our model. It would be interesting to see if such materials can be tuned to support three-sublattice order, providing experimental equivalence of a pinch-off point.

Chapter 4

Hard squares at full packing on a cubic lattice

In the previous chapter, we dealt with a spin model where the order disorder transition is facilitated by the interplay of internal energy and entropy. Hard object models with no interaction energy between the objects are examples of entropic models with the configurational energy being zero. The only way the object *talk* to each other is through their hard core repulsion which implies that they cannot overlap. A typical configuration of hard objects will have an entropy associated with it. Any transition the system undergoes will be an entropic transition. Such entropic transitions can be driven by introducing vacancies in the system or anisotropy in fugacities of the hard objects. Hard object models both *on* and *off* lattice have been continuously studied. An *off* lattice example is the hard sphere gas whose liquid to solid transition has been of continuous interest[113]. An well studied example of an hard object model on the lattice is the dimer model. The dimer model consists of sites forming a lattice and edges connecting the sites. Each edge can be occupied by a dimer or be empty. Hard dimers implies that each edge is occupied by only one dimer such that no two dimers touch each other. This implies that each site of the lattice can be touched by exactly one dimer. The full packing limit of this problem implies that every lattice site is touched by one dimer. This dimer model on a planar square lattice can be solved by writing the partition function in terms of a Pfaffian[114]. Apart from mathematical intrigue, these dimer models serve as important dual mappings of various spin models. The 2d Ising model can be mapped to a dimer model on the fisher lattice and can be solved exactly[115]. The Rokshar-Kivelson quantum dimer model was proposed as a model for high temperature superconductivity where the dimers represent singlet states between electrons of neighbouring sites[116]. The classical dimer model is a limiting case of this model where the dynamics of the quantum model can be represented as dimer flips in the classical case.The quantum wave-function of the quantum dimer model can be rep-

resented as a superposition of all classical dimer coverings. In the previous chapters we used the fact that a antiferromagnetic Ising model on the triangular lattice can be mapped to a dimer model on the dual honeycomb lattice to construct worm algorithms for the dimer model. The classical dimer model in a 2d square lattice is a prototypical example of a model for entropic considerations with the configurational energy being zero. Entropy in the system arises from the notion that dimers can flip freely as long as they don't violate the hard core condition. This results in a pair of dimer flipping freely on a bipartite lattice. The classical square lattice dimer model has been explored in the presence of vacancies. Other types of hard object have also been studied as mentioned in Chapter 1. One such is model is hard squares on a square lattice. At full packing, this model is in a columnar ordered state which destabilises into a disordered fluid at finite vacancy density[66]. A model of a mixture of hard squares and dimers has also been previously studied[66]. In this case, the columnar order under goes a KT transition into a power-law ordered state at finite dimer density. A mixture of hard-squares, dimers and vacancies has also been studied[66]. It was shown that the KT transition from finite dimer density and the order disorder transition from finite vacancy density are connected by a line of Ashkin-Teller criticality with exponents depending on the ratio of dimers and vacanies. In this chapter we study the problem of anisotropic hard squares on a cubic lattice. Anisotropy here refers to the different fugacities for differently oriented squares. Our motivation to study this problem comes from trying to generalise the problem of squares and dimers on a 2d square lattice. In the limit of the fugacity of z-normal oriented squares (z-squares) becoming zero, one can reduce the 3d problem into decoupled 2d layers of hard-squares on the XY plane. A small density of z-normal plates then couples these layers. The projection of z-normal plates on the 2d XY plane can be thought of as dimers on the XY plane.

4.1 Model

We consider a system of hard squares on a cubic lattice at full packing as shown in Fig.4.1. The cubic lattice is of a linear dimension L, with the total number of lattice sites $N = L^3$. A hard plate occupies four sites on this lattice. With periodic boundary conditions the lattice can be populated with hard squares which do not touch each other such that every site of the lattice belongs uniquely to one hard plate. We distinguish the hard squares on the basis of the Cartesian direction in which their normals are pointing. Thus x, y and z-type squares have their normals in the x, y and z directions. We assign fugacities to each of the three types of squares: s_x, s_y and s_z. The partition function of

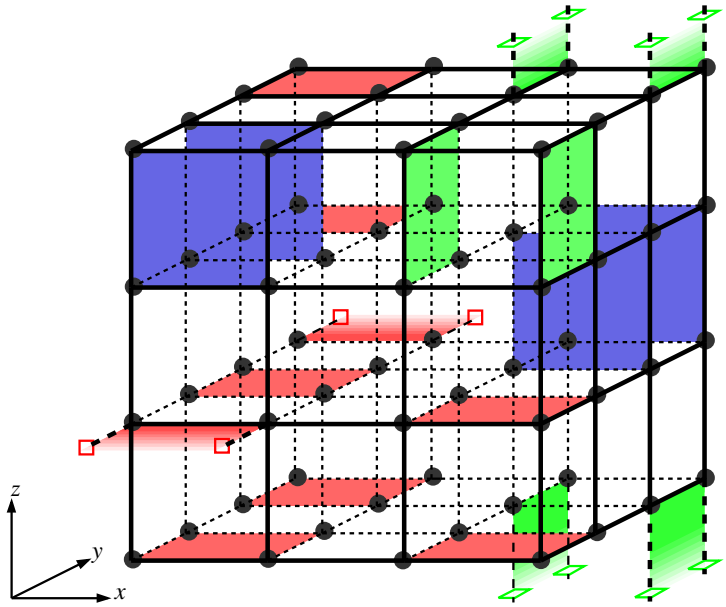

Figure 4.1: A sample configuration of hard squares at full packing on the cubic lattice with $L = 4$. Hard squares are objects which occupy four lattice sites with the property that no two squares share one or more lattice sites. At full packing each lattice site uniquely belongs to a hard plate. x, y and z-type squares are colored green, blue and red respectively.

the system is then given by:

$$Z = \sum_{C} (s_x)^{n_x} (s_y)^{n_y} (s_z)^{n_z} \tag{4.1}$$

where the sum extends over all allowed configurations C. n_x, n_y and n_z are the number of x, y and z-type squares respectively with s_x, s_y and s_z as their respective fugacities. In this work we study the system at the isotropic point which is defined by $s_x = s_y = s_z = 1$. We also study the system by setting the fugacities s_x and s_y to be equal and varying the fugacity s_z. We explore the phase diagram as a function of s_z.

4.2 Methods

We simulate the system using local and non-local updates. The local updates are of two types as shown in Fig. 4.2 and 4.3. Fig. 4.2 shows a 'ring' type exchange, where a two adjacent squares of the same type, say x-type, belonging to a cube can rotate into two y-type or two z-type squares. Fig. 4.3 shows a 'shift' type exchange, wherein a plate slides across a cube consisting of two adjacent squares.

By using only the two local updates above, ergodicity in the configuration space of the system cannot be achieved as the local moves can not change winding numbers. We supplement the local updates with a pocket cluster algorithm[95] explained in detail

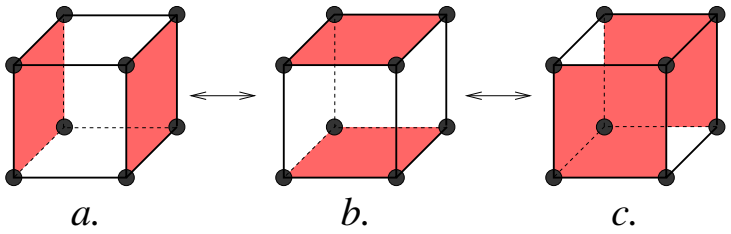

Figure 4.2: A local update which consists of 'ring' exchange of squares on a cube where two adjacent x-type squares belonging to a cube can rotate into two y-type squares or two z-type squares and vice-versa.

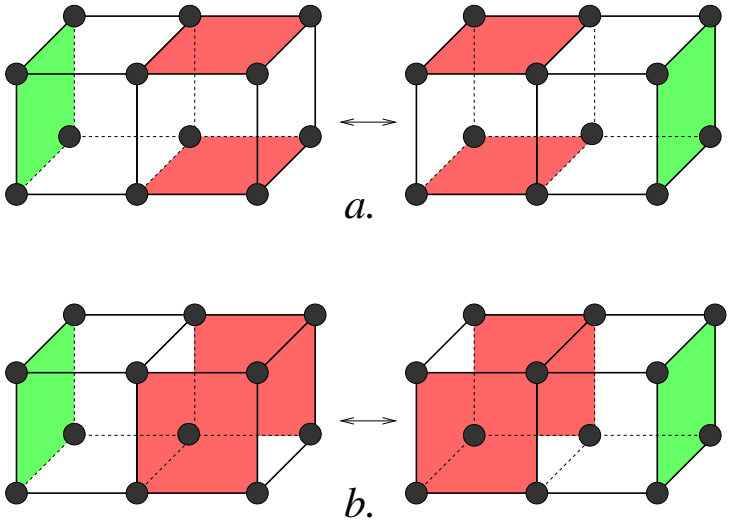

Figure 4.3: A local update which consists of a 'shift' exchange of a plate and a cube consisting of two adjacent squares.

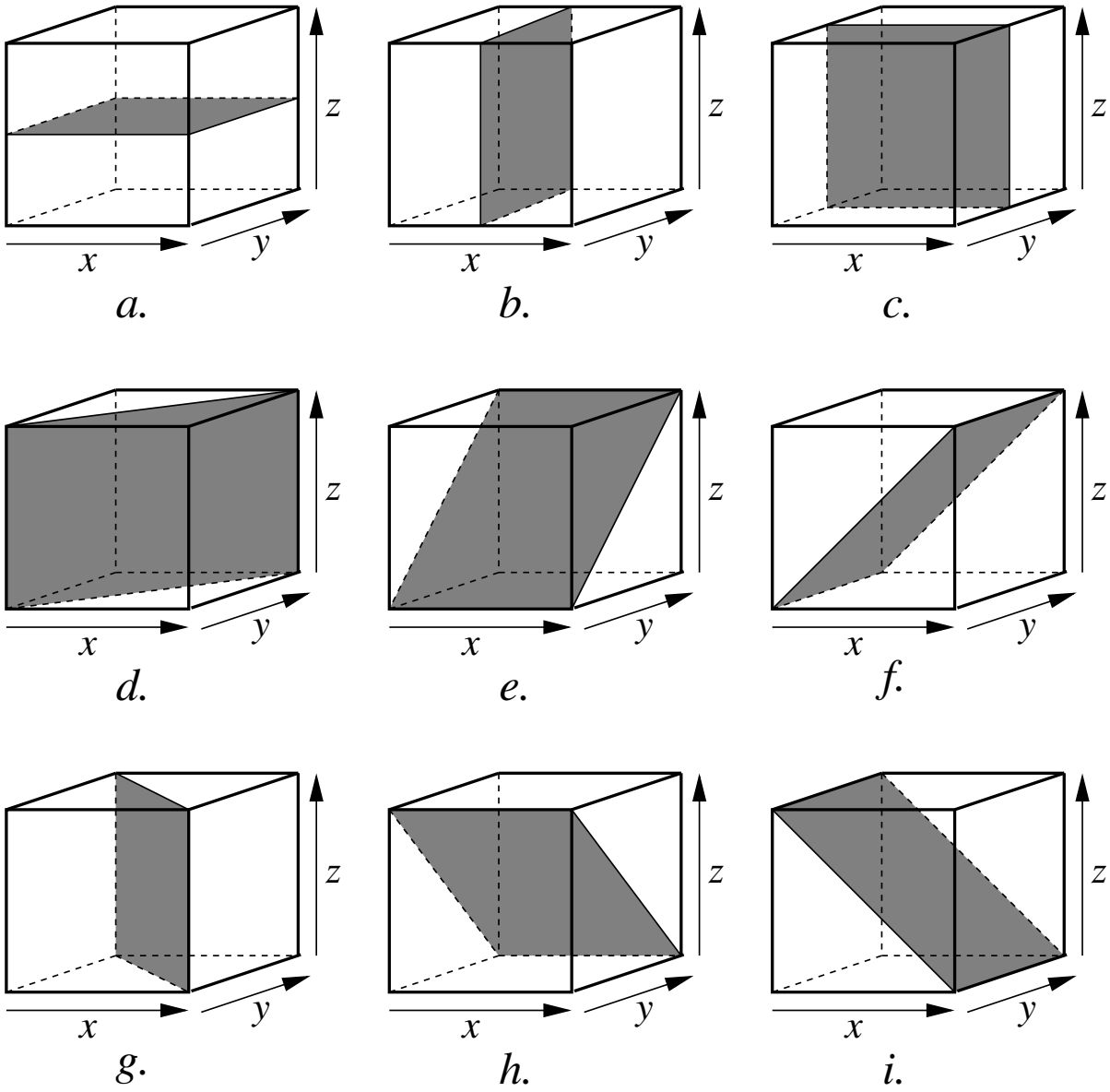

Figure 4.4: All the above nine are symmetry planes of the cubic lattice and are allowed at the isotropic point when the fugacities of all the three types of squares are equal. When we vary the fugacity of the z-type plate, a z-type plate can not be reflected into an x or y-type plate. Thus the symmetry planes in e, f, h and i are not allowed in this anisotropic scenario.

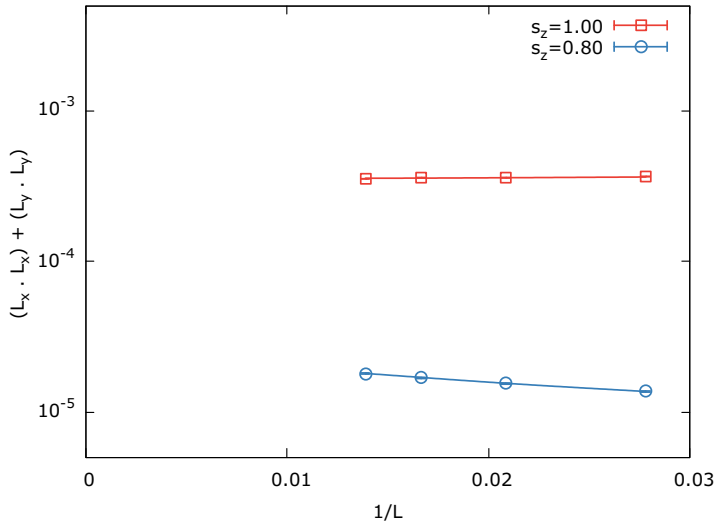

Figure 4.5: The layering order parameter $(L_x \cdot L_x) + (L_y \cdot L_y)$ as a function of inverse system size $1/L$ for values of z plate fugacites, $s_z = 1.0, 0.8$. The fact that $(L_x \cdot L_x) + (L_y \cdot L_y)$ goes to a non-zero value in the thermodynamic limit shows that the system is not in a layered phase but in the sublattice phase at these values of s_z.

in the introduction which updates a macroscopic number of squares at each move. We generalised the pocket cluster algorithm to the 3d case of anisotropic squares. One move of the pocket cluster algorithm can be described in short as follows: A random square p is picked as a seed and removed from the lattice A and placed in a pocket P which is an empty lattice in the beginning. The seed square p is then taken from the pocket, reflected about a randomly chosen symmetry plane S of the system and placed back on the original lattice A. All the other squares which now overlap with p on A are removed and placed on P. Again, a square p' on P is chosen, reflected about S and placed on A. This procedure is repeated till P is empty. We finally end up with a cluster update on A. The only care needed to be taken in case of anisotropic systems is that the symmetries of the system about which one can reflect the squares reduces. In our case since z-squares have a different fugacity compared to x and y squares, any symmetry cut which reflects a z-square into an x or y square is not allowed. Fig. 4.4 shows the possible symmetry planes of the system which can be used to define the pocket cluster update for an isotropic system. Planes e, f, h, i are not allowed incase of z-square anisotropy.

4.3 Results

We define a layering order vector $\vec{L}$ as follows:

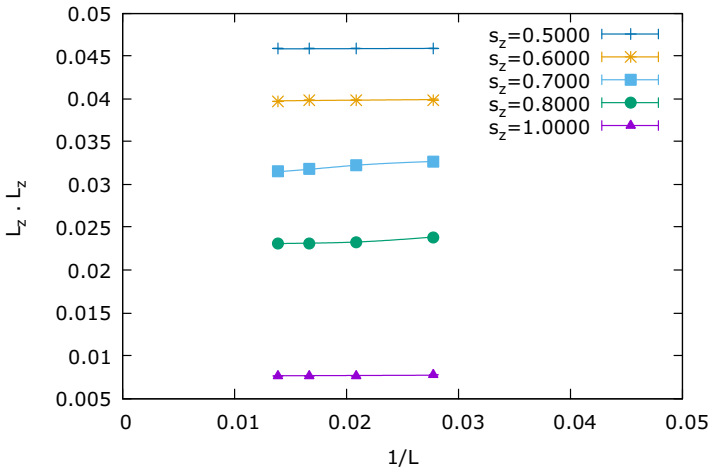

Figure 4.6: The layering order parameter $L_z \cdot L_z$ as a function of inverse system size $1/L$ for various values of z plate fugacites, ($s_z = 1, 0.8, 0.7, 0.6, 0.5$). The order parameter goes to a non-zero value in the thermodynamic limit for the whole range of s_z. This coupled with the fact that that x and y layering order parameters go to 0 for $s_z < 0.60(5)$ indicate that for $s_z < 0.60(5)$ the system is layered in the z-direction and for $s_z > 0.60(5)$ the system is sublattice ordered.

$$L_x = \sum_{x,y,z} (-1)^x (N_x + N_y + N_z)/L^3 \tag{4.2}$$

$$L_y = \sum_{x,y,z} (-1)^y (N_x + N_y + N_z)/L^3 \tag{4.3}$$

$$L_z = \sum_{x,y,z} (-1)^z (N_x + N_y + N_z)/L^3 \tag{4.4}$$

$$\tag{4.5}$$

At the isotropic point ($s_z = 1$) we find that all three components of the layering order vector go to a non-zero value in the thermodynamic limit. Fig.4.5 shows the order parameter constructed from the x and y components of the layering order vector and Fig.4.6 shows the order parameter constructed from the z component of the layering order vector. At $s_z = 1$, both can be seen going to a constant non-zero value as a function of $1/L$.

Now we systematically decrease s_z, making the system anisotropic in the z direction.

Fig.4.8 shows the order parameter constructed from the x and y components of the layering order vector. As s_z is decreased it can be seen that the order parameter goes from a constant value in the thermodynamic limit to a disordered decay. The order parameter constructed from the z component on the other hand remains a constant as a function of $1/L$ for all values of s_z with the magnitude of the order parameter increasing as we decrease s_z.

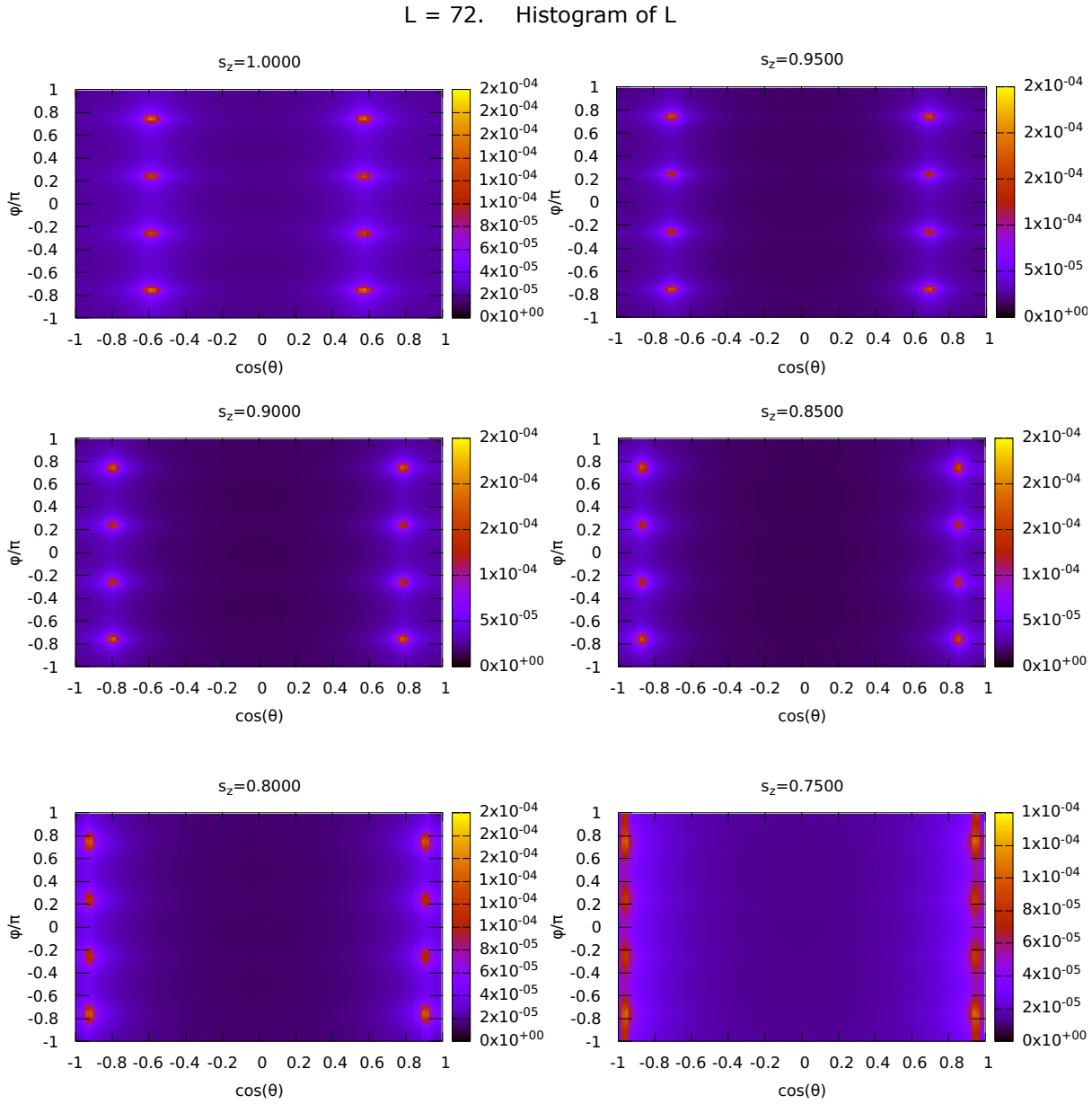

Figure 4.7: Joint histogram of the single plate layering order vector L in (ϕ, θ) coordinate space at four values of z plate fugacities: $s_z = 1, 0.9, 0.8, 0.7$. The continuous shifting of peaks as we decrease s_z away from isotropy suggests a continuous transition. As we decrease s_z, ϕ of the eight peaks remain constant, while θ shift continuously from $(-)\frac{1}{\sqrt{3}}$ to (-)1. The four peaks in the northern (southern) hemisphere, close up continuously into the north(south) pole and in the layered phase we see peaks only in the north and south poles.

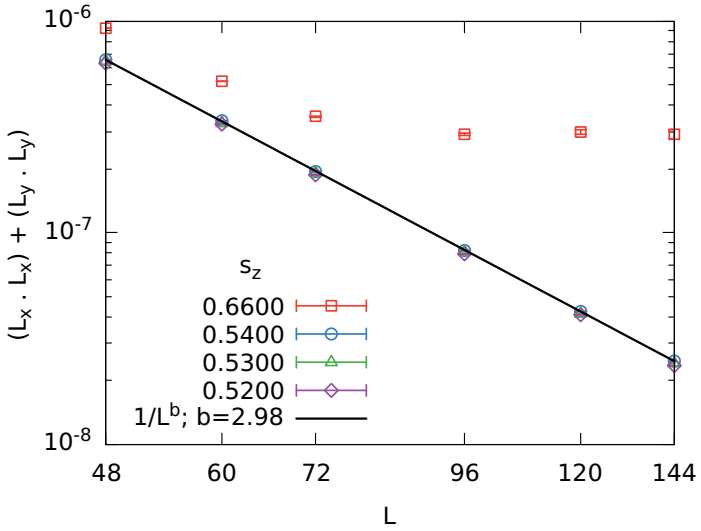

Figure 4.8: The layering order parameter $(L_x \cdot L_x) + (L_y \cdot L_y)$ as a function of system size L for various values of z plate fugacites, across the transition. At $s_z = 0.66$, the order parameter clearly goes to a constant value. At $s_z = 0.54$, it decays as $\sim 1/L^3$, indicative of a layered phase.

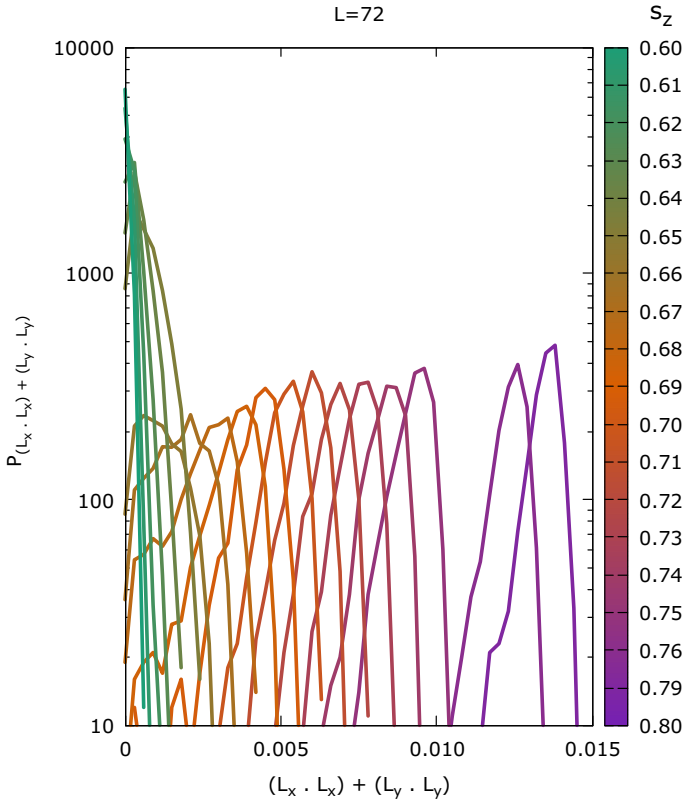

Figure 4.9: Histogram of the single plate layer order parameter $(L_x \cdot L_x) + (L_y \cdot L_y)$ for various values of s_z. The peaks shift continuously away from 0 as we increase s_z, from the layerd phase into the sublattice phase.

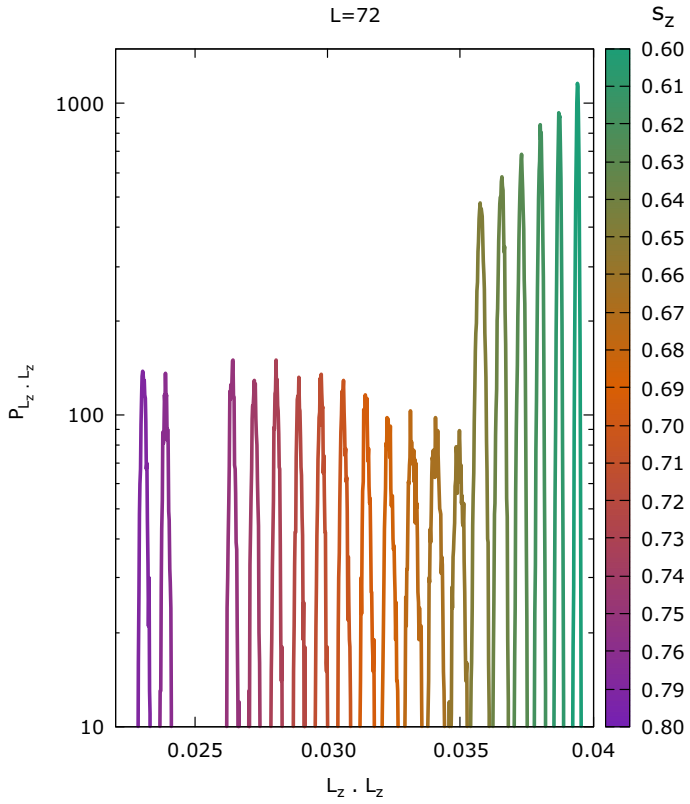

Figure 4.10: Histogram of the single plate layer order parameter $L_z \cdot L_z$ for various values of s_z. The peaks shift continuously towards 0 as we increase s_z, from the layered phase into the sublattice phase.

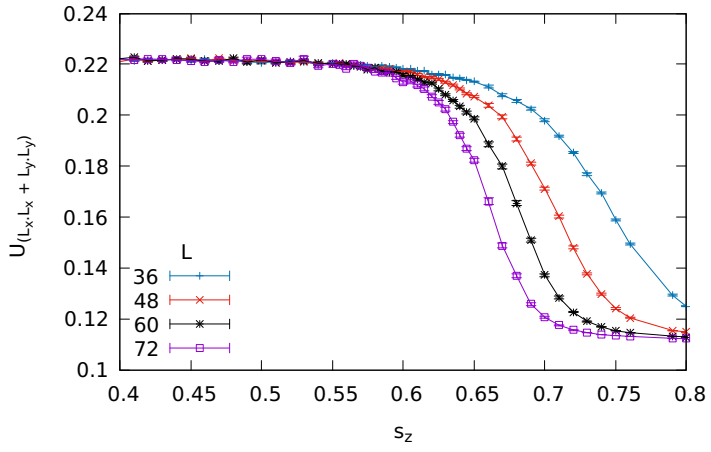

Figure 4.11: Binder cumulants of the single plate columnar order parameter $(L_x \cdot L_x) + (L_y \cdot L_y)$ as a function of s_z for four values of system sizes, L. At $s_z \sim 0.62$ the binders cumulants for various system sizes start sticking indicating a transition from an ordered into a power-law behaviour of the order parameter.

To further study the nature of the transition, we look at the histogram of the direction of the layering order vector in the (ϕ, θ) plane in Fig.4.7. As we decrease s_z systematically, we find that the ϕ of the peaks remain constant. $cos(\theta)$ on the other hand, shifts continuously from $(-)\frac{1}{\sqrt{3}}$ to $(-)1$ as we decrease s_z from 1 to 0.75. This is consistent with the fact that the order parameter constructed from the x and y components decrease in magnitude and the z component order parameter increases in magnitude as we decrease s_z. The continuous shifting of peaks away from the isotropic point also suggests a continuous transition.

Fig.4.9 and Fig.4.10 show the histograms of the order parameters constructed from the x, y and z components respectively. Continuous shifting of peaks in the histogram as a function of increasing s_z suggests a continuous transition. Fig.4.11 also shows the binder cumulant constructed from the x, y component order parameter. As we decrease s_z, the binders start sticking a $s_z \sim 0.6$ which is an artifact of the fact that the x, y component order parameter goes from a constant to a power-law as a function of system size, L.

We conclude that at $s_z = 0.60(5)$, the system goes from an ordered state into a layered state, with layering in the z direction.

4.4 Summary

We have studied the model of hard-squares on a cubic lattice at full packing with anisotropy in the fugacity of z-normal plates. At the isotropic point $s_z = 1$, we find that the system supports long range columnar order. In the fully anisotropic limit of $s_z = 0$, we find that the system is in a layered phase. We find a transition from the layered phase to the columnar ordered phase at a non-zero s_z, across which the layered order parameter is continuous. Although we do not yet have a theory for this transition, we can make some useful observations for future work. The Binder cumulant of the layering order parameter sticks in the layered phase and splays in the columnar ordered phase. This is similar to the sticking and splaying of binder cumulant across a 2d KT transition. We observe KT behaviour in a 3d system. This could be an artefact of the fact that in the layered phase, the system acts as decoupled 2d layers. It has been shown that thin films of a 3d XY model supports KT physics[117]. It will be very interesting to explore this connection further.

Chapter 5

Conclusion and Outlook

In Chapter.1 we presented a overview of simple theoretical models which can be used to study the wide range of magnetic phenomena in nature. We also further explored the nature of interaction that drive magnetic transitions. We also eloberated on purely entropic transitions. We then gave a short summary of numerical Monte-Carlo techniques we use to solve the problems posed in this thesis. In Chapter.2, we presented and tested a simple statistical model for the distribution of lengths of worms constructed by worm algorithms used in Monte Carlo simulations of frustrated triangular and kagome lattice Ising antiferromagnets, focusing on the behaviour in the critical phase associated with the two-step melting of three-sublattice order in these systems. These worm algorithms work by creating a defect-antidefect pair and propagating the antidefect while keeping the defect fixed. The worm construction ends when the antidefect returns to the starting site and annihilates the defect. To model the distribution of worm lengths in the critical (power-law three-sublattice ordered) phase, we use an analogy with a random walker in a *logarithmic* central potential whose strength is set by the *power-law form* of the equilibrium defect-antidefect correlation function. The return time distribution of such a random walk in a logarithmic potential is known to follow a power-law behaviour, which provides us a prediction for the distribution of lengths of the worms in this critical regime. This prediction depends only on the long-distance properties of the system in equilibrium, and is therefore independent of details of the algorithm and model Hamiltonian. We find that measured power-law exponents for the worm-length distribution are in reasonably good agreement with this prediction for two different worm algorithm protocols independent of the lattice (kagome or triangular) and the detailed form of the model Hamiltonian. This provides a rationale for the approximately universal behaviour of autocorrelation exponents noted in earlier work on these worm algorithms. Clearly, a similar heuristic picture for the worm-length distribution is possible in other applications of worm algorithms to two-dimensional critical points/phases, and it would be interesting to ask how well the analogs of Eq.(1.44) do in these cases. In the opposite direction, the readily discernible deviations of the

measured values of θ from the prediction of the simple random walk model underscore the importance of incorporating the back-reaction of worm motion on the underlying dimer configuration, rather than thinking in terms of a fixed static potential provided by the dimer configuration. We leave this as an interesting direction for future work.

In Chapter.3 we performed Monte Carlo simulations using recently developed cluster algorithms for frustrated lattices [49] to study the phase diagram of a triangular lattice Ising antiferromagnet with ferromagnetic next-nearest and next-next-nearest interactions. In the presence of ferromagnetic next-nearest neighbor couplings, the spins form a three-sublattice ordered $(\sqrt{3} \times \sqrt{3})$ state at low temperatures which is known to melt via a two-step melting process with an intermediate power-law three-sublattice ordered phase characterized by a temperature dependent exponent $\eta(T) \in \left(\frac{1}{9}, \frac{1}{4}\right)$[103, 105, 47]. We studied the effect of increasing ferromagnetic next-next-nearest neighbor interactions on the nature of this melting transition. We find that the two-step melting pinches off into an anomalous effective critical transition line characterized by scale invariant behavior of the correlation functions and anomalous binder cumulant behavior before finally resolving into a first order transition which separates the ferrimagnetic three-sublattice ordered state and a paramagnet. We numerically investigate this anomalous effective critical line and obtain estimates for the location of a multicritical point $\mathcal{M}_c$ with exponents which are shown to match within errorbars with the values for the Z_6 self-dual parafermionic conformal field theory constructed by Zamolodchikov and Fateev [98]. We also demonstrate that the same exponents govern the behavior of the corresponding pinch-off point of the two-step melt of the six-fold symmetric ground state in the six-state clock model studied by J. Cardy [96]. Our results on the clock model provide strong evidence in favor of a conjecture of Dorey et. al. identifying this pinch-off point with the Z_6 parafermionic conformal field theory [97]. We compare the binder cumulant behavior of the three-sublattice order parameter and the ferromagnetic order parameter near the estimated multicritical point of both the models and find similarities which helps us in pin-pointing the location of the multi-critical point on the triangular lattice phase diagram. In further work we would also like to study the phase diagram of the Ising antiferromagnet on the Kagome lattice with next-nearest and next-next nearest neighbor interactions. The ground states stabilized by these interactions on the Kagome lattice are similar to the ones on the triangular lattice. It would be interesting to know the properties of the multi-critical point and if it also falls in the same universality class.

In Chapter.4 We numerically investigate a lattice gas of hard squares at full packing on a cubic lattice with fugacities z_x, z_y and z_z of the three differently oriented squares as control parameters using local and cluster Monte Carlo updates. At the isotropic point, we find that the system is in an sublattice ordered state. As we decrease the fugacity of one orientation of squares while keeping the other two fixed, we observe a transition

from the columnar ordered state to a bi-layered phase. In future work, we would like to further explore this bi-layered phase by thinking of it as a problem of a mixture of hard squares and dimers on a square lattice. This will shed more insight into the KT like transition that we observe in this 3d system.

In conclusion we have explored two models, one where energetic interactions drives the physics and the other where entropic considerations drives the physics. For the first case we developed two sophisticated Monte-Carlo worm algorithms whose statistics we were able to map to a random walker in a logarithmic field. We then proceed to numerically investigate the model and show the presence of a multicritical point in the Z_6 universality class. To our knowledge, this is the first numerical confirmation of a non-trivial multicritical point in a microscopic model and was made possible because of the exceptional performance of the worm algorithms that we developed. In the second case, we generalised a previously proposed pocket cluster algorithm for 2d dimer models to a 3d hard-square model. In this model we observe 2d KT physics in a 3d model. To our knowledge this has not been seen before and opens up many possibilities to observe KT physics in such models. The ideas and methods used in the development of the algorithms and in the numerical analysis of the models will be very useful for further numerical studies of exotic models with many competing interactions.

Bibliography

[1] L. Onsager, "Crystal statistics. i. a two-dimensional model with an order-disorder transition," *Physical Review*, vol. 65, no. 3-4, pp. 117–149, 1944.

[2] L. Onsager, "The effects of shape on the interaction of colloidal particles," *Annals of the New York Academy of Sciences*, vol. 51, no. 4, pp. 627–659, 1949.

[3] D. P. Landau and K. Binder, *A guide to Monte Carlo simulations in statistical physics*. Cambridge university press, 2014.

[4] E. Fradkin, *Field Theories of Condensed Matter Physics*. Cambridge University Press, 2013.

[5] A. Auerbach, *Interacting electrons and quantum magnetism*. Springer Science & Business Media, 2012.

[6] N. W. Ashcroft, N. D. Mermin, *et al.*, "Solid state physics [by] neil w. ashcroft [and] n. david mermin.," 1976.

[7] D. C. Mattis, *The theory of magnetism made simple: an introduction to physical concepts and to some useful mathematical methods*. World Scientific Publishing Company, 2006.

[8] D. Breed, K. Gilijamse, and A. Miedema, "Magnetic properties of k2cof4 and rb2cof4; two-dimensional ising antiferromagnets," *Physica*, vol. 45, no. 2, pp. 205–216, 1969.

[9] E. Ising, "Beitrag zur theorie des ferromagnetismus," *Zeitschrift für Physik A Hadrons and Nuclei*, vol. 31, no. 1, pp. 253–258, 1925.

[10] M. Hutchings, J. Als-Nielsen, P. Lindgard, and P. Walker, "Neutron scattering investigation of the temperature dependence of long-wavelength spin waves in ferromagnetic rb2crcl4," *Journal of Physics C: Solid State Physics*, vol. 14, no. 34, p. 5327, 1981.

[11] R. Peierls, "On ising's model of ferromagnetism," in *Mathematical Proceedings of the Cambridge Philosophical Society*, vol. 32, pp. 477–481, Cambridge University Press, 1936.

[12] H.-O. Heuer, "Critical dynamics of the three-dimensional ising model: A monte carlo study," *Journal of statistical physics*, vol. 72, no. 3-4, pp. 789–827, 1993.

[13] J. Zinn-Justin, *Quantum field theory and critical phenomena*. Clarendon Press, 1996.

[14] N. D. Mermin and H. Wagner, "Absence of ferromagnetism or antiferromagnetism in one-or two-dimensional isotropic heisenberg models," *Physical Review Letters*, vol. 17, no. 22, p. 1133, 1966.

[15] J. M. Kosterlitz and D. J. Thouless, "Ordering, metastability and phase transitions in two-dimensional systems," *Journal of Physics C: Solid State Physics*, vol. 6, no. 7, p. 1181, 1973.

[16] Néel, M. Louis, "Propriétés magnétiques des ferrites ; ferrimagnétisme et antiferromagnétisme," *Ann. Phys.*, vol. 12, no. 3, pp. 137–198, 1948.

[17] G. Wannier, "Antiferromagnetism. the triangular ising net," *Physical Review*, vol. 79, no. 2, p. 357, 1950.

[18] A. P. Ramirez, A. Hayashi, R. a. Cava, R. Siddharthan, and B. Shastry, "Zero-point entropy in spin ice," *Nature*, vol. 399, no. 6734, p. 333, 1999.

[19] C. Castelnovo, R. Moessner, and S. L. Sondhi, "Magnetic monopoles in spin ice," *Nature*, vol. 451, no. 7174, p. 42, 2008.

[20] M. Harris, S. Bramwell, D. McMorrow, T. Zeiske, and K. Godfrey, "Geometrical frustration in the ferromagnetic pyrochlore ho 2 ti 2 o 7," *Physical Review Letters*, vol. 79, no. 13, p. 2554, 1997.

[21] A. Olariu, P. Mendels, F. Bert, F. Duc, J. Trombe, M. De Vries, and A. Harrison, "O 17 nmr study of the intrinsic magnetic susceptibility and spin dynamics of the quantum kagome antiferromagnet zncu 3 (oh) 6 cl 2," *Physical review letters*, vol. 100, no. 8, p. 087202, 2008.

[22] M. Wolf and K. Schotte, "Ising model with competing next-nearest-neighbour interactions on the Kagome lattice," *Journal of Physics A: Mathematical and General*, vol. 21, no. 9, p. 2195, 1988.

[23] T. Fennell, S. Bramwell, D. McMorrow, P. Manuel, and A. Wildes, "Pinch points and kasteleyn transitions in kagome ice," *Nature Physics*, vol. 3, no. 8, p. 566, 2007.

[24] J. E. Greedan, "Geometrically frustrated magnetic materialsbasis of a presentation given at materials discussion no. 3, 26–29 september, 2000, university of cambridge, uk.," *Journal of Materials Chemistry*, vol. 11, no. 1, pp. 37–53, 2001.

[25] S. Bramwell, S. Carling, C. Harding, K. Harris, B. Kariuki, L. Nixon, and I. Parkin, "The anhydrous alums as model triangular-lattice magnets," *Journal of Physics: Condensed Matter*, vol. 8, no. 9, p. L123, 1996.

[26] H. Serrano-González, S. Bramwell, K. Harris, B. Kariuki, L. Nixon, I. Parkin, and C. Ritter, "Magnetic structures of the triangular lattice magnets $afe(so_4)_2$ $(a = k, rb, cs)$," *Journal of applied physics*, vol. 83, no. 11, pp. 6314–6316, 1998.

[27] M. Townsend, G. Longworth, and E. Roudaut, "Triangular-spin, kagome plane in jarosites," *Physical Review B*, vol. 33, no. 7, p. 4919, 1986.

[28] A. S. Wills and A. Harrison, "Structure and magnetism of hydronium jarosite, a model kagome antiferromagnet," *Journal of the Chemical Society, Faraday Transactions*, vol. 92, no. 12, pp. 2161–2166, 1996.

[29] M. R. Norman, "Colloquium: Herbertsmithite and the search for the quantum spin liquid," *Rev. Mod. Phys.*, vol. 88, p. 041002, Dec 2016.

[30] B. Fåk, E. Kermarrec, L. Messio, B. Bernu, C. Lhuillier, F. Bert, P. Mendels, B. Koteswararao, F. Bouquet, J. Ollivier, A. D. Hillier, A. Amato, R. H. Colman, and A. S. Wills, "Kapellasite: A kagome quantum spin liquid with competing interactions," *Phys. Rev. Lett.*, vol. 109, p. 037208, Jul 2012.

[31] J. Reimers, A. Berlinsky, and A.-C. Shi, "Mean-field approach to magnetic ordering in highly frustrated pyrochlores," *Physical Review B*, vol. 43, no. 1, p. 865, 1991.

[32] R. Moessner and J. Chalker, "Properties of a classical spin liquid: the heisenberg pyrochlore antiferromagnet," *Physical review letters*, vol. 80, no. 13, p. 2929, 1998.

[33] W. Schiessl, W. Potzel, H. Karzel, M. Steiner, G. Kalvius, A. Martin, M. Krause, I. Halevy, J. Gal, W. Schäfer, *et al.*, "Magnetic properties of the zn fe 2 o 4 spinel," *Physical Review B*, vol. 53, no. 14, p. 9143, 1996.

[34] A. Wills, N. Raju, and J. Greedan, "Low-temperature structure and magnetic properties of the spinel limn2o4: A frustrated antiferromagnet and cathode material," *Chemistry of materials*, vol. 11, no. 6, pp. 1510–1518, 1999.

[35] S.-H. Lee, C. Broholm, G. Aeppli, T. Perring, B. Hessen, and A. Taylor, "Isolated spin pairs and two-dimensional magnetism in srcr 9 p ga 1 2- 9 p o 19," *Physical review letters*, vol. 76, no. 23, p. 4424, 1996.

[36] A. Ramirez, "Strongly geometrically frustrated magnets," *Annual Review of Materials Science*, vol. 24, no. 1, pp. 453–480, 1994.

[37] J. N. Reimers, J. Dahn, J. Greedan, C. Stager, G. Liu, I. Davidson, and U. Von Sacken, "Spin glass behavior in the frustrated antiferromagnetic linio2," *Journal of Solid State Chemistry*, vol. 102, no. 2, pp. 542–552, 1993.

[38] Y. Kitaoka, T. Kobayashi, A. Kōda, H. Wakabayashi, Y. Niino, H. Yamakage, S. Taguchi, K. Amaya, K. Yamaura, M. Takano, *et al.*, "Orbital frustration and resonating valence bond state in the spin-1/2 triangular lattice linio 2," *Journal of the Physical Society of Japan*, vol. 67, no. 11, pp. 3703–3706, 1998.

[39] Y. Han, Y. Shokef, A. M. Alsayed, P. Yunker, T. C. Lubensky, and A. G. Yodh, "Geometric frustration in buckled colloidal monolayers," *Nature*, vol. 456, no. 7224, p. 898, 2008.

[40] Y. Li, G. Chen, W. Tong, L. Pi, J. Liu, Z. Yang, X. Wang, and Q. Zhang, "Rare-earth triangular lattice spin liquid: A single-crystal study of $\mathrm{ybmggao_4}$," *Phys. Rev. Lett.*, vol. 115, p. 167203, Oct 2015.

[41] Y. Li, S. Bachus, Y. Tokiwa, A. A. Tsirlin, and P. Gegenwart, "Absence of zero-point entropy in a triangular ising antiferromagnet," *arXiv preprint arXiv:1804.00696*, 2018.

[42] Y. Tanaka and N. Uryû, "Ground state spin configurations of the triangular ising net with the first, second and third nearest neighbor interactions," *Progress of Theoretical Physics*, vol. 55, no. 5, pp. 1356–1372, 1976.

[43] J. Stephenson, "Ising-model spin correlations on the triangular lattice," *Journal of Mathematical Physics*, vol. 5, no. 8, pp. 1009–1024, 1964.

[44] B. Metcalf, "Ground state spin orderings of the triangular ising model with the nearest and next nearest neighbor interaction," *Physics Letters A*, vol. 46, no. 5, pp. 325–326, 1974.

[45] S. Alexander, "Lattice gas transition of he on grafoil. a continuous transition with cubic terms," *Physics Letters A*, vol. 54, no. 5, pp. 353 – 354, 1975.

[46] A. Berker, S. Ostlund, and F. Putnam, "Renormalization-group treatment of a Potts lattice gas for krypton adsorbed onto graphite," *Phys. Rev. B*, vol. 17, pp. 3650–3665, May 1978.

[47] D. Landau, "Critical and multicritical behavior in a triangular-lattice-gas ising model: Repulsive nearest-neighbor and attractive next-nearest-neighbor coupling," *Physical Review B*, vol. 27, no. 9, p. 5604, 1983.

[48] S. Korshunov, "Nature of phase transitions in the striped phase of a triangular-lattice ising antiferromagnet," *Physical Review B*, vol. 72, no. 14, p. 144417, 2005.

[49] G. Rakala and K. Damle, "Cluster algorithms for frustrated two-dimensional Ising antiferromagnets via dual worm constructions," *Phys. Rev. E*, vol. 96, p. 023304, Aug 2017.

[50] P. W. Kasteleyn, "The statistics of dimers on a lattice: I. the number of dimer arrangements on a quadratic lattice," *Physica*, vol. 27, no. 12, pp. 1209–1225, 1961.

[51] M. E. Fisher, "On the dimer solution of planar ising models," *Journal of Mathematical Physics*, vol. 7, no. 10, pp. 1776–1781, 1966.

[52] R. Mössner and S. Sondhi, "Ising and dimer models in two and three dimensions," *Physical Review B*, vol. 68, no. 5, p. 054405, 2003.

[53] D. A. Huse, W. Krauth, R. Moessner, and S. Sondhi, "Coulomb and liquid dimer models in three dimensions," *Physical review letters*, vol. 91, no. 16, p. 167004, 2003.

[54] A. Verberkmoes and B. Nienhuis, "Triangular trimers on the triangular lattice: An exact solution," *Physical review letters*, vol. 83, no. 20, p. 3986, 1999.

[55] A. Ghosh, D. Dhar, and J. L. Jacobsen, "Random trimer tilings," *Physical Review E*, vol. 75, no. 1, p. 011115, 2007.

[56] D. S. Gaunt and M. E. Fisher, "Hard-sphere lattice gases. i. plane-square lattice," *The Journal of Chemical Physics*, vol. 43, no. 8, pp. 2840–2863, 1965.

[57] A. Bellemans and R. Nigam, "Phase transitions in two-dimensional lattice gases of hard-square molecules," *The Journal of Chemical Physics*, vol. 46, no. 8, pp. 2922–2935, 1967.

[58] H. Meirovitch, "A monte carlo study of the entropy, the pressure, and the critical behavior of the hard-square lattice gas," *Journal of Statistical Physics*, vol. 30, no. 3, pp. 681–698, 1983.

[59] P. A. Pearce and K. A. Seaton, "A classical theory of hard squares," *Journal of statistical physics*, vol. 53, no. 5-6, pp. 1061–1072, 1988.

[60] T. M. Haas, "A numerical study of the phase structure of the q-state generalization of the hard-square model," *Journal of statistical physics*, vol. 54, no. 1-2, pp. 201–219, 1989.

[61] A. Baram and M. Fixman, "Hard square lattice gas," *The Journal of chemical physics*, vol. 101, no. 4, pp. 3172–3178, 1994.

[62] K. Ramola and D. Dhar, "High-activity perturbation expansion for the hard square lattice gas," *Physical Review E*, vol. 86, no. 3, p. 031135, 2012.

[63] R. J. Baxter, "Hard hexagons: exact solution," *Journal of Physics A: Mathematical and General*, vol. 13, no. 3, p. L61, 1980.

[64] J. Kundu, R. Rajesh, D. Dhar, and J. F. Stilck, "Nematic-disordered phase transition in systems of long rigid rods on two-dimensional lattices," *Physical Review E*, vol. 87, no. 3, p. 032103, 2013.

[65] T. Nath, J. Kundu, and R. Rajesh, "High-activity expansion for the columnar phase of the hard rectangle gas," *Journal of Statistical Physics*, vol. 160, no. 5, pp. 1173–1197, 2015.

[66] K. Ramola, K. Damle, and D. Dhar, "Columnar order and ashkin-teller criticality in mixtures of hard squares and dimers," *Physical review letters*, vol. 114, no. 19, p. 190601, 2015.

[67] J. Bouttier, P. Di Francesco, and E. Guitter, "Critical and tricritical hard objects on bicolourable random lattices: exact solutions," *Journal of Physics A: Mathematical and General*, vol. 35, no. 17, p. 3821, 2002.

[68] M. Assis, J. Jacobsen, I. Jensen, J. Maillard, and B. McCoy, "Integrability versus non-integrability: hard hexagons and hard squares compared," *Journal of Physics A: Mathematical and Theoretical*, vol. 47, no. 44, p. 445001, 2014.

[69] W. K. Hastings, "Monte carlo sampling methods using markov chains and their applications," 1970.

[70] U. Wolff, "Collective Monte-Carlo Updating for Spin Systems," *Phys. Rev. Lett.*, vol. 62, pp. 361–364, Jan 1989.

[71] R. H. Swendsen and J.-S. Wang, "Nonuniversal critical dynamics in monte carlo simulations," *Physical review letters*, vol. 58, no. 2, p. 86, 1987.

[72] H. G. Evertz, "The loop algorithm," *Advances in Physics*, vol. 52, no. 1, pp. 1–66, 2003.

[73] N. Prokof'ev and B. Svistunov, "Worm algorithms for classical statistical models," *Physical review letters*, vol. 87, no. 16, p. 160601, 2001.

[74] F. Alet and E. S. Sørensen, "Directed geometrical worm algorithm applied to the quantum rotor model," *Physical Review E*, vol. 68, no. 2, p. 026702, 2003.

[75] F. Alet and E. S. Sørensen, "Directed geometrical worm algorithm applied to the quantum rotor model," *Physical Review E*, vol. 68, no. 2, p. 026702, 2003.

[76] M. Wallin, E. S. So, S. Girvin, A. Young, *et al.*, "Superconductor-insulator transition in two-dimensional dirty boson systems," *Physical Review B*, vol. 49, no. 17, p. 12115, 1994.

[77] M. Suzuki, "Relationship between d-dimensional quantal spin systems and (d+ 1)-dimensional ising systems: Equivalence, critical exponents and systematic approximants of the partition function and spin correlations," *Progress of theoretical physics*, vol. 56, no. 5, pp. 1454–1469, 1976.

[78] J. E. Hirsch, R. L. Sugar, D. J. Scalapino, and R. Blankenbecler, "Monte carlo simulations of one-dimensional fermion systems," *Physical Review B*, vol. 26, no. 9, p. 5033, 1982.

[79] A. W. Sandvik, "Stochastic series expansion method with operator-loop update," *Physical Review B*, vol. 59, no. 22, p. R14157, 1999.

[80] A. Dorneich and M. Troyer, "Accessing the dynamics of large many-particle systems using the stochastic series expansion," *Physical Review E*, vol. 64, no. 6, p. 066701, 2001.

[81] P. Hitchcock, E. S. Sørensen, and F. Alet, "Dual geometric worm algorithm for two-dimensional discrete classical lattice models," *Physical Review E*, vol. 70, no. 1, p. 016702, 2004.

[82] P. W. Leung and C. L. Henley, "Percolation properties of the wolff clusters in planar triangular spin models," *Physical Review B*, vol. 43, no. 1, p. 752, 1991.

[83] F. Alet, Y. Ikhlef, J. L. Jacobsen, G. Misguich, and V. Pasquier, "Classical dimers with aligning interactions on the square lattice," *Physical Review E*, vol. 74, no. 4, p. 041124, 2006.

[84] A. W. Sandvik and R. Moessner, "Correlations and confinement in nonplanar two-dimensional dimer models," *Physical Review B*, vol. 73, no. 14, p. 144504, 2006.

[85] W. Janke, T. Neuhaus, and A. M. Schakel, "Critical loop gases and the worm algorithm," *Nuclear Physics B*, vol. 829, no. 3, pp. 573–599, 2010.

[86] W. Janke and A. M. Schakel, "Fractal structure of spin clusters and domain walls in the two-dimensional ising model," *Physical Review E*, vol. 71, no. 3, p. 036703, 2005.

[87] A. Stella and C. Vanderzande, "Scaling and fractal dimension of ising clusters at the d= 2 critical point," *Physical review letters*, vol. 62, no. 10, p. 1067, 1989.

[88] H. Saleur and B. Duplantier, "Exact determination of the percolation hull exponent in two dimensions," *Physical review letters*, vol. 58, no. 22, p. 2325, 1987.

[89] H. E. Stanley, "Cluster shapes at the percolation threshold: and effective cluster dimensionality and its connection with critical-point exponents," *Journal of Physics A: Mathematical and General*, vol. 10, no. 11, p. L211, 1977.

[90] C. Vanderzande and A. Stella, "Bulk, surface and hull fractal dimension of critical ising clusters in d= 2," *Journal of Physics A: Mathematical and General*, vol. 22, no. 10, p. L445, 1989.

[91] B. Duplantier, "Conformally invariant fractals and potential theory," *Physical review letters*, vol. 84, no. 7, p. 1363, 2000.

[92] D. Kandel, R. Ben-Av, and E. Domany, "Cluster dynamics for fully frustrated systems," *Physical review letters*, vol. 65, no. 8, p. 941, 1990.

[93] G. Franzese, "Cluster analysis for percolation on a two-dimensional fully frustrated system," *Journal of Physics A: Mathematical and General*, vol. 29, no. 23, p. 7367, 1996.

[94] L. Jaubert, M. Haque, and R. Moessner, "Analysis of a fully packed loop model arising in a magnetic coulomb phase," *Physical review letters*, vol. 107, no. 17, p. 177202, 2011.

[95] W. Krauth and R. Moessner, "Pocket monte carlo algorithm for classical doped dimer models," *Physical Review B*, vol. 67, no. 6, p. 064503, 2003.

[96] J. L. Cardy, "General discrete planar models in two dimensions: Duality properties and phase diagrams," *Journal of Physics A: Mathematical and General*, vol. 13, no. 4, p. 1507, 1980.

[97] P. Dorey, P. Provero, R. Tateo, and S. Vinti, "On the phase diagram of the discrete z6 spin models," *Journal of Physics A: Mathematical and General*, vol. 32, no. 13, p. L151, 1999.

[98] A. Zamolodchikov and V. Fateev, "Nonlocal (parafermion) currents in two-dimensional conformal quantum field theory and self-dual critical points in zn-symmetric statistical systems," *Sov. Phys. JETP*, vol. 62, no. 2, pp. 215–225, 1985.

[99] K. Kano and S. Naya, "Antiferromagnetism. the kagomé ising net," *Progress of theoretical physics*, vol. 10, no. 2, pp. 158–172, 1953.

[100] H. Blote and H. Hilborst, "Roughening transitions and the zero-temperature triangular ising antiferromagnet," *Journal of Physics A: Mathematical and General*, vol. 15, no. 11, p. L631, 1982.

[101] B. Nienhuis, H. J. Hilhorst, and H. Blote, "Triangular sos models and cubic-crystal shapes," *Journal of Physics A: Mathematical and General*, vol. 17, no. 18, p. 3559, 1984.

[102] S. Papanikolaou, E. Luijten, and E. Fradkin, "Quantum criticality, lines of fixed points, and phase separation in doped two-dimensional quantum dimer models," *Physical Review B*, vol. 76, no. 13, p. 134514, 2007.

[103] K. Damle, "Melting of three-sublattice order in easy-axis antiferromagnets on triangular and kagome lattices," *Physical review letters*, vol. 115, no. 12, p. 127204, 2015.

[104] G.-W. Chern and O. Tchernyshyov, "Magnetic charge and ordering in kagome spin ice," *Phil. Trans. R. Soc. A*, vol. 370, no. 1981, pp. 5718–5737, 2012.

[105] J. V. José, L. P. Kadanoff, S. Kirkpatrick, and D. R. Nelson, "Renormalization, vortices, and symmetry-breaking perturbations in the two-dimensional planar model," *Physical Review B*, vol. 16, no. 3, p. 1217, 1977.

[106] O. F. Syljuåsen, "Directed loop updates for quantum lattice models," *Physical Review E*, vol. 67, no. 4, p. 046701, 2003.

[107] O. F. Syljuåsen and A. W. Sandvik, "Quantum monte carlo with directed loops," *Physical Review E*, vol. 66, no. 4, p. 046701, 2002.

[108] A. Bray, "Random walks in logarithmic and power-law potentials, nonuniversal persistence, and vortex dynamics in the two-dimensional xy model," *Physical Review E*, vol. 62, no. 1, p. 103, 2000.

[109] S. Redner, *A guide to first-passage processes*. Cambridge University Press, 2001.

[110] G. Barkema and M. Newman, "Monte carlo simulation of ice models," *Physical Review E*, vol. 57, no. 1, p. 1155, 1998.

[111] A. W. Sandvik, "Computational studies of quantum spin systems," in *AIP Conference Proceedings*, vol. 1297, pp. 135–338, American Institute of Physics, 2010.

[112] F. Alcaraz and R. Koberle, "Duality and the phases of z (n) spin systems," *Journal of Physics A: Mathematical and General*, vol. 13, no. 5, p. L153, 1980.

[113] B. Alder and T. Wainwright, "Phase transition in elastic disks," *Physical Review*, vol. 127, no. 2, p. 359, 1962.

[114] P. W. Kasteleyn, "Dimer statistics and phase transitions," *Journal of Mathematical Physics*, vol. 4, no. 2, pp. 287–293, 1963.

[115] M. E. Fisher, "On the dimer solution of planar ising models," *Journal of Mathematical Physics*, vol. 7, no. 10, pp. 1776–1781, 1966.

[116] D. S. Rokhsar and S. A. Kivelson, "Superconductivity and the quantum hard-core dimer gas," *Physical review letters*, vol. 61, no. 20, p. 2376, 1988.

[117] M. Hasenbusch, "The kosterlitz–thouless transition in thin films: a monte carlo study of three-dimensional lattice models," *Journal of Statistical Mechanics: Theory and Experiment*, vol. 2009, no. 02, p. P02005, 2009.